



universität  
wien

# DISSERTATION

Titel der Dissertation

Multiple Length-Scale Modeling of  
Through-Mask Electrochemical  
Micromachining of Complex PCBs

Verfasser

Mag. Peter Raffelstetter

Angestrebter akademischer Grad

Doktor der Naturwissenschaften

Wien, 2010

Studienkennzahl lt. Studienblatt:

A 091 419

Dissertationsgebiet lt. Studienblatt:

Chemie

Betreuer:

A.o. Univ.-Prof. Dr. Peter Herzig



# Abstract

The modeling of through-mask electrochemical micromachining of complex patterned workpieces, such as printed circuit boards (PCBs), faces the challenge of multiple length scales. While the characteristic dimensions of the features are typically tens of micrometers, the dimension of the entire working electrode may be centimeters or larger.

A hierarchic modeling strategy has been developed which allows to compute the shape evolution of any desired feature of a complex PCB design. The strategy consists of three separate and consecutive simulations on the macroscopic, the mesoscopic and the microscopic scale. These simulations are merged by considering the other scales than the one in question in a simplified way. The macroscopic modeling step considers all geometric factors of the reactor, but neglects the shapes and sizes of features by using the active area density approach. The mesoscopic step takes into account all geometric factors of the features, but considers only a mesoscopic section of the workpiece. On the microscopic scale, moving-boundary simulations of individual features are performed.

An auxiliary electrode has been introduced into the modeling strategy to investigate its potential in governing the uniformity of the shape evolution. The performance of the auxiliary electrode is governed by a complex interplay of different current density extrema caused by the patterning of the workpiece. This interplay could be cleared up by plotting the current density of the extrema versus the respective parameters. An optimized auxiliary electrode was found to be highly effective in preventing loss of electrical contact due to non-uniform shape evolution.

The direct modeling of complex patterned workpieces is in general infeasible, because it is highly costly in terms of allocated memory. The proposed modeling strategy replaces the direct simulation by three separate simulations, each feasible on customary personal computers and yields results which reflect the real complexity of the workpiece.



# Zusammenfassung

Die Simulation der elektrochemischen Mikrobearbeitung komplex fotolithografisch strukturierter Werkstücke umfasst Längenskalen unterschiedlicher Größenordnungen. Die charakteristischen Maße einzelner Strukturelemente betragen typischerweise einige Dutzend Mikrometer, wohingegen die gesamte Arbeitselektrode Zentimeter oder mehr messen kann.

Eine hierarchische Modellierungsstrategie wurde entwickelt, die die Berechnung des Ätzprofils jedes beliebigen Strukturelements eines komplexen Printed Circuit Boards (PCBs) ermöglicht. Die Strategie besteht aus drei separaten und konsekutiven Simulationen auf der makroskopischen, mesoskopischen und mikroskopischen Skala. Diese Simulationen werden miteinander verknüpft, indem bei der Modellierung auf einer Skala die anderen Skalen auf eine vereinfachte Weise Berücksichtigung finden. Der makroskopische Modellierungsschritt berücksichtigt alle geometrischen Einflussgrößen des Reaktors, vernachlässigt aber jene der Strukturelemente durch Anwendung des Active Area Density Konzepts. In den mesoskopischen Schritt fließen alle geometrischen Details der Strukturelemente ein, jedoch umfasst er nur einen mesoskopischen Teil des Werkstücks. Auf der mikroskopischen Skala werden Moving-Boundary Simulationen einzelner Strukturelemente durchgeführt.

Eine Hilfselektrode wurde in die Modellierungsstrategie einbezogen, um den Einfluss derselben auf die Homogenität der Ätzratenverteilung zu untersuchen. Das Leistungsvermögen der Hilfselektrode wird von einem komplexen Zwischenspiel verschiedener Stromdichteextremwerte bestimmt, welches durch die Strukturierung der Arbeitselektrode bedingt ist. Das Zwischenspiel konnte mittels der Abhängigkeiten der Extremwerte von den untersuchten Parametern aufgeklärt werden. Eine optimierte Hilfselektrode zeigte sich äußerst effizient in der Homogenisierung der Ätzratenverteilung.

Die direkte Simulation komplex strukturierter Werkstücke ist aufgrund des benötigten Arbeitsspeichers im Allgemeinen nicht möglich. Die entwickelte Strategie ersetzt die direkte Simulation durch drei separate Modellierungsschritte, die auf gebräuchlichen Computern durchführbar sind, und liefert Ergebnisse, die die tatsächliche Komplexität des Werkstücks widerspiegeln.



# Acknowledgments

This thesis has been conducted at the Center of Electrochemical Surface Technology (CEST), a center of competence in the COMET funding program for non-university research, and its predecessor the Center of Competence in Applied Electrochemistry (ECHEM), respectively. It has been supervised at the Department of Physical Chemistry of the University of Vienna by A.o. Univ.-Prof. Dr. Peter Herzig.

I would like to thank the Austrian Research Promotion Agency (FFG) and the government of Lower Austria for the financial support given in the framework of the COMET program and the University of Vienna for the framework of the supervision of this thesis.

I am grateful to A.o. Univ.-Prof. Dr. Peter Herzig for supervising this thesis. I would especially like to thank Dr. Bernhard Mollay for the careful choice of the objective, the technical mentoring and for receiving the best possible support and promotion. He has shown dedication and tireless efforts not only in the work which formed this thesis. My thanks also go to my colleague Mag. Gunther Schöllhammer who has provided assistance in numerous ways. It is a pleasure to thank the colleagues at CEST for offering a pleasant and constructive working atmosphere.

I would like to express my gratitude to my parents and my sister and to all of my friends for their absolute confidence in me and for offering encouragement and support. This thesis would not have been possible without them.





# Contents

<b>1</b>	<b>Introduction</b>	<b>1</b>
1.1	Objective . . . . .	2
<b>2</b>	<b>Through-Mask Electrochemical Micromachining</b>	<b>5</b>
2.1	Competing Technologies . . . . .	7
2.2	Technical Applications of Through-Mask EMM . . . . .	8
<b>3</b>	<b>Fundamentals on Current Density Distributions</b>	<b>13</b>
3.1	Primary Current Density Distributions . . . . .	14
3.2	Secondary Current Density Distributions . . . . .	17
3.2.1	Active Area Density Concept . . . . .	18
3.3	Tertiary Current Density Distributions . . . . .	20
<b>4</b>	<b>Survey of Literature</b>	<b>21</b>
4.1	Modeling of Current Density Distributions on Complex Patterned Substrates . . . . .	21
4.2	Modeling of Shape Evolution in Through-Mask EMM . .	24
4.3	Modeling of Auxiliary Electrodes . . . . .	24
<b>5</b>	<b>Modeling Strategy</b>	<b>27</b>
5.1	Strategy . . . . .	27
5.1.1	Macroscopic Modeling Step . . . . .	28
5.1.2	Mesosopic Modeling Step . . . . .	29
5.1.3	Microscopic Modeling Step . . . . .	30
5.2	Mathematical Model . . . . .	31
5.3	Software Tools . . . . .	32
<b>6</b>	<b>Modeling of a Typical PCB</b>	<b>33</b>
6.1	Simulations without Consideration of Auxiliary Means .	34
6.1.1	Macroscopic Modeling . . . . .	34
6.1.2	Mesosopic Modeling . . . . .	37

6.1.3	Microscopic Modeling . . . . .	49
6.2	Simulations Considering an Auxiliary Electrode . . . . .	56
6.2.1	Macroscopic Modeling . . . . .	56
6.2.2	Mesosopic Modeling . . . . .	63
6.2.3	Microscopic Modeling . . . . .	65
<b>7</b>	<b>Direct Simulation</b>	<b>67</b>
7.1	Accuracy of the Macroscopic Modeling Step . . . . .	69
7.2	Accuracy of the Mesoscopic Modeling Step . . . . .	74
7.2.1	Choosing an Appropriate Frame Size . . . . .	93
<b>8</b>	<b>Future Work / Outlook</b>	<b>95</b>
<b>9</b>	<b>Conclusions</b>	<b>97</b>
<b>A</b>	<b>Photoresist Thickness</b>	<b>101</b>
<b>B</b>	<b>Numerical Issues</b>	<b>105</b>
	<b>Bibliography</b>	<b>109</b>
	<b>Publications on this Thesis</b>	<b>113</b>
	<b>List of Symbols</b>	<b>115</b>
	<b>List of Figures</b>	<b>117</b>
	<b>List of Tables</b>	<b>121</b>
	<b>Curriculum Vitae</b>	<b>123</b>

# Chapter 1

## Introduction

It is well-understood in electrochemistry that current density varies in general over electrode surfaces [1, 2]. Nearly every technical application of electrochemical processes is in pursuit of a uniform current density distribution. In fact, the success of electrochemical fabrication techniques has largely been depending on securing a uniform deposition or etching rate distribution, respectively. Evaluation and governing of current density distributions is thus of great importance for industrialists and scientists engaged in this field.

The prediction of current density distributions by modeling has proven to be an extremely valuable tool since it can reduce the need for trial-and-error experiments. Prentice and Tobias [3] have given a comprehensive survey of current distribution simulations, discussing both analytical and numerical approaches. They also discussed fundamentals on the topic of current density distributions. Due to the ever-increasing capabilities of modern computers, numerical modeling can nowadays tackle highly complex and sophisticated problems.

One of such problems are current density distributions over complex photolithographically structured electrodes, e.g., printed circuit boards (PCBs). These substrates are assembled of an insulating support topped with a metal layer, onto which a photolithographic mask, or photoresist, is applied (Fig. 1.1). Etching of such electrodes is referred to as through-mask electrochemical micromachining [4, 5, 6] and deposition on them is referred to as through-mask electrodeposition [7, 8].

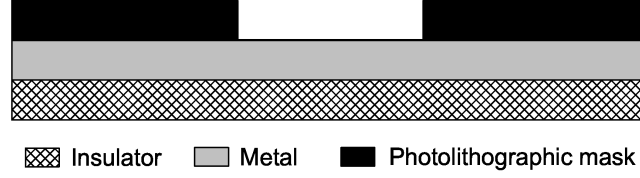


Figure 1.1: Typical photolithographically structured substrate.

PCBs, or printed wiring boards (PWBs), are the basic building block of electronic packaging [9]. In the course of the scale integration triggered by electronics industry, they have become an essential part of overall electronic devices. PCBs are designed to interconnect and assemble electronic components, e.g., integrated circuits (ICs), to form functional and operating systems. Both of the fabrication processes named in the former paragraph are of importance in the production of PCBs because they offer some unique advantages over competing technologies.

Modeling of electrochemical processes on complex photolithographically structured substrates faces the challenge of multiple length scales: The characteristic dimensions of individual features (conducting lines, pads, ...) are typically tens of micrometers, whereas the dimension of the entire workpiece may be centimeters or larger. In order to ensure a sufficient discretization all over the working electrode, an extremely fine mesh needs to be applied. Because the number of nodal points or elements, respectively, correlates with the allocated memory during the computation, such simulations are in general infeasible on customary personal computers.

## 1.1 Objective

The objective of this dissertation is to elaborate a modeling strategy which makes the simulation of current density distributions on PCBs or other complex photolithographically patterned substrates feasible. It will be developed for and applied to through-mask electrochemical micromachining processes. The strategy should be able to predict not only the initial current density distribution, but also the shape change of the electrode. As outlined above, the main challenge of this aim is to reduce

the allocated memory significantly.

Such a modeling strategy would be a powerful tool for the optimization of the electrochemical micromachining process and hence, of considerable interest in industry-related research and development. It could not only yield quantitative predictions but also allow for a deeper understanding of how the different process parameters act and would consequently reduce the need for trial-and-error experiments.



## Chapter 2

# Through-Mask Electrochemical Micromachining

Through-mask electrochemical micromachining falls in the category electrochemical machining, in the following abbreviated as ECM [10]. ECM is a fabrication process where the workpiece is made the anode in an electrolytic cell. The cathode is the machining tool and has the shape of the negative mirror image of the desired workpiece. The two electrodes are sited closely together; their distance from each other is called the machining gap. Upon passage of current through the electrolytic cell, the anode dissolves locally so that a workpiece with the desired shape is generated. In order to remove the products of the electrochemical reactions and to dissipate the generated heat, the electrolyte flows at high velocities through the inter-electrode gap.

The term electrochemical micromachining (EMM) [5, 6, 10] refers to ECM processes in dimensions ranging from micrometers to millimeters. It involves maskless or through-mask material removal, the latter being termed through-mask electrochemical micromachining. The classical maskless EMM is the scaling-down of ECM. Other maskless EMM techniques include jet-EMM, where the localization of the material removal is caused by the impingement of a fine electrolytic jet. There is no need to give the cathode a specific shape or to bring it close to the workpiece, although a small distance between the nozzle and the anode is required.

In through-mask EMM, a photolithographic mask is applied onto the workpiece and dissolution occurs only from areas not protected by the mask. I.e., the localization of the material removal is secured by the photolithographic mask. There are no specific requirements concerning the shape or position of the counter electrode.

Photolithography is a process used in microfabrication to selectively cover certain parts of a substrate with a so-called photolithographic mask, or photoresist [9]. Its basic steps involve the application of a light-sensitive polymeric layer onto the workpiece, exposing this layer to light with a desired pattern, and developing the exposed photoresist. In positive photoresists, the parts of the polymeric layer exposed to the light become soluble to the developer. In negative photoresists, the exposed area becomes insoluble to the developer. After the microfabrication step, which may be etching or deposition, the photoresist is removed chemically from the workpiece by a resist stripper. The continuing improvements in photolithography have made it possible for through-mask EMM to play an increasingly important role in microfabrication [5, 6].

The etching rate distribution on the workpiece is desired to be uniform in through-mask EMM, because a non-uniform etching of different openings of the mask will in general make the governing of the workpiece's shape difficult or even impossible. It may also cause loss of electrical contact (see below). This is contrary to ECM and maskless EMM, where the localization of the metal removal actually stems from the non-uniformity of the etching rate distribution.

The substrates in through-mask EMM typically consist of an insulating support layer topped with a metal layer, onto which a photolithographic mask is applied (Fig. 1.1). A process using such a substrate is referred to as one-sided through-mask EMM. In two-sided through-mask EMM, the metal layer is sandwiched between two congruent layers of photolithographic mask. The etching process thus occurs on both sides of the metal layer. In the framework of this thesis, the focus fell on one-sided through-mask EMM.

The assembly of the substrates in through-mask EMM causes an inherent drawback. Because the underlying support is insulating, the metal layer itself is the only electrical contact to the power source. The metal at the openings of the photolithographic mask is usually completely etched off. If the etching is non-uniform and higher etching rates occur at the



brink of the workpiece, the electrical contact will be lost and the process will stop prematurely before the etching is finished in the middle of the workpiece. This problem does not apply if there is a continuous area or lane of photoresist running from the brink to the middle, e.g., the fabrication of vias in a metal layer. I.e., loss of electrical contact depends highly on the design of the workpiece. PCB designs usually have an open area along the edges and hence, a non-uniform distribution of the etching rate would cause loss of electrical contact.

## 2.1 Competing Technologies

ECM and maskless EMM are alternatives to conventional metal-cutting machining technologies. They offer various advantages such as no tool wear, no physical or thermal strain, absence of burr, high machining rate, bright surface finishing, processing of three-dimensional shapes in one single step and independence of the hardness of the material. On the other hand, ECM and EMM suffer from the inability to machine non-conductive materials, dependence on the electrochemical properties of the electrode-electrolyte system, sophisticated machining design, corrosion, handling of gas evolution and a higher power consumption. They are cost-effective for high production numbers, but ineffective for low production numbers. This is because each material requires research on the electrode-electrolyte system and each workpiece requires the design of a machining tool.

In integrated circuits fabrication, dry vacuum etching technologies are preferred to EMM. The former include ion etching, plasma etching and reactive ion etching [11]. Plasma etching is carried out at relatively high pressure and is based on chemical reactions of gaseous species with the substrate. As a consequence, plasma etching is selective but isotropic. Ion etching is carried out at low pressure and is a physical process. Ions are accelerated to the substrate and erode the surface by momentum transfer. This technique offers anisotropic etching but suffers from lack of selectivity, i.e., the photolithographic mask is also eroded by the ion beam. Reactive ion etching is a compromise between the two other dry etching techniques; it involves both chemical and physical effects. Dry etching technologies offer high reproducibility, high resolution and precision, control of end point, no capillary and galvanic effects and ease

of automation. Among their disadvantages are etching defects due to momentum transfer, erosion of the mask, scarce selectivity for certain material combinations, re-deposition on the substrate and the need for expensive and specialized equipment.

Chemical micromachining (CMM) is another competing technology in microelectronics [12, 13, 14, 15]. It involves chemical reactions in an electrolyte by which the workpiece substrate is oxidized to soluble reaction products. CMM depends on the aggressive nature of the electrolyte, which is in general toxic and corrosive. It has found widespread use because of its following advantages: cost-effectiveness, high throughput, high reliability, ease of use, high reproducibility and high selectivity due to the chemical nature of the etching process. The disadvantages include limited resolution, isotropy, safety issues and environmental concerns.

The advantages of through-mask EMM over alternative technologies include good control and flexibility, high machining rate, high selectivity, low costs and environmental acceptability. One of the main problems encountered in EMM is the non-uniformity of the machining rate, giving rise to loss of electrical contact. This can in general be improved by proper adjustment of electrochemical and geometric parameters, which is topic of the given thesis. Other drawbacks include isotropy and limited resolution. In comparison with CMM, through-mask EMM offers higher machining rates, better control, better surface texture, better influence on isotropy and a wider range of materials which can be machined, compensating the non-uniformity of the machining rate.

## 2.2 Technical Applications of Through-Mask EMM

This section is a literature survey on technical processes for which through-mask EMM has been reported to be of interest. The technical applications are arranged by the machined material. Where applicable, the pros and cons are discussed in terms of the special demands of each technical process.

*Titanium* – Biomedical implantable devices, e.g., dental and orthopedic implants and biomedical microsystems such as load bearing or

drug containing devices are often made of titanium and titanium alloys. These materials offer biocompatibility, high fracture toughness and excellent corrosion resistance. Through-mask EMM has received attention in the fabrication of biomedical implantable devices from titanium [16, 17, 18]. The well-defined surface topographies obtained with EMM are a crucial advantage in this application. This is because the biomedical performance of titanium depends highly on the surface structure on the micrometer and nanometer scale. The alternative chemical etching process suffers from severe safety and environmental problems because it requires HF-based chemistry. Chauvy et al. [19] applied a special technique of through-mask EMM to titanium. They generated a defined surface oxide layer, which was subsequently structured by removing the oxide with excimer laser irradiation. The structured oxide functioned as lithographic mask in the machining process.

*Steel* – Steel has a particularly broad field of application, and so has through-mask EMM of steel. Datta [20] discussed the production of nozzle plates for inkjet printer heads by through-mask EMM. Inkjet printing is based on ejecting the ink through nozzles by the pressure caused from the heating-up and vaporization of the ink constituents. The demands on the nozzles are a highly reproducible shape and dimension as well as the electrical and mechanical properties of the material. Through-mask EMM meets these demands and offers a competitively-priced manufacturing process.

In hard disk drives, the information is stored on magnetic hard-disk platters. To read and write data, a slider with a magnetic head is moved along the platter. The slider is mechanically attached to a suspension, which is moved by an actuator arm. Through-mask EMM has received attention in the manufacturing of such slider suspensions [21]. The slider suspension in this patent consists of an insulating layer which is sandwiched between a steel and a copper layer. Both metal layers are etched through a photolithographic mask. The specific advantage of through-mask EMM in this application is the potential to machine both metal layers with the same electrolyte in one fabrication step. CMM has been applied without much success, because it is highly selective concerning the material: It requires two separate fabrication steps for steel and copper.

Proton exchange membrane fuel cells (PEMFCs) consist of a conductive polymer serving as electrolyte sandwiched between two bipolar plates serving as electrodes. The bipolar plates have a defined channel structure, which allows the transport of the fuel to the electrodes and the evacuation of the reaction products. Through-mask EMM has been reported to be attractive for the production of such bipolar plates [22]. They are often made of stainless steel, although other corrosion-resistant alloys may also be of interest.

Kwon et al. [23] conducted a study on the fabrication of shadow masks with through-mask EMM. These masks are perforated steel plates with many small holes and are used for cathode ray tube televisions and computer displays. The holes are placed in a particular pattern ensuring that the radiation from the cathode guns reaches only the appropriately-colored spots on each pixel of the display. Shadow masks are made of invar, an iron-nickel alloy with 36 weight percent nickel, which meets the requirement of a small thermal expansion coefficient. In this application, through-mask EMM is an excellent alternative to chemical etching because the latter involves  $\text{FeCl}_3$  solutions causing disposal problems. Furthermore, this fabrication process requires well-defined and reproducible shapes of the holes, which is met by through-mask EMM.

*Copper* – Because of its high conductivity and electromigration resistance, copper is highly attractive for applications in microelectronics. PCBs, for instance, are usually made of this metal. Datta [24] discussed the fabrication of PCBs with through-mask EMM. A crucial advantages in this application is the ability to provide straight and smooth walls for copper lines of varying dimensions. Major drawbacks are the problem of island formation in large openings of the photoresist and the loss of electrical contact.

Another application of electrochemically machining copper through masks is the fabrication of cone connectors [25]. Cone connectors are detachable electrical interconnections in electronic packaging applications and may be used to interconnect for example integrated circuits with PCBs and cards with each other or with cables. They are conical protrusion of specific shape and location, which may either contact with other cone connectors or with plane surfaces. For fabricating such shapes, the mask consists of photoresist dots placed at positions where the connec-

tors are meant to evolve. Through-mask EMM is a favorable technique for the fabrication of cone connectors because it yields well-defined, reproducible shapes and can be applied to a wide range of materials. Cone connectors may also be made of other metals including, but not limited to, gold, tin, lead, aluminum, and steel.

*Molybdenum* – Two-sided through-mask EMM has received attention in the production of metal masks for screen printing [26]. Screen printing is a process where a metal paste is forced by a squeegee through the openings of a mask onto a substrate. In other words, the parts of the substrate where no paste should be applied are shielded, or “screened”, by the mask, which is where the term “screen printing” comes from. The design of the mask defines the pattern of the metallization. After the printing of the metal paste, the substrate is heated in order to obtain a solid metal pattern having good electrical properties. Molybdenum masks are used for the most demanding screen printing applications, because they provide better edge definition and paste release properties than alternative materials such as steel. Through-mask EMM offers etching rates of up to 100 times larger than the etching rates in the earlier established CMM process along with better surface finish and better aspect ratios. Furthermore, CMM of molybdenum is performed with ferricyanide solution, posing safety and environmental problems.

*Platinum* – Frankenthal and Eaton [27] employed through-mask EMM in the manufacturing of silicon integrated circuits. They studied a metallization procedure which involves the sequential application of a titanium, platinum and gold layer. The platinum and gold layers are patterned according to their functionality. This study demonstrates the potential of electrochemical etching through masks in the patterning of the platinum layer. It uses an HCl-based electrolyte, whereas chemical etching uses aqua regia. Other attractive features regarding this application are better control of the etching endpoint, better reproducibility and higher etching rates.

Other materials for which through-mask EMM is an attractive fabrication technology include conductive ceramics, doped silicon and germanium semiconductors and various metals such as tantalum, tungsten, nickel, titanium, rhodium, aluminum and palladium [5, 6, 24].



## Chapter 3

# Fundamentals on Current Density Distributions [1, 2]

Generally speaking, the local current density varies over electrode surfaces. It may only be uniform for special geometries and conditions, respectively. The term “current density distribution” refers to the function  $j = f(x, y, z)$ , where  $j$  is the local current density flowing through the point on the solid-liquid interface having the coordinates  $x$ ,  $y$  and  $z$ . Current density distributions are subdivided into primary, secondary and tertiary distributions [28].

The basis for a discussion of current density distributions are the laws governing the transport of solute species in electrochemical systems. The starting point in this derivation is the flux density  $\mathbf{N}_k$  of the species  $k$  through an ideal dilute electrolyte given by

$$\mathbf{N}_k = -D_k \nabla c_k + c_k \mathbf{v} - \frac{z_k F}{RT} c_k D_k \nabla U, \quad (3.1)$$

where  $D_k$  is the diffusion coefficient,  $c_k$  the concentration and  $z_k$  the charge of the species  $k$ .  $\mathbf{v}$  denotes the velocity of the electrolyte,  $F$  Faraday’s constant,  $R$  the gas constant,  $T$  the temperature and  $U$  the potential of the electrolyte. The first two terms in Eq. 3.1 represent the contribution of diffusion and convection to the flux density and the third term the contribution of migration.

The law of mass conservation states that the change of the concentration of species  $k$  in an infinitesimal volume with time is given by the net

flux density of species  $k$  entering or leaving the volume and the amount of species  $k$  generated or consumed by chemical reactions:

$$\frac{dc_k}{dt} = -\nabla \mathbf{N}_k + v_k, \quad (3.2)$$

where  $t$  represents the time and  $v_k$  the moles of the species  $k$  generated or consumed per unit volume.

Inserting the flux density given in Eq. 3.1 into Eq. 3.2 and assuming an incompressible fluid ( $\nabla \mathbf{v} = 0$ ) yields

$$\frac{dc_k}{dt} = D_k \nabla^2 c_k - \mathbf{v} \nabla c_k + \frac{z_k F}{RT} D_k \nabla (c_k \nabla U) + v_k. \quad (3.3)$$

Eqs. 3.1 and 3.3 are the most important fundamental equations concerning the transport of solute species in electrochemical systems.

### 3.1 Primary Current Density Distributions

The primary current density distribution establishes itself when the influence of charge-transfer and concentration overpotential can be neglected. The latter assumption implies that there are no concentration gradients in the electrolyte

$$\nabla c_k = 0. \quad (3.4)$$

In that case,  $\frac{dc_k}{dt}$  as well as the first and second term in Eq. 3.3 equal zero. Furthermore, the third term can be simplified because  $\nabla (c_k \nabla U) = \nabla c_k \nabla U + c_k \nabla^2 U = c_k \nabla^2 U$ . The term  $v_k$  can be dropped if Eq. 3.1 is multiplied by the ionic charge and the sum for all ionic species is taken (for details see [1]). What remains of Eq. 3.3 is

$$\nabla^2 U = 0. \quad (3.5)$$

This equation is called Laplace's equation and it governs the potential distribution in the electrolyte. Its numerical solution over the electrolyte is the basis for the simulation of primary current density distributions. In the absence of concentration gradients, the current density  $\mathbf{j}$  at any



point in the electrolyte is related to the potential by Ohm's law:

$$\mathbf{j} = -\kappa \nabla U, \quad (3.6)$$

where  $\kappa$  is the conductivity of the electrolyte.

In deriving the governing equations for the primary current density distribution (Eqs. 3.5 and 3.6), the terms representing the contribution of diffusion and convection in Eq. 3.1 have dropped out. What remains is the contribution of migration, which is in fact the reason for applying Ohm's law in Eq. 3.6. This mathematical model is called potential model or potential theory.

For the computation of primary current density distributions, polarization resistance, or charge-transfer resistance, is neglected. The boundary conditions on Eq. 3.5 are as follows.

$$U = \text{const.} \quad \text{at electrode surfaces,} \quad (3.7)$$

$$j = -\kappa \frac{\partial U}{\partial n} = 0 \quad \text{at insulating surfaces,} \quad (3.8)$$

where  $j$  is the component of  $\mathbf{j}$  at the surface perpendicular to it, i.e., the current flowing through the solid-liquid interface.  $n$  represents the spatial coordinate perpendicular to the boundary.

Non-uniformity in current density distributions caused by migration stems from variations in ohmic pathways. Ohmic pathways are the regions of the electrolyte which transport solute species to and from specific regions of the electrodes. This will be outlined in the following for a simple example. Fig. 3.1 shows schematically the current field of an electrochemical cell with parallel electrodes embedded in insulating walls. The current tubes A and B comprise the pathways for the flux density from the electrode segment  $Q_C$  to  $Q_A$  and from  $R_C$  to  $R_A$ , respectively. In the potential model, the flux density is solely determined by Ohm's law. The ohmic pathway B is larger than A and thus, the conductance of pathway B is larger than of pathway A (the conductivity of the electrolyte is evidently constant). Pathway B allows for a faster transport of ionic species, i.e., for a larger ion flux, to the edge of the electrode, which results in a larger current density there. That is why in many electrochemical systems current density is largest at corners and edges of electrodes.

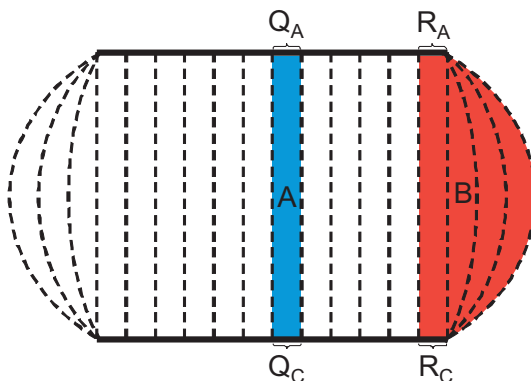


Figure 3.1: Schematic illustration of the current lines in a parallel plate reactor. The blue current tube is named A and the red tube B.

Primary current density distributions depend only on the geometric factors of the electrochemical cell. Neglecting the polarization resistance means that the electrochemical parameters of the electrode do not play a role. The conductivity of the electrolyte does not influence the distribution either. It does change the conductance of ohmic pathways (and thus the average current density) but not their ratio (which determines the distribution). Primary current density distributions can only become uniform for special geometric situations, e.g., for plain parallel electrodes filling completely the cross-section of the cell or for concentric cylinders and spheres. In general, they are the most non-uniform distributions.

Primary current density distributions are usually not associated with realistic distributions. They are used to obtain a first tentative picture of the distribution in electrochemical cells if there is no information about the electrochemical parameters and should be seen as a worst-case prediction concerning the uniformity. Primary distributions are most likely to show good agreement with experiment if the charge-transfer resistance is small and the average current density is well below the limiting current density.

## 3.2 Secondary Current Density Distributions

Secondary current density distributions take into account charge-transfer resistance but neglect concentration overpotential. Because the assumption of neglecting concentration gradients also applies for secondary current density distributions, the potential model may be used for their simulation. The electrochemical factors of the polarization resistance enter the model via the boundary conditions on Eq. 3.5, which are as follows.

$$j = f(\eta) \quad \text{at electrode surfaces,} \quad (3.9)$$

$$j = 0 \quad \text{at insulating surfaces.} \quad (3.10)$$

$\eta$  represents the overpotential, which is defined as the potential applied to an electrode minus its equilibrium potential ( $\eta = V - V_0$ ).  $f(\eta)$  is the polarization curve or polarization function of the given electrode.

In general, secondary current density distributions tend to be more uniform than primary ones. As in primary distributions, the transport of solute species in secondary distributions is based solely on migration and Ohm's law holds. Hence, the picture of ohmic pathways outlined before also holds here. The charge-transfer resistance adds in series with the resistance of the ohmic pathways. If a voltage is applied, some of the potential drops at the polarization resistances and hence, less potential drop is available for the ohmic pathways. The influence of the ohmic pathways is thus less pronounced in the current density distribution. Often, the charge-transfer resistance may be assumed to be constant or at least varies in a relatively small range, which makes secondary distributions more uniform. The larger the charge-transfer resistance, the smaller is the influence of the ohmic pathways and the more uniform is the distribution. If the charge-transfer resistance is constant and much larger than the resistance of the ohmic pathways, so that the latter can be neglected, the current density distribution is uniform.

Wagner [29] discussed a criterion for the uniformity of secondary current density distributions, which was subsequently named Wagner's number  $W_a$  [28].

$$W_a = \frac{\frac{\partial \eta}{\partial j}}{\rho l}, \quad (3.11)$$

where  $\frac{\partial \eta}{\partial j}$  is the charge-transfer resistance,  $\rho$  is the resistivity of the electrolyte and  $l$  is the characteristic length. When  $\frac{\partial \eta}{\partial j} \gg \rho$ ,  $W_a \rightarrow \infty$  which means the distribution is uniform. When  $\frac{\partial \eta}{\partial j} \ll \rho$ ,  $W_a \rightarrow 0$  which means the polarization resistance is negligible. The distribution is then primary and thus pronounced non-uniform. The characteristic length is an important factor for structured electrodes which involve characteristic lengths spanning several orders of magnitudes, or in the scaling-up and scaling-down of electrochemical cells. Current density distributions tend to be more uniform for smaller characteristic lengths.

Secondary current density distributions are an applicable mathematical model for situations where the average current density is well below the limiting current density. Under these conditions, the depletion of the consumed solute species at the electrode surfaces is negligible and Eq. 3.4 holds. If concentration overpotential cannot be neglected, the secondary model may still be valuable for a discussion of migrational effects, which may be the main cause for non-uniformity in tertiary current density distributions.

### 3.2.1 Active Area Density Concept

The active area density concept was introduced by Mehadizadeh et al. [30]. It is a modification of the potential model and computes secondary current density distributions on photolithographically patterned electrodes. The difference lies in the boundary conditions.

The active area density, denoted by the symbol  $a$ , is defined as the quotient of the active area  $A^{\text{ACT}}$  and the superficial area  $A^{\text{SUP}}$

$$a := \frac{A^{\text{ACT}}}{A^{\text{SUP}}}. \quad (3.12)$$

$A^{\text{ACT}}$  is simply the electrode area.  $A^{\text{SUP}}$  equals the sum of the electrode surfaces and the surfaces of the photolithographic mask parallel to the electrode. Using the active area density, the superficial current density  $j^{\text{SUP}}$  is defined as

$$j^{\text{SUP}} := a f(\eta). \quad (3.13)$$

This equation holds as boundary condition on Eq. 3.5 for the entire work-piece. The boundary conditions for the other reactor surfaces (insulating

walls and electrodes) are identical to those discussed before (Eqs. 3.9 and 3.10).

$j^{\text{SUP}}$  is simply the current density per unit superficial area and is thus not the appropriate output function to visualize the etching rate. The quantity  $j^{\text{ACT}}$

$$j^{\text{ACT}} := \frac{j_n^{\text{SUP}}}{a} \quad (3.14)$$

is the current density per unit active area and hence, the proper quantity to evaluate the etching rate by means of Faraday's law. It will be used for plots of current density distributions computed by using the active area density approach.

When modeling a photolithographically patterned electrode with the classical potential theory for secondary current density distributions, boundary condition Eq. 3.9 is applied for electrode surfaces and Eq. 3.10 for photoresist surfaces. This implies that the geometric factors of the photoresist pattern needs to be fed into the simulation. This is contrary to the active area density approach, where the boundary condition Eq. 3.13 is valid for the *entire* workpiece. This includes the areas covered by the photolithographic mask. I.e., the geometric factors of the photoresist pattern do not enter the simulation. Only the active area density varies over the electrode surface. Thus, the discretization does not need to be adjusted to the small characteristic length scales occurring in the photoresist pattern but to the length scale where the active area density varies. The latter length scale is much larger, which makes the discretization significantly less costly.

It is inherent in the active area density approach that the yielded current density distributions are continuous. The distribution over the real features of the photoresist is not yielded. One may regard only the current density where electrode surfaces are and ignore the rest, but the distribution can evidently only reflect variations in active area density and not the shapes and sizes of the features.

Variations in active area density can only be predominant in current density distributions if the resistance of the respective current tubes is similar and significantly larger than the charge-transfer resistance. In this case, one yields a current density distribution that mirrors the active area density distribution. For a piece-wise constant active area density distributions, this would mean a piece-wise constant current density dis-

tribution. These conditions apply only in special cases for the entire workpiece, e.g., for plain parallel electrodes filling completely the cross-section of the cell or for concentric cylinders and spheres. In such cases, the current tubes all over the workpieces are identical. They often may apply for parts of the workpiece, e.g., for the central region in Fig. 3.1 because the current tubes are practically identical there. Such a case will occur in Secs. 6.1.1 and 6.2.1.

### 3.3 Tertiary Current Density Distributions

Tertiary current density distributions account for charge-transfer overpotential and concentration overpotential. The latter implies that not only migration but also convection and diffusion are considered concerning the transport in the electrolyte. Hence, the simplification of neglecting concentration gradients in primary and secondary distributions is not applicable here and Eq. 3.5 has to be replaced by Eq. 3.3. The numerical integration of this equation is far more challenging. It is beyond the scope of these explanations to give a deeper insight into this topic; reference is given to Ibl [1] and Newman [2].

The influence of concentration overpotential is far more complex than the influence of charge-transfer overpotential and hence, qualitative considerations of tertiary current density distributions are limited. One may distinguish between the case where the thickness of the diffusion layer is much smaller than the characteristic dimension of the electrode (e.g., height of a trench) and the case where it is much larger. In the former case, the electrode is equally accessible to diffusion everywhere and the diffusion layer thus follows the profile of the electrode. Concentration overpotential makes the current density distribution more uniform under these conditions. In the other case, recesses are less accessible to diffusion and the concentration overpotential is consequently larger there. This results in a less uniform current density distribution having maxima at easily accessible regions, analogous to the non-uniformity caused by migration.

# Chapter 4

## Survey of Literature

Due to the high complexity of the problem stated in Chap. 1, modeling of photolithographically patterned electrodes is confined to relatively simple mathematical models. Authors have predominantly been using the potential model, which has been explained in detail in Chap. 3. Many studies consider only a single feature in investigating the through-mask EMM process. In this case, it is feasible to model tertiary current density distributions, which are evidently more realistic. However, the consideration of a single feature cannot reflect the real complexity of the workpiece. It is inadequate if the influence of the patterning is in the focus, for example, in preventing loss of electrical contact.

### 4.1 Modeling of Current Density Distributions on Complex Patterned Substrates

Numerous studies on the modeling of electrochemical processes on photolithographically patterned substrates have been reported in literature. The fundamental idea of how to simplify the overall problem was discussed for the first time by Kessler and Alkire [31]: They broke the system into different spatial scales. These scales were the macroscale, characteristic of the size of the entire workpiece, the miniscale, characteristic of the size of an individual feature, and the microscale, characteristic of surface roughness. A detailed discussion of the microscale was not in the scope of this study. The authors clarified the factors governing current

density distributions on the macro- and miniscale independently by using dimensionless parameters. Thus, an illustration of the interplay of various effects controlling the overall behavior was given. As many of the following references, this study deals with through-mask electrodeposition. Nevertheless, the relevant conclusions also hold for through-mask EMM.

Dukovic published two articles [32, 33] discussing the concept of considering different spatial scales. He additionally defined and discussed the so-called pattern scale, which is characteristic of regions that differ in electrode surface per unit area.

In the present investigation, the idea of splitting the problem into different spatial scales is adopted. The scales used in the framework of this thesis are defined as follows. The macroscopic scale considers the entire workpiece and all details of the reactor, but neglects individual features. The mesoscopic scale takes into account several features but not the whole workpiece. The term microscopic scale applies if one accounts for a single feature only. This nomenclature of the spatial scales will be used from now on.

Most studies conducted on the modeling of photolithographically patterned substrates focus on one scale and totally neglect the others. As was addressed before, such a simulation is not applicable where the influence of the photoresist pattern is of importance. Hence, it is highly desirable to link simulations on different spatial scales by considering the other scales than the one in question in a simplified way. Only in doing so, one can obtain current density distributions which reflect the real complexity of the substrate and discuss the characteristics of the process related to the photoresist pattern. This idea has, however, far escaped attention in literature and only a limited number of studies have been published. It is beyond the scope of this survey to give reference to the numerous publications confined to a single spatial scale; some of them have been reviewed by Dukovic [32, 33].

Mehdizadeh et al. [30] introduced a valuable concept for the simulation of secondary current density distributions on scales that are large compared to the scale of an individual feature. They computed macroscopic current density distributions while accounting for the microscopic scale in a simplified way by the active area density (see Sec. 3.2.1). The workpiece is sectioned into regions containing clusters of conducting lines



arranged in a specific density, and each subunit is seen as a continuous electrode surface characterized by its active area density. Their modeling concept allows for the computation of macroscopic current density distributions which reflect microscopic influences without entering attributes specific to individual features.

In a follow-up study [34], a simple consideration of mass transport was added on the active area density concept, which is originally a secondary model. As would be assumed, the authors found good agreement of the secondary model with experimental results only far below the mass-transfer limit. The tertiary model could very well predict current density distributions if concentration overpotential plays a dominant role.

The secondary active area density model has been used in several studies, one of them being conducted by Pantleon et al. [35]. They extended the corresponding approach to three dimensions and used it to predict the layer thickness distribution of electrochemically deposited copper. A good agreement of simulation with experimental results was found and thus the applicability of the respective modeling concept confirmed.

West et al. [36] computed macroscopic and microscopic current density distributions on six unevenly spaced conducting lines. It was assumed that the macroscopic scale is not influenced by the microscopic current density distribution on the conducting lines, but only by their average current density. Thus, the macroscopic modeling accounted for microscopic influences in a simplified way. The microscopic modeling performed in this paper did not take into account any macroscopic effects.

DeBecker and West [37] broadened that concept to a hierarchic modeling strategy which yields current density distributions on all three scales. The workpiece they considered is assembled of several pattern clusters which are themselves assembled of several conducting lines. On each scale, distributions on the other scales are neglected and only mean current densities are taken into account. This modeling approach thus merges simulations on three different spatial scales. It is, however, limited to the simulation of electrodes coplanar to insulating surfaces and cannot account for a photolithographic mask.

## 4.2 Modeling of Shape Evolution in Through-Mask EMM

The literature discussed in Sec. 4.1 deals solely with initial current density distributions. They may be used to predict the etch profile if the metal removal does not change the surface geometry significantly, i.e., if the removed layer is very thin. Through-mask EMM usually aims at removing the entire metal layer at regions not covered by the photolithographic mask. Initial current density or etching rate distributions are thus an incomplete investigation of the problem. The electrode shape change during the machining process is a crucial point in the overall performance of the process.

To model electrode shape changes, or shape evolution, for transient problems so-called moving boundary simulations are performed. The problem is discretized in time, and for each time step the electrode shape is determined from the etching rate distribution and the shape of the previous time step [1, 2].

As was discussed in Chap. 1, moving-boundary simulations of complex patterned substrate are in general infeasible. The respective literature is confined to the feature scale; the merging of influences from different scales on electrode shape change has not been approached. Prentice and Tobias [3] dedicated a section of their review article to discuss the beginnings of moving boundary simulations. Shape evolution in through-mask EMM has been modeled with primary [38, 39, 40] and secondary current density distributions [41]. The influence of the respective geometric factors was in the focus of these studies.

## 4.3 Modeling of Auxiliary Electrodes

Auxiliary electrodes, or current thieves, are electrodes which are used to prevent non-uniform current density distributions [42, 43]. They are of the same polarity as the working electrode and positioned close to the maxima of current density which they are meant to suppress. Especially if the mean current density or potential, respectively, of an auxiliary electrode is optimized, it is a highly effective tool in securing a certain

uniformity in the etching or deposition rate distribution. Current thieves are of interest in through-mask EMM for preventing loss of electrical contact and will be considered in the course of this thesis. A selection of relevant literature is given in the following.

Dalby et al. [42] and McCormick et al. [43] have given a general introduction into the field of auxiliary electrodes, addressing advantages, challenges and applications. They stated that planning ahead by simulation is a crucial step in the successful application of auxiliary electrodes. Lots of modeling studies on this topic have been published, most of them being focussed on the optimization for a special workpiece and a special reactor design, respectively. The paper by Mehdizadeh et al. [44] aims for a fundamental understanding of how an auxiliary electrode works. They clarified the relevant process parameters and how they affect the performance of the device. The conclusions which gave the starting point for the investigations in this thesis will be outlined in the next paragraph.

The modeling was carried out for a two-dimensional axisymmetric reactor, containing a coplanar, concentric auxiliary electrode surrounding the working electrode. A gap of insulating material separates the electrodes, and the potential of the auxiliary electrode can be controlled independently. Upon varying the mean current density of the auxiliary electrode, they found that for each set of geometric parameters an optimum mean current density exists, for which the uniformity is best. A lower mean current density than the optimum one results in not fully suppressed current density maxima at the edge. In contrast, a higher mean current density results in an inverted distribution, i.e., the minimum in current density is situated at the edge and the maximum at the center (for an outline of why current density maxima occur in general at edges, see Chap. 3). It may be expected that the distribution on the working electrode will always get more uniform if the size of the gap between the two electrode is reduced. But it was found that if the optimum current density of the auxiliary electrode is used throughout, an optimum gap size exists. I.e., the distribution gets less uniform if the gap size is below that value. A large Wagner's number and a wide auxiliary electrode both favor a uniform current density distribution.

Auxiliary electrodes have also been used in modeling studies for the governing of current density distributions on photolithographically patterned substrates [45, 46, 47]. These references deal solely with distribu-

tions on the macroscopic scale. The authors used the active area density concept to account for microscopic influences. Optimizations of the auxiliary electrodes for the given electrochemical cells were performed, and the results can be seen as an application of the generalized conclusions drawn by Mehdizadeh et al. [44]. The influence of some additional parameters has been investigated, e.g., the distance and size of the counter electrode [46] and the vertical distance of a non-planar auxiliary electrode [47].

# Chapter 5

## Modeling Strategy

### 5.1 Strategy

In the following, the introduced modeling strategy will be explained in a general manner, and it will be applied to a typical PCB design in Chap. 6.

The strategy breaks the overall problem into three spatial scales: the macroscopic scale, characteristic of the size of the entire workpiece; the mesoscopic scale, characteristic of the size of several features; and the microscopic scale, characteristic of the size of an individual feature. It consists of three separate and consecutive modeling steps, one on each of these size scales. The three simulation steps are merged by handing on mean current densities when going from one to the other step: The total current of the mesoscopic and microscopic modeling is determined from the current density distributions computed in the macroscopic and mesoscopic step.

The strategy is based on the assumption, that the current density distribution on a certain region is influenced by the shape of features in its close proximity, but not by the shape of features far away. Regions which are far away from the region in question influence only the mean current density of the latter by their own mean current density. The current density distributions of regions far away do not influence each other (for constant mean current densities). I.e., only the shapes and sizes of features in the close proximity need to be taken into account;

regions far away can be assumed to be continuous electrode surfaces.

The modeling strategy circumvents the direct simulation of the workpiece, which would be highly costly in terms of discretization or allocated memory, respectively, and thus infeasible on customary personal computers. Each simulation step of the strategy requires significantly less nodal points in discretization and is easily feasible on customary personal computers. The strategy thus makes the simulation of complex photolithographically patterned workpieces feasible.

### 5.1.1 Macroscopic Modeling Step

The macroscopic modeling step considers the entire workpiece and all geometric factors of the reactor. Individual features are accounted for in a simplified way by using the active area density approach [30]. The shapes and sizes of features do not enter the simulation, they are reflected merely by the active area density. The latter is defined as the electrode area per unit area and enters the simulation via the boundary conditions (see Sec. 3.2.1).

For continuously patterned electrodes, a constant active area density may be applied. Complex patterned electrodes such as PCBs need to be characterized with an active area density distribution. This distribution replaces the workpiece in macroscopic simulations. There is in general no analytical active area density distribution and hence, the working electrode is sectioned into piecewise-continuous subunits with different active area densities. Each subunit is a plane and continuous electrode surface, characterized only by the boundary condition which includes the active area density.

Working electrodes modeled in the literature [30, 34, 35] consist of clusters of evenly arranged features. In that case, choosing the subunits is trivial because each cluster will evidently be a subunit. Finding an active area density distribution for a PCB is not straightforward. The working electrode needs to be cut into subunits by a suitable raster, which inevitably cuts through features. If the raster is too fine, very small active area densities will occur and the accuracy of the respective approach breaks down [30]. If the raster is too coarse, mesoscopic simulations become infeasible. Between these limitations one may choose

the raster more or less arbitrarily. Using a finer raster will increase the complexity of the macroscopic discretization and decrease the complexity of the mesoscopic discretization. Making the raster more coarse has the opposite effect.

Among the factors of the reactor are auxiliary electrodes if present. Their geometric parameters as well as their potential or mean current density, respectively, are taken into account in this step.

The macroscopic modeling step computes the initial current density distribution on the entire workpiece. It is inherent in the active area density approach that it yields a continuous distribution and not the distribution over the real features (see Sec. 3.2.1). The macroscopic distribution is used to evaluate the mean current density of any interesting mesoscopic region, which is used as input in the next step. The distribution itself is not of interest to the modeling strategy.

### 5.1.2 Mesoscopic Modeling Step

The mesoscopic step considers merely a chosen mesoscopic region of the workpiece but accounts for all geometric factors of the respective region. For reasons of convenience, this mesoscopic region is in general a raster element, but could in principle also be a larger region. Choosing a region smaller than a raster element is not reasonable, because the active area density distribution cannot adequately reflect the feature's influence on a region smaller than its spatial resolution.

As a start, the mesoscopic reactor is a square box containing the chosen raster element (or mesoscopic region) at one base and the counter electrode filling the opposite one. The height of the reactor either equals the real distance between working electrode and counter electrode, or is large enough not to influence the current density distribution. The reactor is thus a section of the macroscopic reactor. The mean current density of the mesoscopic reactor equals the mean current density flowing through the respective raster element evaluated from the macroscopic simulation.

If the mesoscopic simulation is performed with a reactor as just described, a false behavior of the current density distribution near the border of the reactor is to be expected. This is due to cutting off all

surroundings. As was explained before, the shape of the *nearest* features indeed influences the distribution. E.g., a feature adjacent to the raster element which is just completely cut off influences the distribution in its close proximity, which includes the border of the element.

This problem is solved by enlarging the region considered in the mesoscopic reactor. The current density distribution on the additionally considered area is cut off, and only the distribution on the originally chosen region, in general a raster element, is used as output. The square bordering the region taken into account in mesoscopic simulations will be named “frame” from now on. Choosing an appropriate frame and thus considering enough of the surroundings is a sophisticated question. It highly depends on the shape of the features on the raster element and of the features nearby and will be discussed in Secs. 6.1.2 and 7.2. It will be shown there that using an appropriate frame can correct the false behavior very efficiently. The total current of the mesoscopic reactor is adjusted so that the current flowing through the raster element or mesoscopic region remains unchanged by enlarging the reactor.

The mesoscopic modeling step yields the initial current density on any desired raster element or mesoscopic region. In contrast to the macroscopic step, it is the distribution over the real features, because the shapes and sizes of the features enter the simulation. It will be used in the next step to evaluate the total current of the microscopic reactors.

### 5.1.3 Microscopic Modeling Step

The microscopic modeling step investigates the shape evolution of individual features. This step is chosen to be two-dimensional and is thus restricted to the investigation of trenches. These are the only features for which a two-dimensional cut is representative. Microscopic reactors contain the cross-section of a chosen trench, accounting merely for the placement of the neighboring features by placing the side walls at positions equidistant from the trench in question and the adjacent trenches. The counter electrode is placed either at the real distance from the working electrode or at a distance large enough so that it does not influence the current density distribution on the trench. The mean current density of the reactor is evaluated by taking the mean current density along the respective cross-section from the mesoscopic simulation. The total



current is kept constant during shape evolution, i.e., the mean current density of the anode changes according to the electrode area change.

If the initial current density on the PCB is non-uniform and the edge receives significantly more current density than central regions, the EMM process will stop prematurely due to loss of electrical contact (see Chap. 2). It will stop at the point when the insulating support is exposed to the electrolyte along the edges, and thus no electrical contact to the power source is provided. From then, the simulated etch profiles are hypothetical.

As outlined above, each trench is neighbored by features which are not taken into account. As a consequence, one has to take care that the metal wall profile of the trench in question does not penetrate into regions where in reality the metal wall profile of the neighboring feature has evolved. It is assumed that the neighboring features evolve at the same etching rate as the trench in question. In that case, the metal wall profiles would meet exactly half-way between the two features and may not penetrate further. The simulation is stopped if the etch profile reaches this position. It is concluded that in such a case the copper underneath the photolithographic mask surrounding the trench in question is completely etched off.

The microscopic modeling step yields the time-dependent etch profiles, or shape evolution, of any chosen trench on the PCB. The geometric factors of the surroundings are accounted for only by the position of the reactor's border and thus in less detail than in the mesoscopic step.

A flow-chart of the modeling strategy is depicted in Fig. 5.1.

## 5.2 Mathematical Model

All simulations are based on the potential theory for secondary current density distributions, which is explained in detail in Sec. 3.2. The macroscopic step is three-dimensional and uses the active area density approach to compute initial current density distributions. The active area density approach fulfills the requirements addressed in Sec. 5.1.1 in considering the photoresist pattern of the workpiece in a simplified way. The mesoscopic and the microscopic modeling call for a consideration of all

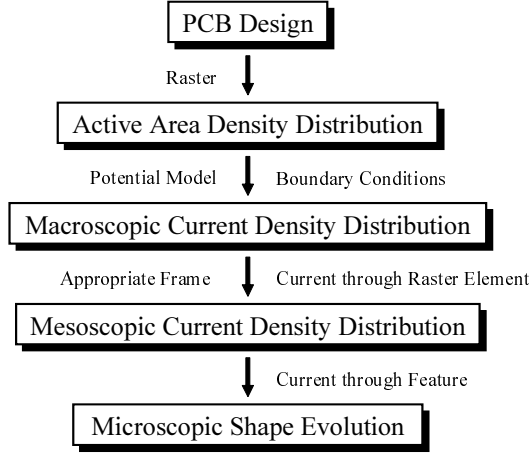


Figure 5.1: Flowchart of the proposed modeling strategy.

geometric factors and thus, for an application of the classical potential model. This is feasible for these two modeling steps because only sections of the workpiece are taken into account. The mesoscopic step is carried out in three dimensions and yields initial distributions, whereas the microscopic step is two-dimensional and involves moving boundaries.

### 5.3 Software Tools

Two software packages were used to solve the mathematical model presented above. PlatingMaster [48] was used for the three-dimensional simulations of initial current density distributions and Elsy [49] for the two-dimensional moving boundary simulations. Both have already been applied successfully to various problems in electrochemistry [35, 50, 51].

# Chapter 6

## Modeling of a Typical PCB

In this chapter, the modeling strategy is applied to a typical PCB design. The PCB is depicted in Fig. 6.1. It is quadratic with a side length of 8.475 mm. The thickness of the copper foil is 17  $\mu\text{m}$  and the thickness of the photolithographic mask is 5  $\mu\text{m}$ .

The PCB design contains pad features and conducting line features. Conducting lines, or traces, are straight or bent lines of copper that function as miniaturized wires. They connect pads, which are designated for the bonding or mounting of electronic components, e.g., integrated circuits. There are two types of pads on this design: circular pads, which are arranged in the central region of the workpiece, and ellipsoidal pads, which are arranged at the brink of the PCB.

In through-mask EMM, evolving features are covered by photolithographic mask. The working electrode is the negative pattern to the emerging PCB. To avoid ambiguity, the photolithographic mask atop of an evolving conducting line, for instance, is referred to as “conducting line feature”. Conducting line features are 40  $\mu\text{m}$  wide, circular pad features have a diameter of 205  $\mu\text{m}$  and ellipsoidal pad features are 90  $\mu\text{m}$  wide.

The polarization function  $f(\eta)$  was assumed to be linear, which implies a constant charge-transfer resistance. In all computations, the charge-transfer resistance was  $10^{-6} \Omega \text{ m}^2$  and the conductivity of the electrolyte was  $30 \text{ S m}^{-1}$ , which is typical for a sulfuric copper sulfate electrolyte.

Computations were carried out on a 2.67 GHz dual-core, 2 GB RAM personal computer.

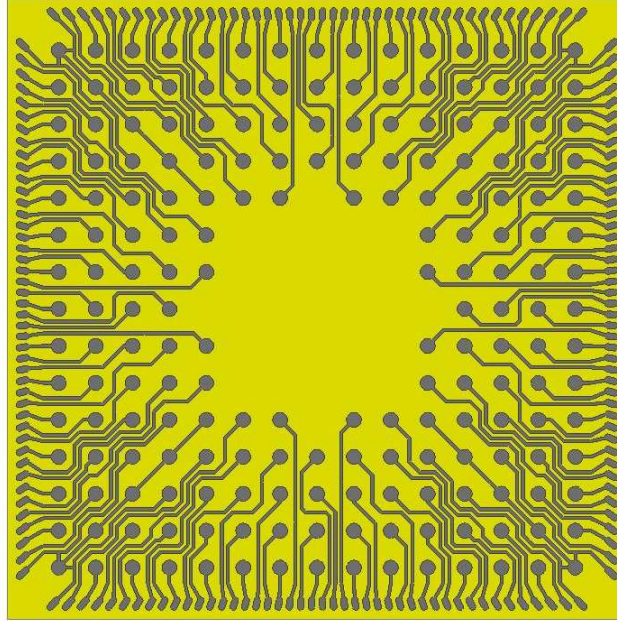


Figure 6.1: PCB design. Electrode surfaces are colored yellow and photoresist surfaces gray.

## 6.1 Simulations without Consideration of Auxiliary Means

This section is dedicated to investigate and interpret the current density distribution and the shape evolution for the given workpiece and given electrochemical parameters. The problem of applying appropriate auxiliary means to prevent a non-uniform distribution will be tackled in Sec. 6.2.

### 6.1.1 Macroscopic Modeling

A raster of  $17 \times 17$  quadratic elements was chosen to determine the active area density distribution. Each raster element has a side length of  $498.5 \mu\text{m}$ . Fig. 6.2 shows the PCB design and the raster and Fig. 6.3 shows the concluding active area density distribution. The minimum of active area density is 0.542, which is definitely not as low as to break the accuracy of the active area density model down (see discussion of the accuracy in Chap. 7). It will be shown in section 6.1.2 that mesoscopic scopes are

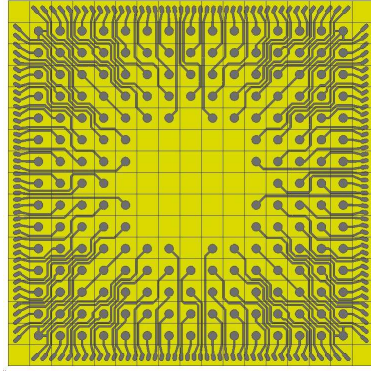


Figure 6.2: PCB design and raster.

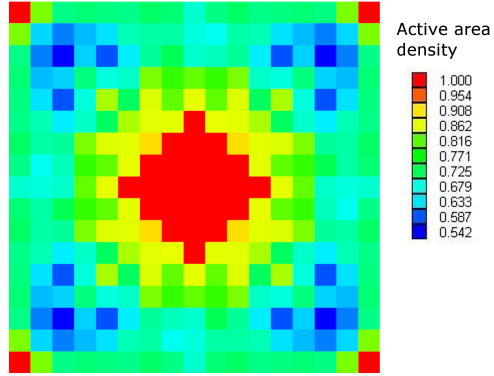


Figure 6.3: Active area density distribution of the PCB according to Fig. 6.2.

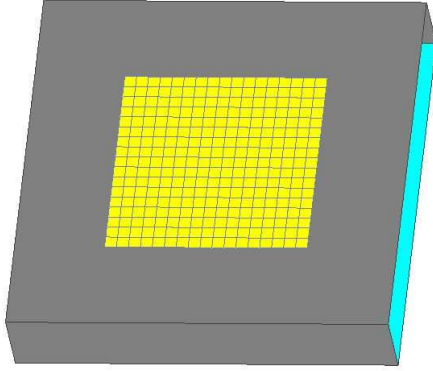


Figure 6.4: Macroscopic reactor. The working electrode is colored yellow, the counter electrode is colored blue and insulating surfaces are either transparent or colored gray.

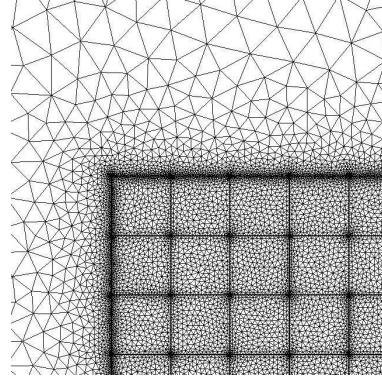


Figure 6.5: A part of the surface mesh of the macroscopic reactor in Fig. 6.4.

appropriate. The raster is thus neither too fine nor too coarse.

The macroscopic reactor is a square box with a side length of 16 mm and a height of 3 mm. The working electrode, which is the anode, is positioned in the middle of the base and the counter electrode fills the opposite square. The reactor was discretized with a mesh of 706,032 nodes and 3,834,734 elements and the computation time was 74 s. Fig. 6.4 pictures the reactor and Fig. 6.5 shows a part of its surface mesh.

The macroscopic current density distribution is depicted in Fig. 6.6. It is emphasized that normalized current density distributions do not depend on the mean current density if the charge-transfer resistance is constant. Hence, the mean current density does not need to be stated. The

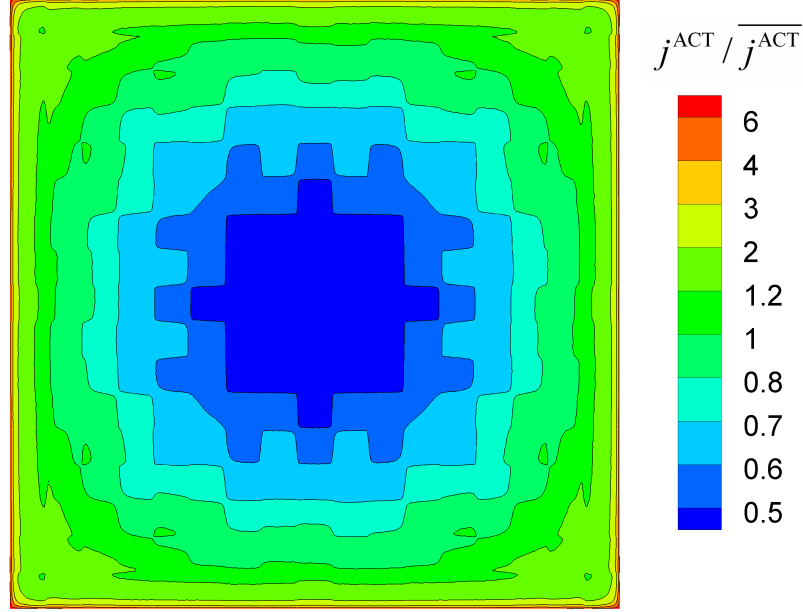


Figure 6.6: Macroscopic current density distribution of  $j^{\text{ACT}}$ , normalized to the mean current density. Maximum 12.20, minimum 0.456.

distribution is significantly non-uniform: The maximum current density is about 12 times the mean current density. One may already foretell qualitatively that this will result in a significantly non-uniform shape evolution causing loss of electrical contact.

The macroscopic current density distribution is predominantly influenced by the migrational flux of the solute species and not by the polarization resistance, because the latter is smaller than the resistance of the ohmic pathways. This finding is already evident from the non-uniform characteristic of the current density distribution. It is confirmed by Wagner's number:  $W_a = 3.5 \cdot 10^{-3}$  for the system at hand, where  $l$  is the width of the PCB. For such a low  $W_a$ , one may classify the distribution as almost primary. In the central region, the influence of variations in active area density plays a role. The resistance of the current tubes is nearly constant there, and the current density distribution consequently reflects the piece-wise characteristic of the active area density distribution (see Sec. 3.2.1).

Q1	Q2	Q3	Q4	Q5	Q6	Q7	Q8	Q9	Q10	Q11	Q12	Q13	Q14	Q15	Q16	Q17
P1	P2	P3	P4	P5	P6	P7	P8	P9	P10	P11	P12	P13	P14	P15	P16	P17
O1	O2	O3	O4	O5	O6	O7	O8	O9	O10	O11	O12	O13	O14	O15	O16	O17
N1	N2	N3	N4	N5	N6	N7	N8	N9	N10	N11	N12	N13	N14	N15	N16	N17
M1	M2	M3	M4	M5	M6	M7	M8	M9	M10	M11	M12	M13	M14	M15	M16	M17
L1	L2	L3	L4	L5	L6	L7	L8	L9	L10	L11	L12	L13	L14	L15	L16	L17
K1	K2	K3	K4	K5	K6	K7	K8	K9	K10	K11	K12	K13	K14	K15	K16	K17
J1	J2	J3	J4	J5	J6	J7	J8	J9	J10	J11	J12	J13	J14	J15	J16	J17
I1	I2	I3	I4	I5	I6	I7	I8	I9	I10	I11	I12	I13	I14	I15	I16	I17
H1	H2	H3	H4	H5	H6	H7	H8	H9	H10	H11	H12	H13	H14	H15	H16	H17
G1	G2	G3	G4	G5	G6	G7	G8	G9	G10	G11	G12	G13	G14	G15	G16	G17
F1	F2	F3	F4	F5	F6	F7	F8	F9	<b>F10</b>	F11	F12	F13	F14	F15	F16	F17
E1	E2	E3	E4	E5	E6	E7	E8	E9	E10	E11	E12	E13	E14	E15	E16	E17
D1	D2	D3	D4	D5	D6	D7	D8	<b>D9</b>	D10	D11	D12	D13	D14	D15	D16	D17
C1	C2	C3	C4	C5	C6	C7	C8	C9	C10	C11	C12	C13	C14	C15	C16	C17
B1	<b>B2</b>	B3	B4	B5	<b>B6</b>	B7	B8	B9	B10	B11	B12	B13	B14	B15	B16	B17
A1	<b>A2</b>	A3	A4	A5	A6	A7	A8	A9	A10	A11	A12	A13	A14	A15	A16	A17

Figure 6.7: Names of the raster elements on the PCB, according to the orientation of the workpiece in Figs. 6.1, 6.2 and 6.3. The five raster elements discussed in the following are marked with bold lines.

### 6.1.2 Mesoscopic Modeling

The raster elements composing the workpiece are named as given in Fig. 6.7; the orientation of the raster in this figure corresponds to the orientation of the workpiece in Figs. 6.1, 6.2 and 6.3.

Simulations of several raster elements are presented in this section. The elements D9, F10 and A2 were chosen to investigate the influence of the frame in detail. Additionally, the current density distributions on the elements B2 and B6 were computed because they contain trenches which will be modeled in section 6.1.3.



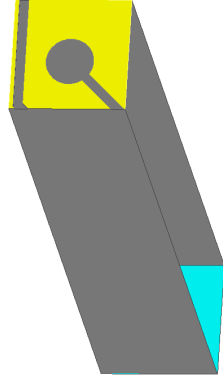


Figure 6.8: Mesoscopic reactor for raster element D9. The working electrode is colored yellow, the counter electrode blue and insulating surfaces are either transparent or colored gray.

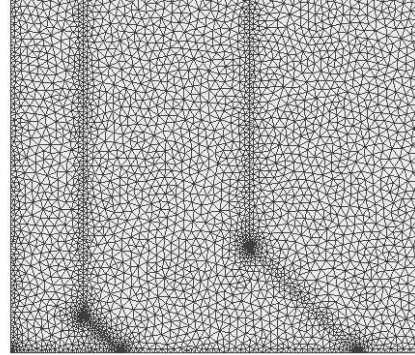


Figure 6.9: A part of the surface mesh of the mesoscopic reactor in Fig. 6.8.

### Raster Element D9

Fig. 6.8 depicts the mesoscopic reactor for the simulation of raster element D9 without using a frame. It is a square box with a height of 3 mm, which equals the height of the macroscopic reactor. The mesoscopic section of the workpiece considered in the simulation, which is as a start the raster element, fills the base and the counter electrode fills the opposite square. The reactor was discretized with 136,291 nodes and 697,472 elements, and the computing time was 15 s. Fig. 6.9 shows a part of the surface mesh on the working electrode.

Fig. 6.10 depicts the current density distribution on the raster element. It is more uniform than the macroscopic distribution. The maxima of current density occur similarly at corners and edges of the electrode surfaces but they are not as pronounced as in the macroscopic simulation. The explanation is given by Wagner's number. The charge-transfer resistance and the conductivity are evidently the same as used in Sec. 6.1.1, whereas  $l$  equals the width of the mesoscopic reactor. I.e.,  $W_a = 6 \cdot 10^{-2}$  which means a more uniform distribution. This is a scaling effect: The mesoscopic reactor contains only a section of the workpiece and is thus on a different length scale than the macroscopic distribution.

As was discussed in section 5.1.2, a false current density distribution near the border of the raster element is to be expected if the mesoscopic reactor considers none of the element's surroundings. In fact, two maxima occur at the border of the element which are evidently erroneous.



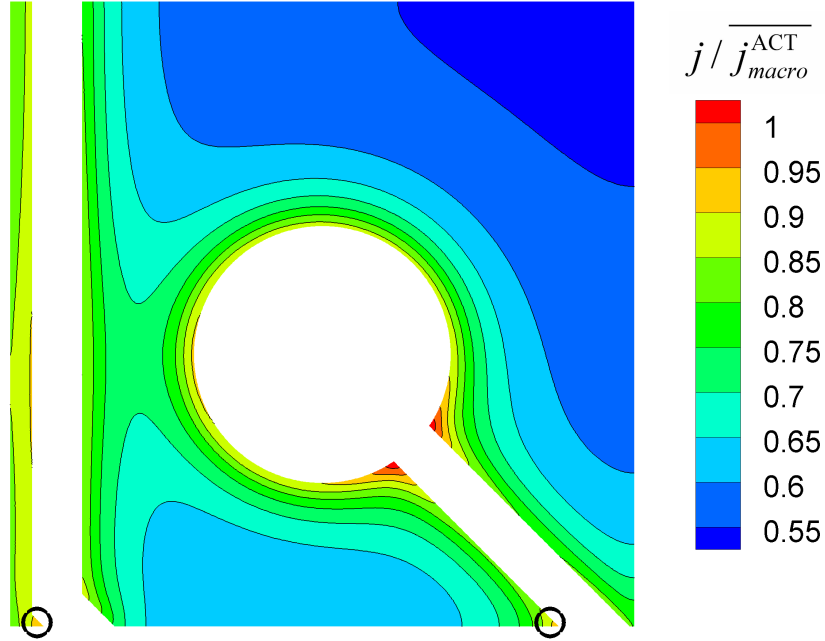


Figure 6.10: Mesoscopic current density distribution on raster element D9 obtained without a frame. The distribution is normalized to the mean  $\overline{j}^{ACT}$  of the macroscopic distribution (Fig. 6.6). Maximum 1.032, minimum 0.539.

They are encircled in Fig. 6.10. These maxima are situated at two corners which were created by cutting off the surroundings. The conducting line features, at which border the maxima appear, continue after they cross the border. These corners are not real and the maxima are thus erroneous. Furthermore, the minimum of the current density distribution is situated exactly at the upper right corner in Fig. 6.10. It would be a very improbable coincidence if the minimum would be found in reality exactly at a crosspoint of the raster.

According to section 5.1.2, a frame was introduced into the simulations. Fig. 6.11 depicts the size of the frames 1-4. The width of these frames are 1.1, 1.25, 1.5 and 2 times the width of the raster element. The width of frame 5 is three times the width of the raster element and it thus comprises the eight neighboring raster elements. Simulations were performed for all five frames. The reactor with frame 5 was discretized with 209,876 nodes and 1,089,412 elements and the computing time was 77 s. The results are visualized in Fig. 6.12, which shows the current density along the solid black line in Fig. 6.11. The blue line represents the current density distribution if no frame is used, corresponding to

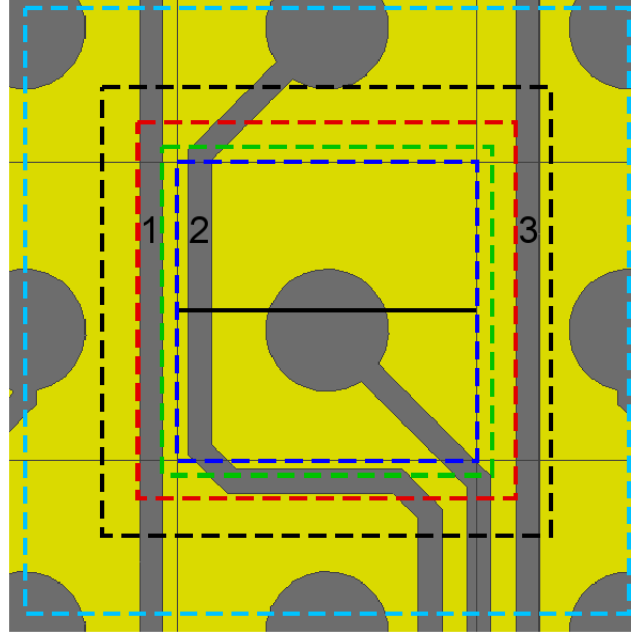


Figure 6.11: Mesoscopic regions considered in the simulation of raster element D9. Blue line: raster element D9, green line: frame 1, red line: frame 2, black line: frame 3, cyan line: frame 4. The solid black line indicates the position of the cross-section in Fig. 6.15. Conducting line features 1, 2 and 3 are indicated by numbers.

Fig. 6.10.

The current density distribution with frame 1 significantly deviates from the distribution without a frame in the left part of the raster element (Fig. 6.12). The narrow strip of electrode surface on the left receives less current density if the additional surrounding area is taken into account. One can interpret this behavior by looking at the resistance of the respective current tubes. The current tube of the strip of electrode surface is enlarged by the conducting line feature to its right (conducting line feature 2, see Fig. 6.11) like the current tube B in Fig. 3.1 is enlarged by the insulating wall neighboring the electrode. The electrode area to the left of the raster element taken into account by frame 1 receives some of the flux density which is provided by the enlarged ohmic pathway caused by conducting line feature 2. If no frame is used, this additional flux density is received by the narrow strip of the raster element. Hence, the current density there is lowered by introducing frame 1.

In comparison with frame 1, frame 2 additionally accounts for conducting line feature 1, which is located to the left of the raster element

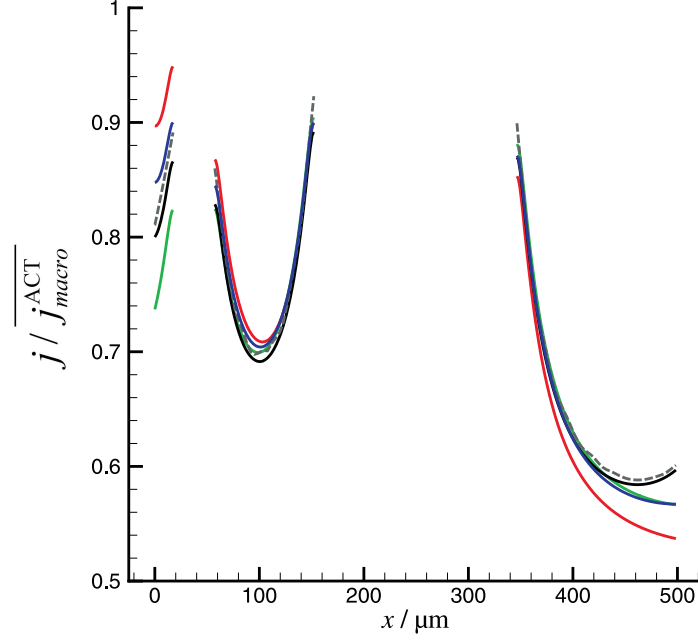


Figure 6.12: Cross-section of the current density distributions along the solid black line in Fig. 6.11, normalized to the mean  $j^{\text{ACT}}$  of the macroscopic distribution (Fig. 6.6). Blue line: without frame, green line: frame 1, red line: frame 2, black line: frame 3, gray dashed line: direct simulation (see Chap. 7).

(see Fig. 6.11). The strip of electrode near the left border of the raster element now receives significantly more current density. Conducting line feature 1 provides an enlarged ohmic pathway for this electrode surface. Thus, the current density is larger there compared to the computations not considering conducting line feature 1. At the right border of the cross-section, the current density is lowered by introducing frame 2. This is due to the same reason as was discussed for frame 1. The additionally considered electrode surface to the right consumes some of the flux density which is provided by the enlarged ohmic pathway caused by the pad feature, stealing it away from the electrode at the right border. This effect also exists for frame 1, but is not as pronounced as to be apparent in the current density distribution.

Frame 3 covers conducting line feature 3, which is located to the right of the raster element. According to what was discussed for frame 1 and 2, this additionally considered photoresist surface enlarges the current density at the right border of the raster element. In comparison with frame 2, the additionally considered electrode surface on the left lowers

the current density received by the narrow strip of electrode on the raster element.

The cross-sections of the current density distributions yielded with frame 4 and 5 are identical within the line thickness with the distribution yielded with frame 3 (black line in Fig. 6.12). It is concluded that with respect to this cross-section, frame 3 is large enough to account for the influence of the geometric factors of the surrounding features. Features outside of frame 3 do not have a significant effect. It is emphasized that the situation may change if another cross-section or the entire two-dimensional current density map is discussed. The question which frame size is sufficient will be tackled quantitatively in Chap. 7.

Fig. 6.13 depicts the current density distribution computed with frame 5. The erroneous maxima which occurred at the border without using a frame have vanished, and the minimum of the current density has shifted away from the corner. Furthermore, the contour lines in the upper left part bend to the right, which is consistent with the bending of the conducting line feature to  $45^\circ$  right above the element's border. This behavior cannot be yielded from the simulation without a frame.

It can be clearly seen from Fig. 6.12 and from comparing Figs. 6.10 and 6.13 that the distribution in the central region remains almost unchanged by introducing and varying the frame. In contrast, the distribution in the border region may change drastically. The changes which arise from taking into account additional surrounding areas can be explained by considering the ohmic pathways of the electrode surfaces. It is evident that the accuracy is improved and that introducing a frame prevents a false distribution in the border region. For a quantitative discussion of the accuracy, see Chap. 7.

### **Raster Element F10**

There are only few features around raster element F10 (see Fig. 6.14). Aside from the conducting line feature protruding from the raster element, there are merely four pad features in the surroundings and they are relatively far away compared to the conducting line features neighboring element D9. It is thus expected that the influence of the surrounding areas considered by the frames will not have a large impact. As for element D9, five different frames were investigated. They have the same

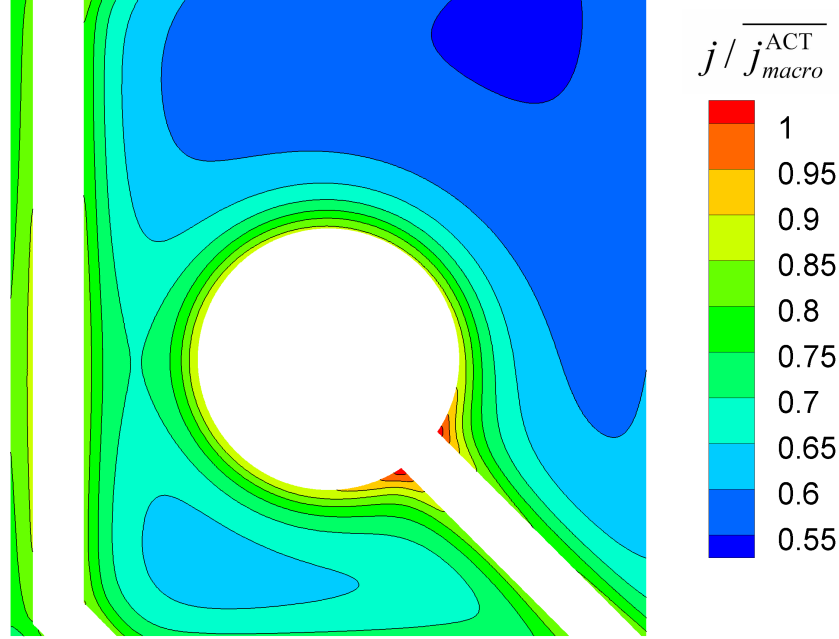


Figure 6.13: Mesoscopic current density distribution on raster element D9 obtained with frame 5. The distribution is normalized to the mean  $j^{\text{ACT}}$  of the macroscopic distribution (Fig. 6.6). Maximum 1.029, minimum 0.546.

names and sizes as for element D9, and aside from frame 5 they are depicted in Fig. 6.14.

The reactor considering only the raster element was discretized with 83,933 nodes and 422,600 elements and the reactor with frame 5 with 219,449 nodes and 1,151,324 elements. The computing times were 8 and 29 s.

Fig. 6.15 shows the current density distribution along the solid black line in Fig. 6.14. This line is placed close to the lower border of the raster element. A cross-section which lies entirely in the border region of the element should in general be influenced much more by the frame size than the cross-section of element D9 in Fig. 6.12. However, the distributions show only minor variations for different frame sizes. The black line for frame 3 is almost totally covered by the red line for frame 2, and the same holds for frames 4 and 5. The simulations using the latter are thus not depicted in Fig. 6.15. Only in the very left part of the cross-section, the current density decreases with increasing frame size. As was discussed for raster element D9, the additionally considered electrode surface to the left of the element lowers the current density in the respective border

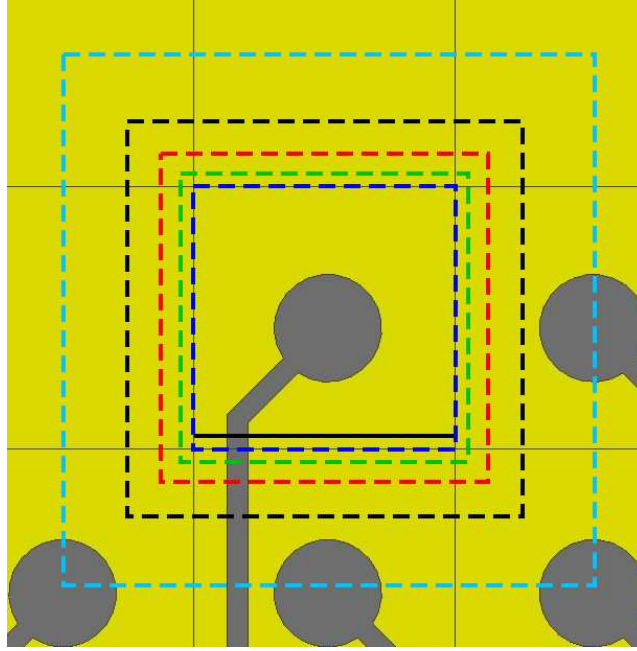


Figure 6.14: Mesoscopic regions considered in the simulation of raster element F10. Blue line: raster element F10, green line: frame 1, red line: frame 2, black line: frame 3, cyan line: frame 4. The solid black line indicates the position of the cross-section in Fig. 6.15.

region.

If the pad features surrounding the element had an effect on the raster element's current density distribution, they would certainly affect the lower part of the element. However, no change in the cross-section of the current density distribution is observed when going from frame 3 to frame 4 and 5, although only the latter account for the pad features. This confirms what was found for the cross-section of element D9: Features outside of frame 3 do not have a significant effect on the current density distribution.

The current density distribution on element F10 without using a frame is depicted in Fig. 6.16. In element D9, a significantly distorted current density distribution was obtained around the protruding conducting line features if no frame was used. There is no distortion, such as erroneous maxima, around the conducting line feature protruding from element F10 because it crosses the border perpendicularly. Linear conducting line features and the current density distributions around them have a mirror plane perpendicular to the running direction. Cutting off a

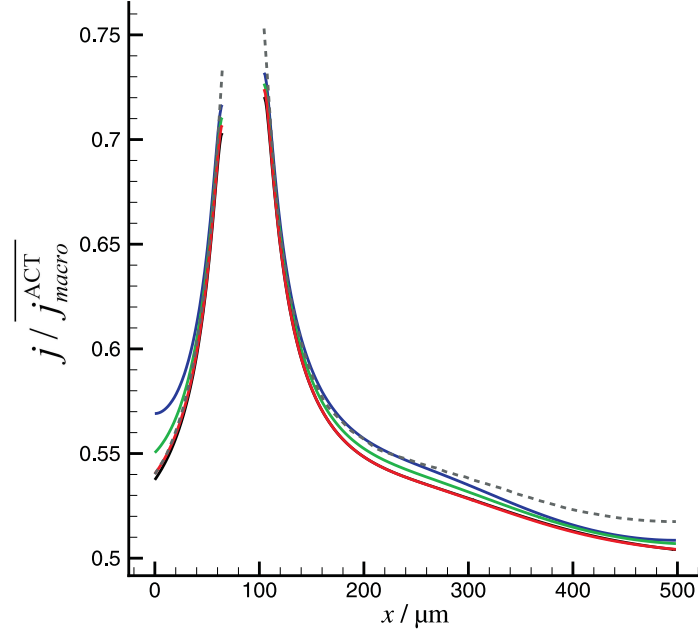


Figure 6.15: Cross-section of the current density distributions along the solid black line in Fig. 6.14, normalized to the mean  $j^{\text{ACT}}$  of the macroscopic distribution (Fig. 6.6). Blue line: without frame, green line: frame 1, red line: frame 2, black line: frame 3, gray dashed line: direct simulation (see Chap. 7).

partly linear conducting line feature in perpendicular direction will thus have a minor impact.

Because the protruding feature is perpendicular to the border and because the other features are far away, the mesoscopic simulation of raster element F10 may be performed with a very small frame or even without a frame. Introducing a frame brings only a minor benefit, as can be seen from comparing the current density distribution obtained without a frame (Fig. 6.16) and the distribution obtained with frame 5 (Fig. 6.17).

## Raster Element A2

Raster element A2 lies on the border of the workpiece. The lower border of the element is a part of the PCB's border (see Fig. 6.18). The same frame sizes and names are used as for the raster elements before and aside from frame 5 they are depicted in Fig. 6.18. The two conducting line features and the pad feature protruding from the element do not

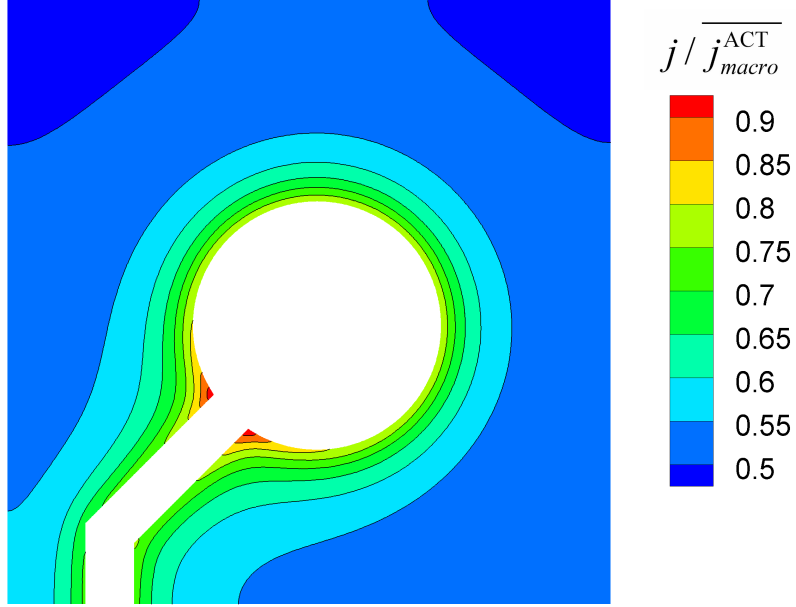


Figure 6.16: Mesoscopic current density distribution on raster element F10 obtained without a frame. The distribution is normalized to the mean  $j^{\text{ACT}}$  of the macroscopic distribution (Fig. 6.6). Maximum 0.930, minimum 0.494.

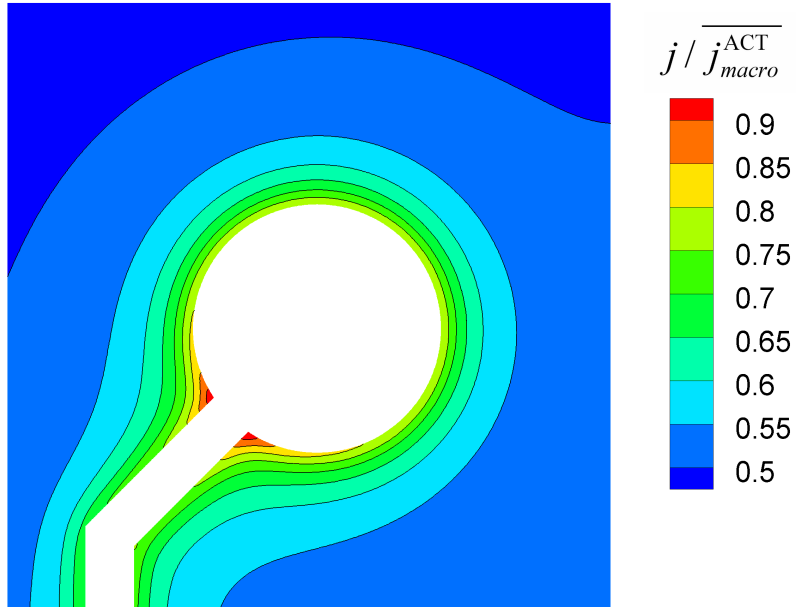


Figure 6.17: Mesoscopic current density distribution on raster element F10 obtained with frame 5. The distribution is normalized to the mean  $j^{\text{ACT}}$  of the macroscopic distribution (Fig. 6.6). Maximum 0.9377, minimum 0.4850.



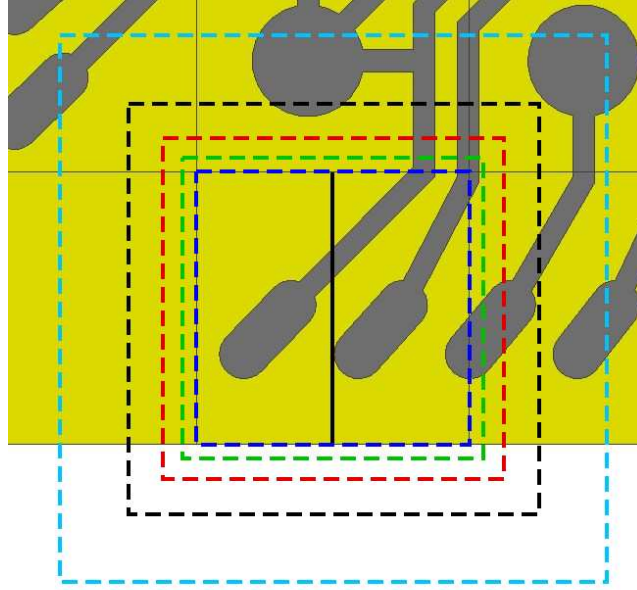


Figure 6.18: Mesoscopic regions considered in the simulation of raster element A2. Blue line: raster element A2, green line: frame 1, red line: frame 2, black line: frame 3, cyan line: frame 4. The solid black line indicates the position of the cross-section in Fig. 6.19.

cross the border perpendicularly. From what was found for element D9, one expects that the current density distribution will be distorted there if no frame is used. The closest feature aside from these three is a pad feature considered from frame 3 on. It is not expected to have a large effect because it is relatively far away. The insulating surface on the lower border of the raster element extends to the side wall of the reactor. It provides a huge ohmic pathway and will probably play a dominant role.

The reactor not using a frame was discretized with 136,690 nodes and 705,354 elements and the reactor using frame 5 was discretized with 227,180 nodes and 1,184,775 elements. The computing times were 18 and 31 s.

Fig. 6.19 depicts the cross-section of the current density distributions along the solid black line in Fig. 6.18. The distributions show a clear trend: The larger the frame, the smaller is the current density at the upper part of the element and the larger is the current density at the lower part. This comes from the insulating surface below the raster element. It provides an enlarged flux density to the lower region of the

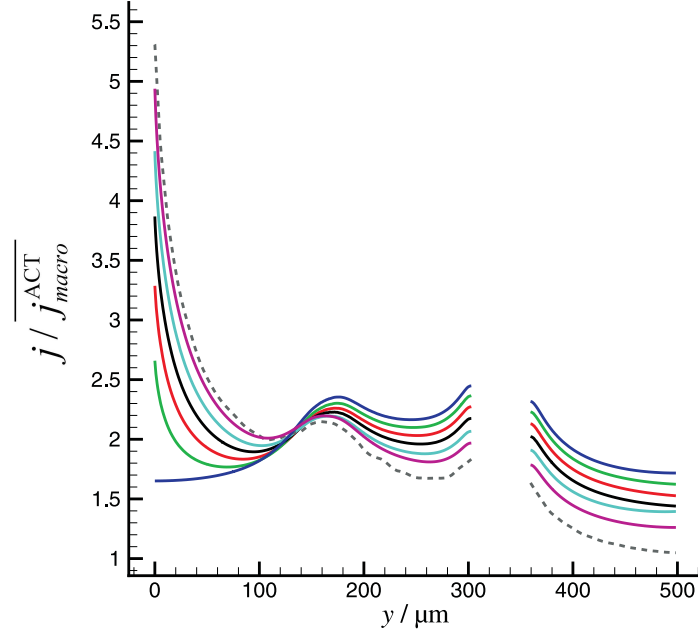


Figure 6.19: Cross-section of the current density distributions along the solid black line in Fig. 6.18, normalized to the mean  $j^{\text{ACT}}$  of the macroscopic distribution (Fig. 6.6). The lower end of the line is on the left of the plot. Blue line: without frame, green line: frame 1, red line: frame 2, black line: frame 3, cyan line: frame 4, magenta line: frame 5, gray dashed line: direct simulation (see Chap. 7).

raster element. Because the mean current density is constant, this comes with a decrease of current density at the upper part of the element. This effect is much more pronounced than what was experienced for elements D9 and F10. Furthermore, there is still a significant change when going from frame 4 to frame 5, which means that at least the latter is not large enough. The pad features do not have an observable effect on the current density distribution.

For the cross-sections of the elements D9 and F10, it was found that additionally considered regions outside of frame 3 do not play any role. Obviously, this does not hold for the insulating surface extending to the border of the reactor. This is a matter of magnitude: The ohmic pathway provided by a feature is much smaller than the one provided by this insulating surface. The smaller the additional ohmic pathway, the smaller is the range where it influences the current density distribution significantly. Concerning the insulating surface embedding the workpiece, the frame would have to range to the border of the macroscopic reactor to fully reflect its influence.

Figs. 6.20 and 6.21 show the current density distributions on the raster element without a frame and with frame 5. The major difference is caused by the insulating surface below the PCB. It shifts the maximum of current density to the lower border of the raster element. According to element D9, the computation without a frame shows a false behavior of the current density distribution where the features cross the border. Maxima of current density, which are caused by cutting off the surroundings and thus erroneous, are observed there. The simulation with frame 5 shows a reliable behavior of the current density distribution there.

The mesoscopic simulation of raster element A2 requires a frame which is as large as possible. Evidently it may not range to the side wall of the reactor because this would mean an infeasible simulation. This finding shows that the question of choosing an appropriate frame is sophisticated. The size of the appropriate frame may vary from the raster element's size to dimensions of the entire macroscopic reactor. But keeping in mind what was learned from the mesoscopic simulations of these three elements, one may intuitively choose an appropriate frame size from contemplating the surroundings. This qualitative discussion will be quantified by comparison with a direct simulation in Chap. 7.

### **Raster Elements B2 and B6**

The current density distributions on the raster elements B2 and B6 are modeled because they contain trenches which will be of interest in the next section. A discussion of the frame's size is not of interest here and hence, the computations were only performed with frame 5. The reactor for element B2 was discretized with 287,423 nodes and 1,510,619 elements, and the reactor for element B6 with 281,296 nodes and 1,476,367 elements. The computing times were 47 and 54 s. The current density distributions are depicted in Figs. 6.22 and 6.23.

### **6.1.3 Microscopic Modeling**

All trenches on the workpiece are 41.25  $\mu\text{m}$  wide and neighbored by two conducting line features which are 40  $\mu\text{m}$  wide. Three trenches were chosen to investigate their shape evolution. Fig. 6.24 names these trenches and shows their position on the workpiece. Trench 1 is situated close to

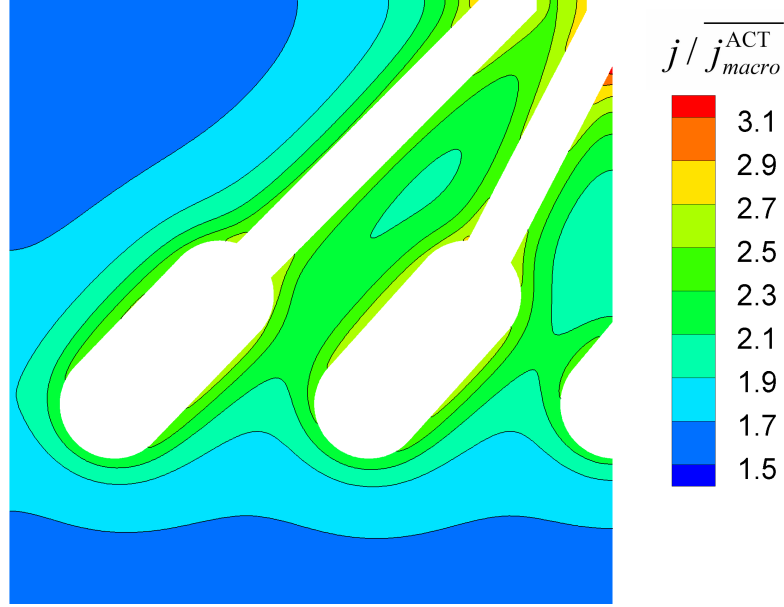


Figure 6.20: Mesoscopic current density distribution on raster element A2 obtained without a frame. The distribution is normalized to the mean  $j^{\text{ACT}}$  of the macroscopic distribution (Fig. 6.6). Maximum 3.203, minimum 1.560.

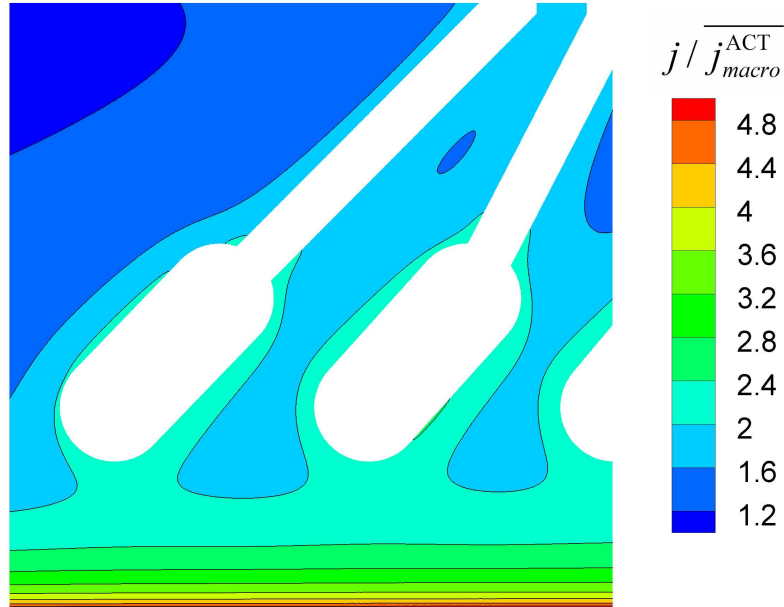


Figure 6.21: Mesoscopic current density distribution on raster element A2 obtained with frame 5. The distribution is normalized to the mean  $j^{\text{ACT}}$  of the macroscopic distribution (Fig. 6.6). Maximum 4.980, minimum 1.139.

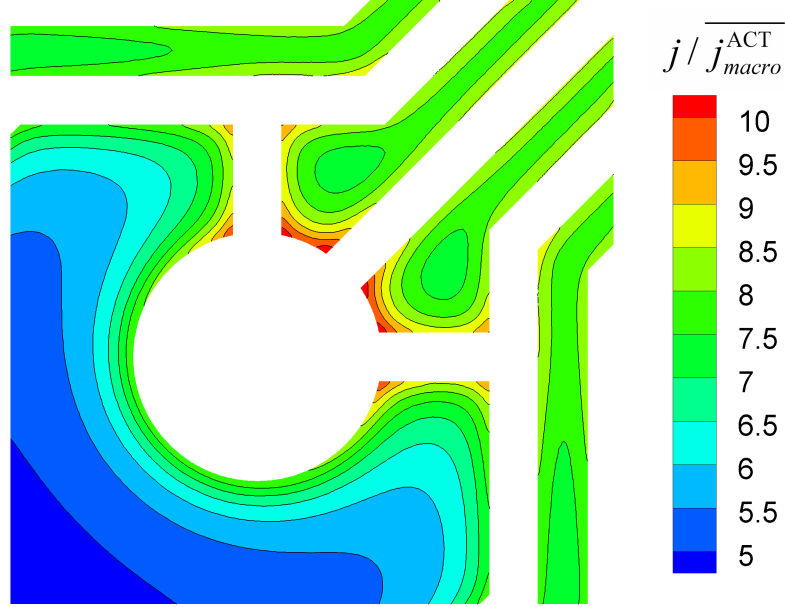


Figure 6.22: Mesoscopic current density distribution on raster element B2 obtained with frame 5. The distribution is normalized to the mean  $j^{\text{ACT}}$  of the macroscopic distribution (Fig. 6.6). Maximum 10.392, minimum 4.758.

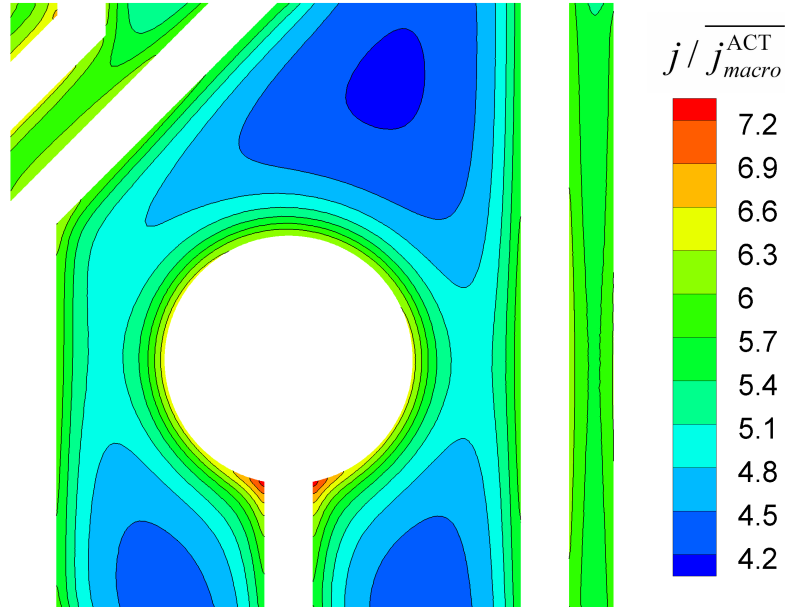


Figure 6.23: Mesoscopic current density distribution on raster element B6 obtained with frame 5. The distribution is normalized to the mean  $j^{\text{ACT}}$  of the macroscopic distribution (Fig. 6.6). Maximum 7.316, minimum 4.164.

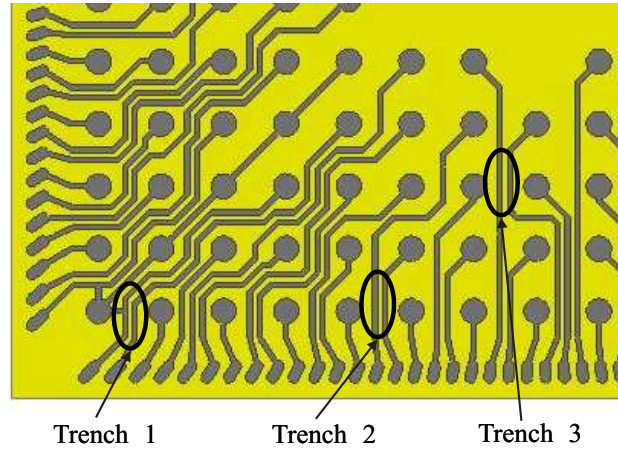


Figure 6.24: Trenches chosen for the microscopic simulations, named trench 1–3.

the corner and trench 2 close to the edge, whereas trench 3 is located in the middle region of the workpiece. From the characteristic of the non-uniformity of the macroscopic current density distribution and the position of the trenches one may already tell qualitatively that trench 1 will have the largest mean current density and that trench 3 will have the lowest mean current density.

Because the distance from the trench in question to the neighboring trenches is equal for all trenches of this PCB, there is a mirror plane in the middle of the cross-section considered in the microscopic modeling. The microscopic reactor thus comprises only half of this cross-section. The width of the reactor is  $40.625\text{ }\mu\text{m}$  and the height is  $0.5\text{ mm}$ . The latter is large enough not to influence the current density distribution on the trench. In Fig. 6.25, the microscopic reactor is pictured with solid lines. The dotted lines indicate the part of the considered cross-section which is not included in the simulation due to the mirror plane. The latter is at the left border of the reactor. Fig. 6.26 depicts the discretization of the microscopic reactor. It consists of 116 elements, and the computing times were between 232 and 856 s. Both the reactor and the mesh were identical in all computations; the difference was solely the total current.

The initial mean current densities of the trenches were evaluated from the mesoscopic current density distributions on the raster elements B2, B6 and D9. They are 1.481 times the mean  $j^{\text{ACT}}$  of the macroscopic distribution for trench 1, 1.139 for trench 2 and 0.849 for trench 3. The

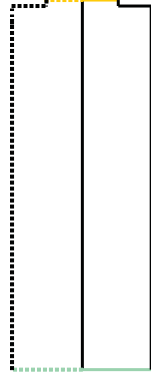


Figure 6.25: Microscopic reactor (drawn with solid lines). The working electrode is colored yellow, the counter electrode blue and insulating surfaces black. The dotted lines indicate the part of the considered microscopic cross-section which does not enter the simulation because of the mirror plane.

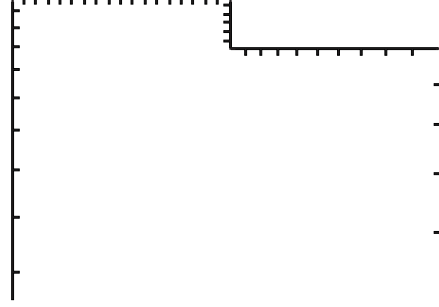


Figure 6.26: A part of the surface mesh of the microscopic reactor, placed in the same orientation as Fig. 6.25.

simulations were performed for three different points in time, namely those points when the insulating support of the different trenches is exposed to the electrolyte.

The initial current density distribution of the microscopic simulation of trench 1 is shown in Fig. 6.27. It is compared to the cross-section of the mesoscopic current density distribution, from which the initial mean current density was determined (Fig. 6.22). The microscopic reactor covers only half of the trench, which is why the microscopic distribution is mirrored at the left border of the reactor. This allows for a better comparison with the mesoscopic distribution. The latter is somewhat asymmetric, but the deviation from the symmetric microscopic distribution is minor. This confirms that considering only half of the adjacent photoresist in the microscopic reactor is a good approximation.

Due to the scaling effect discussed in Sec. 6.1.2, the microscopic current density distribution is more uniform than those on the macroscopic and mesoscopic scale. The characteristic length  $l$  on the microscopic scale equals the width of the trenches, 41.25  $\mu\text{m}$ , which results in  $W_a = 0.74$ . Discussing the uniformity of the distributions on the different scales with respect to  $W_a$  gives a demonstrative example of how this criterion reflects the effect of scaling.

Fig. 6.28 depicts the etch profiles of the three trenches at the three

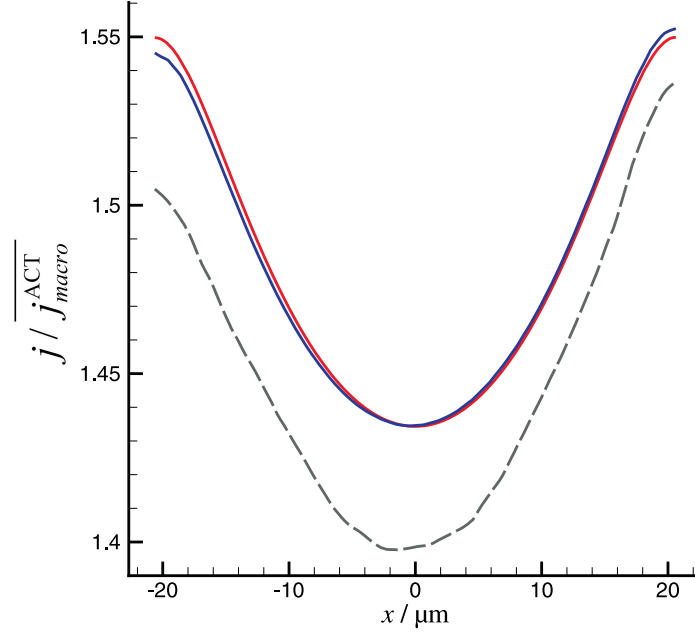


Figure 6.27: Initial current density distribution on trench 1. Red line: microscopic simulation (maximum 1.550, minimum 1.434), blue line: mesoscopic simulation, gray dashed line: direct simulation (see Chap. 7).

points in time. The gray rectangle symbolizes the photolithographic mask and the dashed horizontal line indicates the insulating support. The vertical dot and dash line borders the region into which the metal wall profile may penetrate due to the evolution of the neighboring trench (see Sec. 5.1.3). The colored lines are the metal wall profiles for the given points in time.

The insulating support is exposed in trench 1 after 312 s, in trench 2 after 405 s and in trench 3 after 544 s. These times correspond to a mean macroscopic current density of  $j^{\text{ACT}} = 1000 \text{ A/m}^2$ . The shape evolution is significantly non-uniform: The metal wall profile of trench 1 has crossed the dot and dash line, which means the copper is completely etched off at this trench, even before the insulating support is exposed in trench 3. Under these conditions, the process will surely suffer from loss of electrical contact. Because the etching rate at the edge of the workpiece is higher than the etching rate at trench 1, the loss of contact will occur there and the machining process will stop in reality before the insulating support is exposed in trench 1.



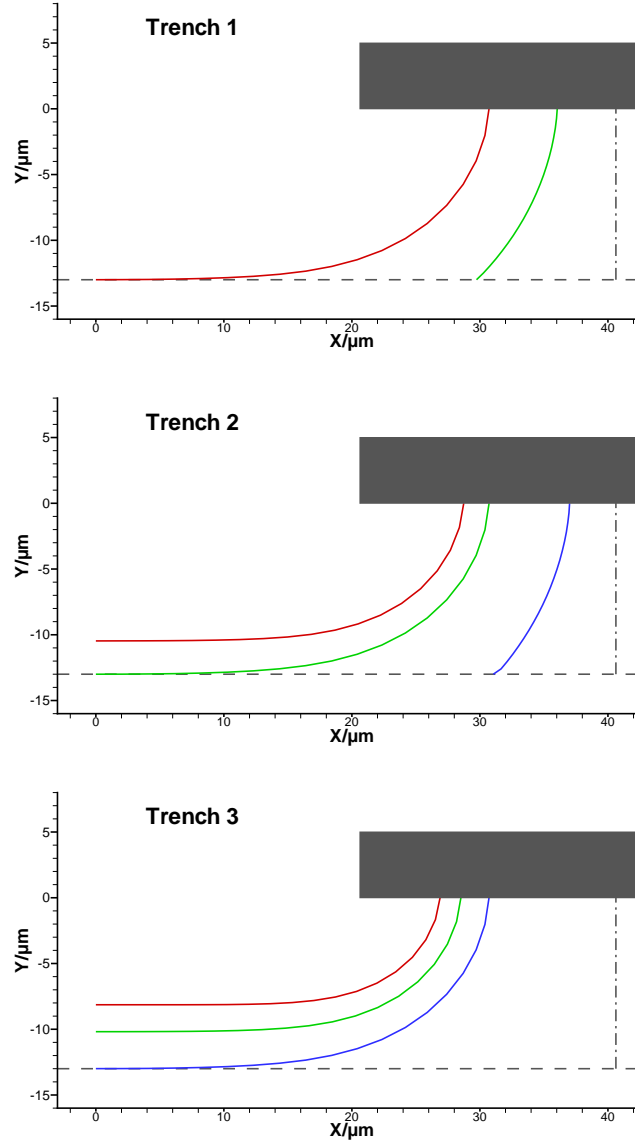


Figure 6.28: Microscopic shape evolution of trenches 1–3 for different points in time. Red line: etch profile at 312 s (insulating support exposed in trench 1); green line: etch profile at 405 s (insulating support exposed in trench 2); blue line: etch profile at 544 s (insulating support exposed in trench 3).

## 6.2 Simulations Considering an Auxiliary Electrode

This section is dedicated to the governing and direction of the current density distribution over the given PCB in order to prevent loss of electrical contact. An auxiliary electrode will be included into the modeling strategy and optimized with respect to the uniformity of the current density distribution.

The mesoscopic and the microscopic modeling steps are performed in the same way as if no auxiliary electrode was included (Secs. 6.1.2 and 6.1.3), only the input for the mean current density changes. The macroscopic modeling accounts for the auxiliary electrode, and the optimization of the latter is performed there. The electrochemical parameters, namely the conductivity of the electrolyte and the charge-transfer resistance, and the dimensions for the macroscopic reactor are evidently the same as in Sec. 6.1.

### 6.2.1 Macroscopic Modeling

The auxiliary electrode is coplanar to the workpiece and has the shape of a picture frame enclosing the latter (Fig. 6.29). The parameters of the auxiliary electrode are its width  $w$ , its distance from the workpiece  $d$  and its mean current density  $I$ . The latter is given in units of the mean current density of the workpiece, and thus non-dimensional. Because  $I$  is an unambiguous function of the potential of the auxiliary electrode, an optimization of  $I$  also means an optimization of the potential. The parameters of the base case of the optimization were  $w = 1$  mm,  $d = 0.15$  mm and  $I = 1.88$ . These values were not chosen arbitrarily, but on the basis of some preliminary simulations. They are pre-optimized and thus very favorable parameters, as will be shown in the course of this section.

The macroscopic reactor with the base case auxiliary electrode is depicted in Fig. 6.29. Significantly more nodal points were used in the discretization of this reactor due to the auxiliary electrode: The mesh consists of 1,486,944 nodes and 8,069,343 elements. A part of the surface mesh is shown in Fig. 6.30. The computing time was 333 s.

Fig. 6.31 shows the macroscopic current density distribution com-

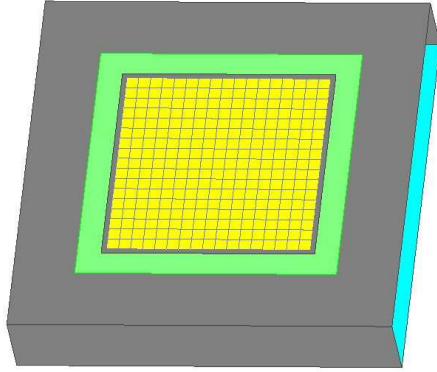


Figure 6.29: Macroscopic reactor with base case auxiliary electrode. The working electrode is colored yellow, the auxiliary electrode green, the counter electrode blue and insulating surfaces are either transparent or colored gray.

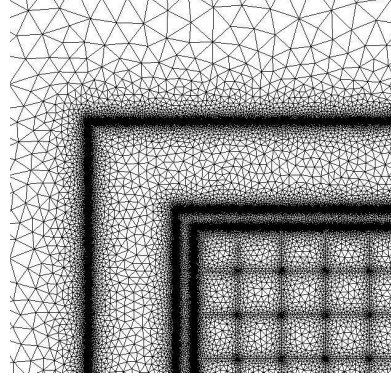


Figure 6.30: A part of the surface mesh of the reactor in Fig. 6.29.

puted with the base case auxiliary electrode. It is significantly more uniform than the distribution obtained without auxiliary means (Fig. 6.6), having a maximum of 1.321 and a minimum of 0.706 times the mean current density.

Wagner's number is not appropriate here to judge the uniformity of the current density distribution, because it does not include parameters of the auxiliary electrode. It is equal for the macroscopic distributions obtained with and without the auxiliary electrode. The distribution in Fig. 6.31 is predominantly influenced by variations of the active area density. As was discussed in Sec. 3.2.1, this results in a current density distribution mirroring the active area density distribution. In this case, this means a piece-wise constant current density distribution. In Fig. 6.6, the resistance of the current tubes was only similar in the middle of the workpiece, whereas here they are similar on the entire workpiece. This is because the current tube of the auxiliary electrode takes the role of current tube B in Fig. 3.1, and the current tubes on the workpiece resemble the central tubes, such as tube A.

### Optimization of the auxiliary electrode

The parameters of the auxiliary electrode  $w$ ,  $d$  and  $I$  are optimized with respect to the uniformity of the macroscopic current density distribution on the workpiece. The criterion for the uniformity of the distribution  $\delta$

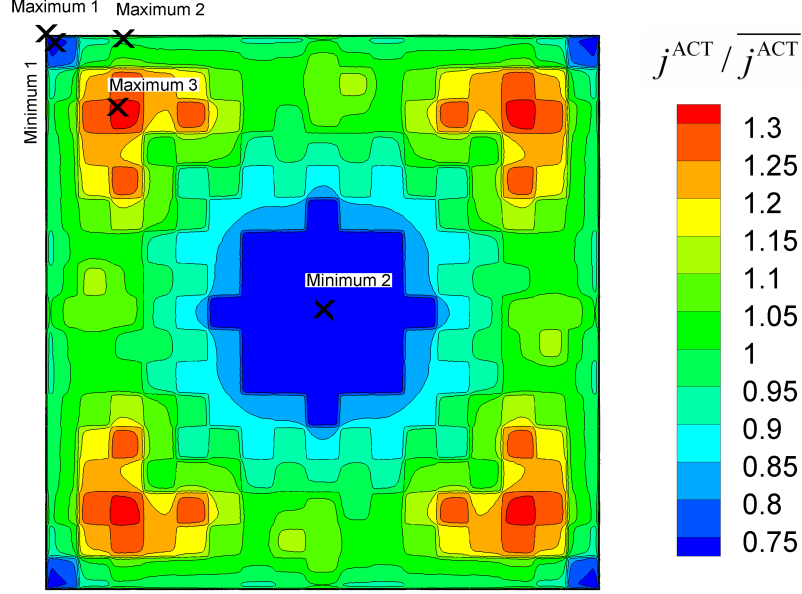


Figure 6.31: Normalized macroscopic current density distribution of  $j^{\text{ACT}}$  with the base case auxiliary electrode. Maximum 1.321, minimum 0.706.

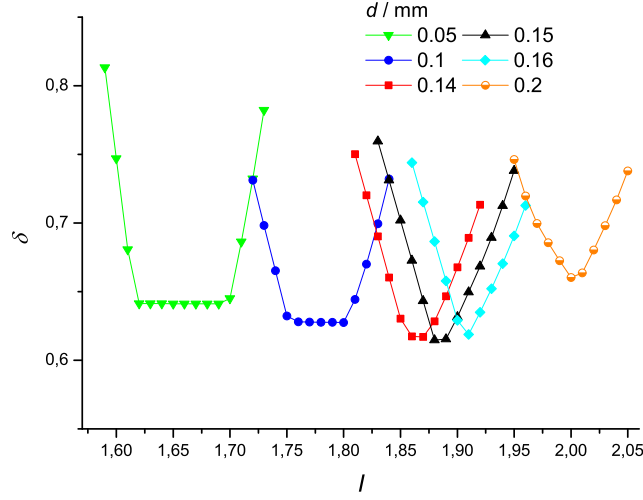
is defined as

$$\delta := \frac{j_{\max}^{\text{ACT}} - j_{\min}^{\text{ACT}}}{\overline{j^{\text{ACT}}}}, \quad (6.1)$$

where  $j_{\max}^{\text{ACT}}$  is the maximum,  $j_{\min}^{\text{ACT}}$  the minimum and  $\overline{j^{\text{ACT}}}$  the mean current density. The smaller  $\delta$  the more uniform is the current density distribution. Another criterion used in literature is the normalized mean-root-square deviation of the current density from its average (e.g., [44])

$$\sigma^2 := \frac{1}{A} \iint_{\mathcal{W}} \left( \frac{j^{\text{ACT}} - \overline{j^{\text{ACT}}}}{\overline{j^{\text{ACT}}}} \right)^2 dx dy, \quad (6.2)$$

which is a normalized surface integral over the workpiece surface  $\mathcal{W}$ , formulated here for a plane workpiece.  $A$  is the norm of the integral (i.e., the area of the workpiece),  $j^{\text{ACT}}$  the current density at the point  $(x, y)$ ,  $\overline{j^{\text{ACT}}}$  the mean current density and  $x$  and  $y$  are the Cartesian coordinates on the workpiece plane. In contrast to  $\sigma^2$ ,  $\delta$  is highly sensitive to large and narrow extrema which could cause loss of electrical contact, and is thus more suitable for the given problem.

Figure 6.32:  $\delta$  versus  $I$  for  $w = 1$  mm and different  $d$ .

The starting point for the optimization was the investigation of the influence of  $I$  on  $\delta$ . First,  $I$  was varied for the geometric parameters of the base case. A parabola-like curve is found when plotting  $\delta$  versus  $I$ , and the optimum  $I$  equals the base case value of 1.88 (not by chance, see above). The black curve in Fig. 6.32 depicts this behavior.

Fig. 6.32 shows the dependency of  $\delta$  on  $I$  for a constant  $w$  of 1 mm and different  $d$ . There is always an optimum  $I$  for every set of geometric parameters. The curves for the larger distances have the same parabola-like shape, and they are shifted towards smaller  $\delta$  for smaller  $d$ . For the smaller distances, the lower ends of the parabolas seem to be cut off by almost horizontal lines. These lines are shifted towards larger  $\delta$  for smaller  $d$ . In the horizontal regimes, the mean current density of the auxiliary electrode does not influence its performance (with respect to the criterion  $\delta$ ).

Fig. 6.33 plots  $\delta$  versus  $I$  for a fixed  $d$  of 0.15 mm and different widths. A similar pattern is observed, only that the trends are mirrored on the horizontal axis. The parabola-like curves appear at larger  $w$  and are shifted towards smaller  $\delta$  for smaller  $w$ . The horizontal lines cut the parabolas at smaller  $w$  and are shifted towards larger  $\delta$  for smaller  $w$ .

The described behavior can be understood by investigating the current density of the governing extrema. This will be exercised for a constant  $w$  and different  $d$  (Fig. 6.32). The governing extrema are maxima

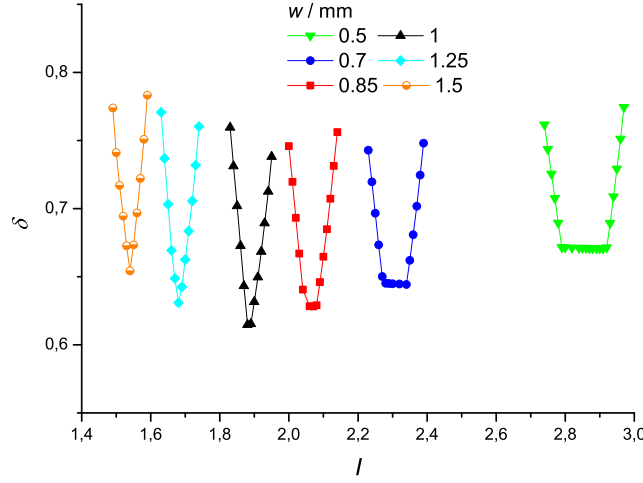


Figure 6.33:  $\delta$  versus  $I$  for  $d = 0.15$  mm and different  $w$ .

and minima of current density which become global extrema under particular conditions. In Fig. 6.31, the governing extrema of the PCB for the parameters in Fig. 6.32 are marked and named. Maximum 1 and minimum 2 stem from the geometry of the working electrode and could also be found on a continuous square-shaped workpiece without an auxiliary electrode. Maximum 2 is caused by introducing the auxiliary electrode. Without the latter, the current density rises from the middle of the edge to the corner. The auxiliary electrode reduces the current density at the corner more effectively than on the edge, because the corner has a larger auxiliary electrode area in its proximity. The superposition of both effects results in maximum 2. Maximum 3 and minimum 1 are caused by the active area density: The former is located on a raster element having the smallest active area density of 0.542 and the latter on a raster element having the largest active area density of 1. Fig. 6.31 only shows maximum 1–3 and minimum 1 in one corner of the working electrode; due to the symmetry<sup>1</sup> corresponding extrema exist in the other three corners.

Fig. 6.34 shows the normalized current density of these governing extrema for  $w = 1$  mm and  $d = 0.2$  mm. Three extrema are located close to the brink: maximum 1, maximum 2 and minimum 1. Their current density is reduced with increasing  $I$ . An increasing  $I$  results in general

<sup>1</sup>The PCB design has a four-fold rotation axis at its center.

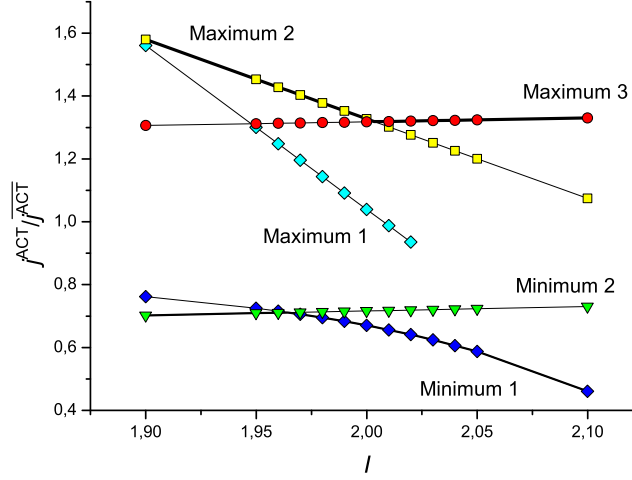


Figure 6.34: Normalized current density of the governing extrema versus  $I$  for  $w = 1$  mm and  $d = 0.2$  mm. Bold lines: global maximum and global minimum curve.

in a decreasing current density at the brink. This is exactly what the auxiliary electrode is meant to bring about: It lowers the current density at the brink of the workpiece.  $I$  may in fact be taken as a measure for the efficacy of the auxiliary electrode. Maximum 3 and minimum 2, on the contrary, receive slightly more current density with increasing  $I$ . This is because the mean current density of the workpiece is constant, and if the brink receives less current density, the center needs to receive accordingly more current density. This increase is less pronounced than the decrease at the brink, because the latter has a smaller area.

From this, it can be concluded that maximum 3 is already too far away from the auxiliary electrode to be affected by the current density suppression. In other words, only maximum 1, maximum 2 and minimum 1 are in the sphere of action of the auxiliary electrode.

The global extrema are indicated in Fig. 6.34 by the bold lines. They change position depending on  $I$ . The criterion  $\delta$  is proportional to the vertical difference of the global maximum and the global minimum, and the optimum  $\delta$  is proportional to the minimum vertical distance. The latter is found where the global maximum changes position from maximum 2 to maximum 3.

The same analysis is performed in Fig. 6.35 for  $w = 1$  mm and  $d = 0.15$  mm. The qualitative behavior of the curves is similar, but the points where the global maximum and minimum change position are shifted

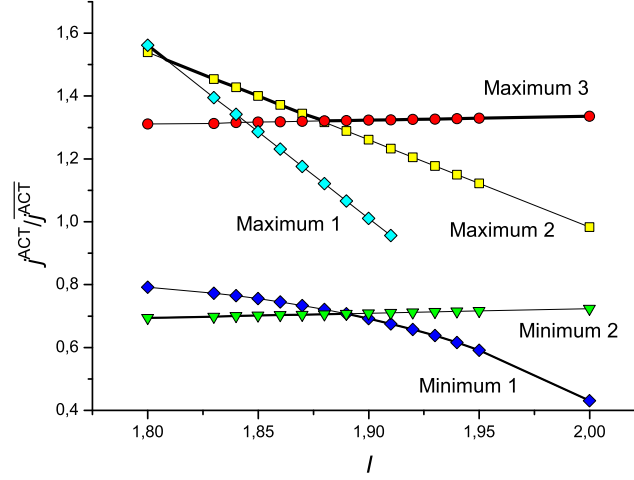


Figure 6.35: Normalized current density of the governing extrema versus  $I$  for  $w = 1$  mm and  $d = 0.15$  mm. Bold lines: global maximum and global minimum curve.

closer towards each other. This means that  $\delta$  reaches a smaller value than for  $w = 1$  mm and  $d = 0.2$  mm (see Fig. 6.32)

Fig. 6.36 plots the current density of the governing extrema for  $w = 1$  mm and  $d = 0.05$  mm. When going from  $d = 0.15$  mm to  $d = 0.05$  mm, the points where the global maximum and minimum change position are shifted away from each other.  $\delta$  is worse than for  $d = 0.15$  mm because maximum 3 and minimum 2 come into play: The optimum  $\delta$  is found in the region where these extrema are global. This is the region of the horizontal lines in Fig. 6.32. In these horizontal regimes, the criterion is governed by extrema which are outside the sphere of action of the auxiliary electrode.

The curves for maximum 2 and minimum 1 are shifted closer towards each other when decreasing  $d$ , i.e., when going from Fig. 6.34 to Fig. 6.35 and to Fig. 6.36. In contrast, the lines for maximum 3 and minimum 2 are shifted away from each other when decreasing  $d$ . This results in an optimum distance for a fixed width. This optimum distance is found exactly where the global maximum and the global minimum change position at the same  $I$ , which is the case for  $w = 1$  mm and  $d = 0.15$  mm (Fig. 6.35).

Fig. 6.37 presents the most condensed information in the optimization of the auxiliary electrode. The criterion  $\delta$  is plotted versus  $d$  for different  $w$ , and all data points are optimized with respect to  $I$ . Each minimum



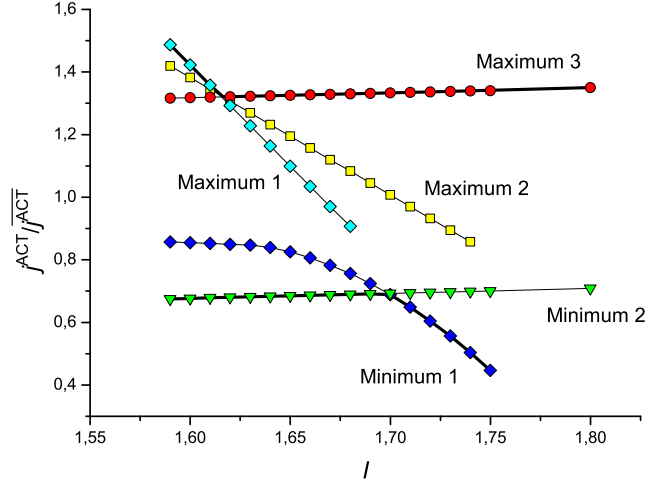


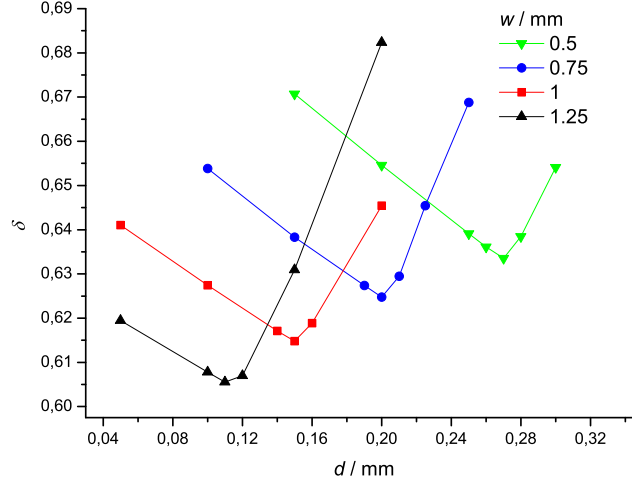
Figure 6.36: Normalized current density of the governing extrema versus  $I$  for  $w = 1$  mm and  $d = 0.05$  mm. Bold lines: global maximum and global minimum curve.

in Fig. 6.32 or 6.33 corresponds to one data point in Fig. 6.37. It is found that small  $d$  and large  $w$  are favorable in order to obtain a uniform current density distribution. This statement may be intuitive, but a false conclusion could be drawn from Figs. 6.32 and 6.33, where an optimum  $w$  and  $d$  exist. A wider auxiliary electrode can always achieve better uniformity, but  $d$  needs to be varied to obtain this finding. The same holds for  $d$ : An optimum exists only for a constant  $w$ . Smaller  $\delta$  are always possible for smaller distances, but a large  $w$  needs to be chosen to obtain them.

The base case auxiliary electrode was chosen to proceed with the modeling strategy, i.e., the mean current densities of the respective raster elements were evaluated from the macroscopic current density distribution with the base case auxiliary electrode.

### 6.2.2 Mesoscopic Modeling

As was mentioned in Sec. 6.1.1, normalized current density distributions do not depend on the mean current density if the charge-transfer resistance is constant, which is the case here. The mesoscopic simulations in this chapter only differ from the simulations without an auxiliary electrode in the mean current density. As a consequence, the mesoscopic current density distributions considering an auxiliary electrode can be

Figure 6.37:  $\delta$  versus  $d$  for different  $w$  and optimum  $I$ .

computed from the mesoscopic distributions not considering an auxiliary electrode. The latter only need to be multiplied with the factor  $f$ , which is defined as the fraction of the mean current densities of the mesoscopic reactors:

$$j(x, y, z)^{\text{AE}} = f j(x, y, z)^{\text{AE}}, \quad (6.3)$$

$$f := \frac{\overline{j^{\text{AE}}}}{\overline{j^{\text{AE}}}}. \quad (6.4)$$

$j(x, y, z)^{\text{AE}}$  is the mesoscopic current density distribution with and  $j(x, y, z)^{\text{AE}}$  the distribution without consideration of an auxiliary electrode.  $\overline{j^{\text{AE}}}$  stands for the mean current density of  $j(x, y, z)^{\text{AE}}$ , and  $\overline{j^{\text{AE}}}$  for the mean current density of  $j(x, y, z)^{\text{AE}}$ . They are determined from the respective macroscopic current density distributions. Eq. 6.3 holds if the distributions are normalized or not.  $f$  is 0.5130 for the raster element A2, 0.9283 for B2, 1.1327 for B6, 1.4395 for D9 and 1.5183 for F10. If the contour labels and the maximum and minimum current densities of the respective distributions (among those, Figs. 6.13, 6.22 and 6.23 contain the three chosen trenches) are multiplied by this value, one obtains the current density distributions with consideration of an auxiliary electrode.

### 6.2.3 Microscopic Modeling

What was discussed in Sec. 6.2.2 about normalized current density distributions does not concern the microscopic step, although the microscopic simulations as well only differ in the mean current density of the reactor. This is because the metal wall profiles must be computed for different points in time. The microscopic simulations thus cannot be determined from the microscopic simulations not considering an auxiliary electrode.

The microscopic modeling step is performed as in Sec. 6.1.3, only that different initial mean current densities are applied. They are evaluated from the mesoscopic current density distributions in Sec. 6.2.2. The shape evolution of the same three trenches is modeled. Their mean initial current densities are 1.377 times the mean  $j^{\text{ACT}}$  of the macroscopic distributions for trench 1, 1.295 for trench 2 and 1.222 for trench 3.

The results of the microscopic simulations are depicted in Fig. 6.38, which is structured just as Fig. 6.28. The shape evolution is significantly more uniform when using the auxiliary electrode: The metal wall profiles of the three trenches evolve almost simultaneously. The electrolyte contacts the insulating support after 336 s in trench 1, after 357 s in trench 2 and after 378 s in trench 3. The simulation predicts that under these conditions the process will not suffer from loss of electrical contact due to a non-uniform machining rate.

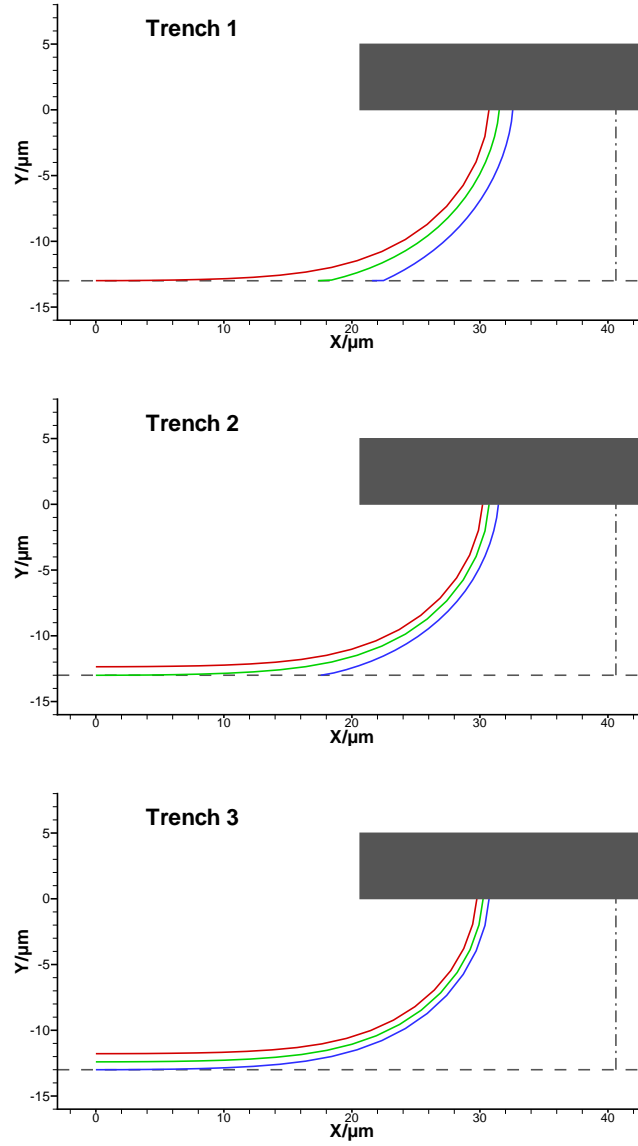


Figure 6.38: Microscopic shape evolution of trenches 1–3 for different points in time with the base case auxiliary electrode. Red line: etch profile at 336 s (insulating support exposed in trench 1); green line: etch profile at 357 s (insulating support exposed in trench 2); blue line: etch profile at 378 s (insulating support exposed in trench 3).

# Chapter 7

## Direct Simulation

This chapter is dedicated to the estimation of the accuracy of the modeling strategy. The macroscopic and the mesoscopic current density distributions computed in Chap. 6 will be evaluated using the direct simulation of the PCB as a benchmark. The determination of the accuracy will also lead to a quantitative evaluation of the frame's size in the mesoscopic modeling step.

The direct simulation is defined as the unsimplified modeling within the potential theory. This means application of the mathematical model outlined in Sec. 3.2 by using the boundary conditions Eqs. 3.9 and 3.10 for the entire reactor. This simulation yields the initial current density distribution over the real features of the entire workpiece in one step. As was discussed before, the direct simulation of a complex PCB is in general infeasible. It is possible here with constraints, because the PCB in question has a small width of 8.475 mm. PCBs encountered in industrial applications may have a width of centimeters or even larger, which renders the direct modeling infeasible.

The microscopic modeling step cannot be evaluated by these means. The direct three-dimensional moving-boundary simulation of the given PCB is infeasible with both the given software and hardware configuration, and thus remains as a future task.

The electrochemical parameters in the direct simulation are evidently identical to those used in Chap. 6. The direct simulation uses a reactor which resembles the reactor of the macroscopic modeling step, only that

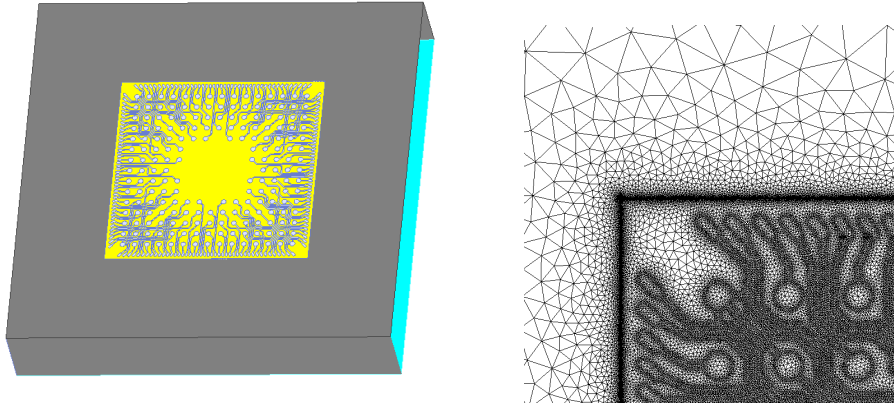
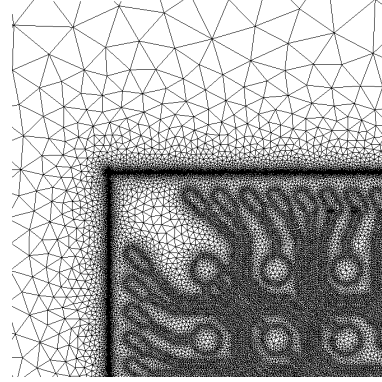


Figure 7.1: Reactor of the direct simulation. The working electrode is colored yellow, the counter electrode blue and insulating surfaces are either transparent or colored gray.



the active area density distribution is substituted with the real workpiece. Fig. 7.1 depicts the reactor of the direct simulation. The discretization of the reactor was made as fine as possible with the given hardware configuration and consisted of 2,135,813 nodes and 11,664,415 elements. A part of the surface mesh is shown in Fig. 7.2; it is the same section which is shown in Fig. 6.5. The computing time was 386 s.

Although the discretization is as fine as possible, it is not sufficient. This may not be apparent from Fig. 7.2, but it is when viewing the mesh on the mesoscopic scale. Fig. 7.3 shows the mesh at the lower left corner of raster element D9. The same section of the mesh in the mesoscopic modeling step is shown in Fig. 6.9. The comparison clearly shows how coarse the mesh in the direct simulation really is. In the mesoscopic modeling step, the strip of electrode area on the left is discretized with approximately 10 nodes in horizontal direction. In contrast, the mesh in the direct simulation has only 2–3 nodes there. It is evident that the current density distribution over the features is not reliable with this discretization. This problem will be addressed in Secs. 7.1 and 7.2, where the accuracy is quantified.

Fig. 7.4 depicts the normalized current density distribution of the direct simulation. The agreement of this distribution with the macroscopic distribution of the modeling strategy is not of interest here, because it only concerns the accuracy of the active area density approach. The latter has already been estimated by Mehdizadeh [30] and in several other studies (e.g., [35]). Furthermore, the modeling strategy does not use

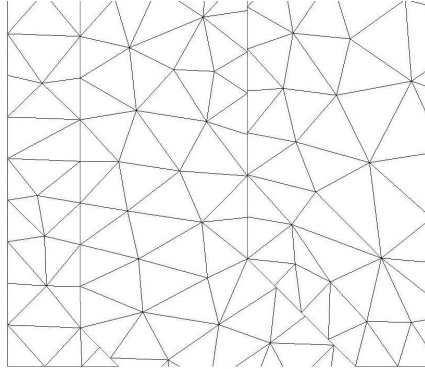


Figure 7.3: The surface mesh of the reactor in Fig. 7.1 at the lower left corner of raster element D9.

the distribution itself, but only mean current densities through raster elements.

The macroscopic modeling step does not consider the geometric factors of the features, which include the thickness of the photolithographic mask. If this thickness would be changed for the same PCB design, nothing would change in the macroscopic modeling step. The influence of the photoresist thickness on the accuracy of the modeling strategy is investigated with another direct simulation. It differs from the direct simulation performed before only in the thickness of the photolithographic mask, which is 40  $\mu\text{m}$ . Trenches now have an aspect ratio <sup>1</sup> of 1.01, compared to 0.12 with 5  $\mu\text{m}$  photoresist thickness.

The direct simulation with 40  $\mu\text{m}$  photoresist thickness is discretized with a comparably fine mesh as the simulation with 5  $\mu\text{m}$ . The mesh consisted of 1,819,995 nodes and 9,503,824 elements, and the computing time was 256 s. The computed current density distribution is depicted in Fig. 7.5.

## 7.1 Accuracy of the Macroscopic Modeling Step

The accuracy of the macroscopic modeling step is quantified by comparing the mean current densities through raster elements. In the modeling

---

<sup>1</sup>The aspect ratio of a trench is defined as its height divided by its width.

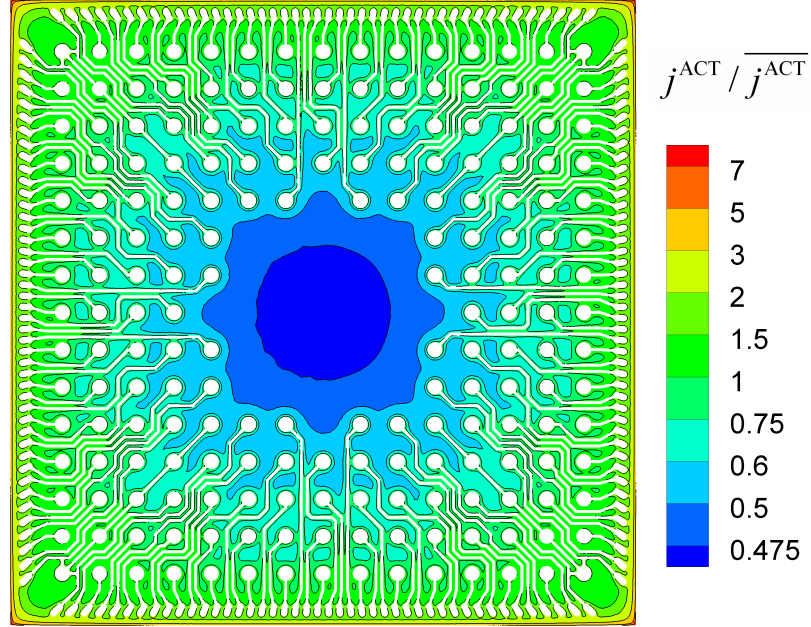


Figure 7.4: Normalized current density distribution of the direct simulation. Maximum 12.514, minimum 0.470.

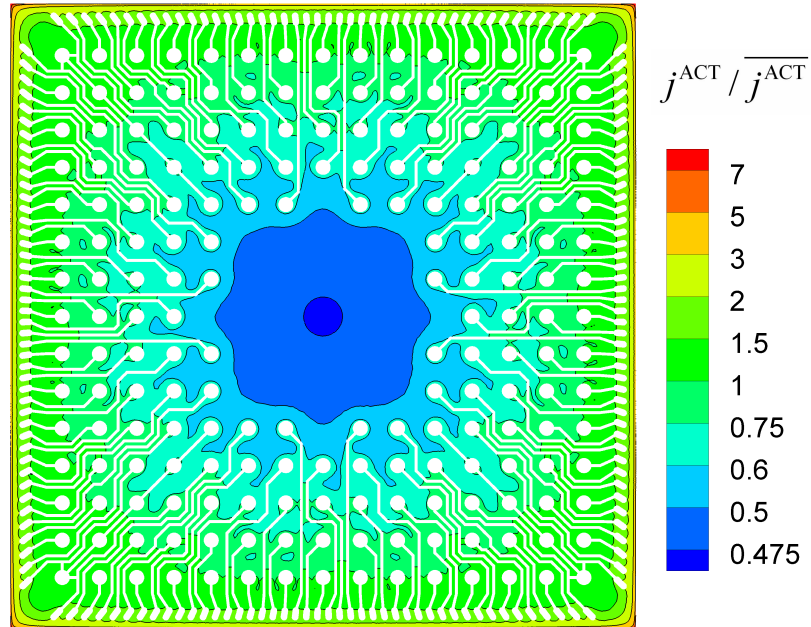


Figure 7.5: Normalized current density distribution of the direct simulation with 40  $\mu\text{m}$  photoresist thickness. Maximum 12.658, minimum 0.475.



strategy, these quantities are determined from the macroscopic distribution and used as input for the total current in the mesoscopic simulation. These mean current densities are the only macroscopic influences which enter the mesoscopic modeling step and hence, their agreement with the direct simulation corresponds with the accuracy of the macroscopic modeling step.

Because of the insufficient discretization in the direct simulation, the current density distribution on the features, i.e., on the microscopic and mesoscopic scale, is not reliable. However, the mean current densities of raster elements are much less sensitive to the discretization and may be considered reliable. The distributions in Figs. 7.4 and 7.5 were used to determine the mean current densities for the estimation of the accuracy.

Tab. 7.1 compares the currents through raster elements  $i$  from the modeling strategy and the direct simulation with 5  $\mu\text{m}$  and 40  $\mu\text{m}$  photoresist thickness.  $i$  is normalized to the total current of the working electrode. Currents are used instead of current densities to avoid ambiguity concerning  $j^{\text{ACT}}$  and  $j^{\text{SUP}}$ .  $\Delta$  is the deviation of the modeling strategy from the direct simulation, defined as

$$\Delta := \frac{i_{\text{strategy}} - i_{\text{direct}}}{i_{\text{direct}}}, \quad (7.1)$$

where  $i_{\text{strategy}}$  and  $i_{\text{direct}}$  are  $i$  through the respective raster element obtained from the modeling strategy and the direct simulation, respectively. It is negative, if  $i$  from the modeling strategy is too small with respect to the direct simulation, and positive, if it is too large. Because the workpiece has a four-fold rotation axis, it is sufficient to list a quarter of the raster elements.

	Strategy $i$	Direct 5 $\mu\text{m}$ $i$	$\Delta$	Direct 40 $\mu\text{m}$ $i$	$\Delta$
A1	11.260	11.316	−0.5%	11.514	−2.3%
A2	7.058	7.051	0.1%	7.025	0.5%
A3	6.410	6.373	0.6%	6.371	0.6%
A4	6.169	6.195	−0.4%	6.197	−0.4%
A5	5.999	6.024	−0.4%	6.018	−0.3%
A6	5.885	5.923	−0.6%	5.910	−0.4%
A7	5.859	5.976	−2.0%	5.962	−1.7%

	Strategy	Direct 5 $\mu\text{m}$		Direct 40 $\mu\text{m}$	
	$i$	$i$	$\Delta$	$i$	$\Delta$
A8	5.837	5.929	−1.6%	5.907	−1.2%
A9	5.726	5.638	1.6%	5.620	1.8%
A10	5.830	5.922	−1.6%	5.900	−1.2%
A11	5.866	5.974	−1.8%	5.954	−1.5%
A12	5.888	5.921	−0.5%	5.906	−0.3%
A13	6.002	6.022	−0.3%	6.015	−0.2%
A14	6.171	6.195	−0.4%	6.197	−0.4%
A15	6.411	6.376	0.6%	6.372	0.6%
A16	7.058	7.052	0.1%	7.024	0.5%
A17	11.258	11.317	−0.5%	11.518	−2.3%
B2	3.794	3.714	2.1%	3.643	4.0%
B3	3.325	3.306	0.6%	3.247	2.3%
B4	3.147	3.205	−1.0%	3.156	0.6%
B5	3.095	3.091	0.1%	3.065	1.0%
B6	3.104	3.074	1.1%	3.072	1.0%
B7	3.035	3.020	1.0%	3.032	0.7%
B8	3.039	2.942	3.3%	2.929	3.6%
B9	3.014	3.005	0.3%	2.990	0.8%
B10	2.996	3.003	−0.2%	3.007	−0.4%
B11	3.063	3.016	1.5%	3.025	1.2%
B12	3.105	3.073	1.0%	3.072	1.1%
B13	3.096	3.091	0.2%	3.065	1.0%
B14	3.175	3.204	−0.9%	3.156	0.6%
B15	3.324	3.306	0.6%	3.248	2.3%
B16	3.795	3.714	2.2%	3.644	4.0%
C3	2.867	2.895	−1.0%	2.844	0.8%
C4	2.752	2.744	0.3%	2.735	0.6%
C5	2.568	2.551	0.7%	2.507	2.4%
C6	2.578	2.585	−0.3%	2.554	0.9%
C7	2.592	2.551	1.6%	2.558	1.3%
C8	2.596	2.553	1.7%	2.553	1.7%
C9	2.544	2.552	−0.3%	2.544	0.0%
C10	2.565	2.563	0.1%	2.578	−0.5%
C11	2.599	2.548	2.0%	2.552	1.8%
C12	2.579	2.584	−0.2%	2.553	1.0%
C13	2.569	2.550	0.7%	2.507	2.4%

	Strategy	Direct 5 $\mu\text{m}$		Direct 40 $\mu\text{m}$	
	$i$	$i$	$\Delta$	$i$	$\Delta$
C14	2.751	2.743	0.3%	2.736	0.6%
C15	2.867	2.895	-1.0%	2.846	0.7%
D4	2.644	2.607	1.4%	2.653	-0.3%
D5	2.468	2.418	2.1%	2.420	1.9%
D6	2.409	2.479	-2.8%	2.466	-2.3%
D7	2.432	2.414	0.7%	2.446	-0.6%
D8	2.387	2.417	-1.2%	2.419	-1.4%
D9	2.395	2.421	-1.1%	2.452	-2.4%
D10	2.393	2.427	-1.4%	2.429	-1.5%
D11	2.434	2.413	0.9%	2.444	-0.4%
D12	2.409	2.479	-2.8%	2.465	-2.3%
D13	2.468	2.418	2.1%	2.421	1.9%
D14	2.643	2.607	1.4%	2.653	-0.4%
E5	2.454	2.439	0.6%	2.484	-1.3%
E6	2.315	2.264	2.2%	2.274	1.8%
E7	2.349	2.384	-1.5%	2.408	-2.5%
E8	2.267	2.226	1.8%	2.212	2.4%
E9	2.315	2.349	-1.5%	2.382	-2.9%
E10	2.266	2.218	2.2%	2.209	2.5%
E11	2.348	2.384	-1.5%	2.408	-2.5%
E12	2.314	2.264	2.2%	2.274	1.7%
E13	2.452	2.439	0.5%	2.485	-1.3%
F6	2.292	2.309	-0.7%	2.333	-1.8%
F7	2.258	2.222	1.6%	2.228	1.3%
F8	2.228	2.200	1.3%	2.198	1.3%
F9	2.310	2.350	-1.7%	2.410	-4.3%
F10	2.230	2.194	1.6%	2.192	1.7%
F11	2.257	2.222	1.6%	2.228	1.3%
F12	2.291	2.308	-0.8%	2.333	-1.9%
G7	2.288	2.306	-0.8%	2.352	-2.8%
G8	2.253	2.269	-0.7%	2.305	-2.3%
G9	2.237	2.255	-0.8%	2.287	-2.2%
G10	2.252	2.269	-0.8%	2.306	-2.4%
G11	2.287	2.306	-0.8%	2.352	-2.8%
H8	2.221	2.235	-0.6%	2.262	-1.8%
H9	2.215	2.228	-0.6%	2.254	-1.7%

	Strategy	Direct 5 $\mu\text{m}$		Direct 40 $\mu\text{m}$	
	$i$	$i$	$\Delta$	$i$	$\Delta$
H10	2.221	2.235	−0.7%	2.262	−1.9%
I9	2.210	2.221	−0.5%	2.246	−1.6%

Table 7.1: Currents through raster elements  $i$  for the macroscopic modeling step and the direct simulations with 5  $\mu\text{m}$  and 40  $\mu\text{m}$  photoresist thickness. Values are normalized to the total current through the workpiece and given units of  $10^{-3}$ .  $\Delta$  is the deviation of the macroscopic modeling step from the direct simulations.

The accuracy of the macroscopic modeling step is in the range of a few percent. Compared to the direct simulation with 5  $\mu\text{m}$ , the maximum  $\Delta$  is 3.3% and the minimum  $\Delta$  is −2.8%. For 40  $\mu\text{m}$  photoresist thickness,  $\Delta$  varies from 4% to −4.3%. The average absolute  $\Delta$  is 1.1% for 5  $\mu\text{m}$  and 1.5% for 40  $\mu\text{m}$ .

The accuracy is barely influenced by the thickness of the photolithographic mask, although the latter is not reflected in the active area density approach. The photoresist thickness does influence the current density distribution on the mesoscopic and microscopic scale, but its influence on the macroscopic mean current densities is minor. This subject is discussed in detail in App. A.

## 7.2 Accuracy of the Mesoscopic Modeling Step

Both the direct simulation and the mesoscopic step of the modeling strategy yield the initial current density distribution over the real features. Evaluating the accuracy of the mesoscopic step is done by directly comparing these distributions.

As outlined in the beginning of this chapter, the discretization in the direct simulation is not sufficiently fine. It was argued in Sec. 7.1, that the current density distribution on the features is thus not reliable but that the mean current densities of raster elements may be considered reliable. In this section, the distribution on the features is of interest, so the direct modeling presented up to now cannot be used. Another direct simulation is performed which has a finer mesh on the raster element in question and correspondingly a coarser mesh on the rest of the workpiece. Because

the area of the raster element is much smaller than the area of the entire workpiece, the coarsening of the mesh on the latter is not significant. The current density distribution on the raster element with the finer discretization may be considered reliable, because the normalized current density distribution on a mesoscopic region is only influenced by the distribution on the surrounding features (see Chap. 5). This influence is considered with good accuracy, because the mesh is not getting abruptly coarse across the border of the respective raster element. The distribution is not reliable on regions far away, which influence the raster element in question only by their mean current density. Mean current densities of insufficiently discretized regions have already been considered reliable in Sec. 7.1.

The following paragraphs discuss the quantities used for the determination of the accuracy. The normalized residual current density  $j_r$  is defined as

$$j_r := \frac{j_{\text{strategy}}^{\text{meso}} - \bar{j}_{\text{direct}}}{\bar{j}_{\text{direct}}}, \quad (7.2)$$

where  $j_{\text{strategy}}^{\text{meso}}$  and  $\bar{j}_{\text{direct}}$  are the current density at a given point obtained from the mesoscopic step of the modeling strategy and the direct simulation, respectively.  $\bar{j}_{\text{direct}}$  is the mean current density of the direct simulation.  $j_r$  gives the deviation of the initial current density distribution yielded by the modeling strategy from the one yielded by the direct simulation. Although dimensionless, it is a measure for the absolute error, because it is normalized to a quantity which is constant for the entire workpiece.  $j_r$  is positive, if  $j_{\text{strategy}}^{\text{meso}}$  is too large compared to the direct simulation, and negative, if it is too small.

The relative error  $r$  of the modeling strategy current density with respect to the direct simulation current density,

$$r := \frac{j_{\text{strategy}}^{\text{meso}} - j_{\text{direct}}}{j_{\text{direct}}}, \quad (7.3)$$

is simply computed by following the common definition of the relative error. In contrast to  $j_r$ , it is normalized to the current density at the respective point. Based on  $r$ , the criterion  $\Sigma$  for the agreement of the

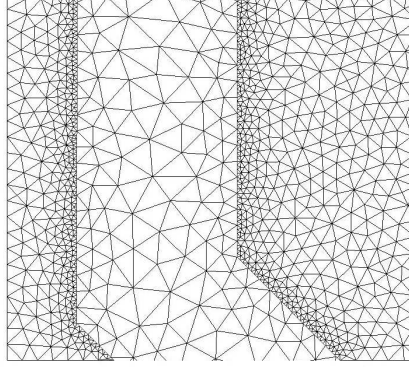


Figure 7.6: The surface mesh at the lower left corner of raster element D9 for the direct simulation with a finer discretization on this element.

modeling strategy with the direct modeling is defined as

$$\Sigma := \sqrt{\frac{1}{A} \iint_{\mathcal{W}} r^2 \, dx \, dy}. \quad (7.4)$$

$A$  is the norm of the integral, i.e., the area of the surface  $\mathcal{W}$  spanned by the limits of the integral.  $\mathcal{W}$  is the respective mesoscopic region, which is in general a raster element.  $\Sigma$  represents the mean root square of the relative error of the current density distribution obtained from the modeling strategy simulation. It is small for a good agreement of  $j_{\text{strategy}}^{\text{meso}}$  and  $j_{\text{direct}}$ , and large for a poor agreement.

App. B discusses numerical issues in the computation of the quantities  $j_r$ ,  $r$  and  $\Sigma$ .

### Raster Element D9

The direct simulation with a finer discretization on raster element D9 used a mesh with 2,255,198 nodes and 11,952,862 elements, and the computing time was 391 s. The mesh on the electrode surfaces of element D9 consisted of 22,672 nodes and 40,519 elements. Fig. 7.6 depicts the mesh at the lower left corner of raster element D9. It is not as fine as in the mesoscopic modeling step (see Fig. 6.9), but significantly finer than in the direct simulation presented before (see Fig. 7.3). These three figures all show the same workpiece section.

The macroscopic current density distribution is not pictured, because

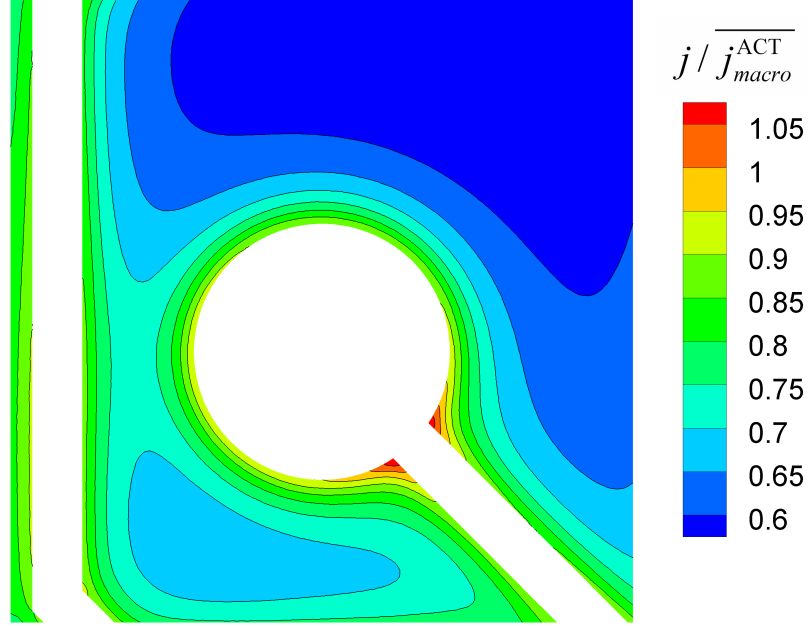


Figure 7.7: Mesoscopic current density distribution on raster element D9 from the direct simulation having a finer discretization there. The distribution is normalized to the mean current density. Maximum 1.094, minimum 0.552.

there is no visible difference compared to Fig. 7.4. The mesoscopic distribution on element D9 is shown in Fig. 7.7. A cross-section of this distribution is depicted in Fig. 6.12. Visual comparison with the mesoscopic modeling strategy simulation without frame (Fig. 6.10) and with frame 5 (Fig. 6.13) already shows that the accuracy is better with the frame; a quantitative discussion is given in what follows.

First, the distributions of  $j_r$  will be interpreted. They allow for a demonstrative discussion of the influence of the surrounding region's design, i.e., of the influence of the shapes and sizes of nearby features. Fig. 7.8 shows the  $j_r$  distribution for the modeling strategy simulation without a frame. The respective findings of Sec. 6.1.2 are confirmed by this plot: The current density distribution in the central region is relatively accurate, whereas there are large errors in the border region. The two erroneous maxima discussed in Sec. 6.1.2 are reflected as large (positive)  $j_r$ . The residuals are relatively large, varying from  $-14\%$  to  $+11\%$ .

Applying frame 2 in the modeling strategy simulation changes the  $j_r$  distribution a lot (see Fig. 6.11 for the size of all frames and the features they consider). Fig. 7.9 depicts this distribution. As was discussed in Sec.

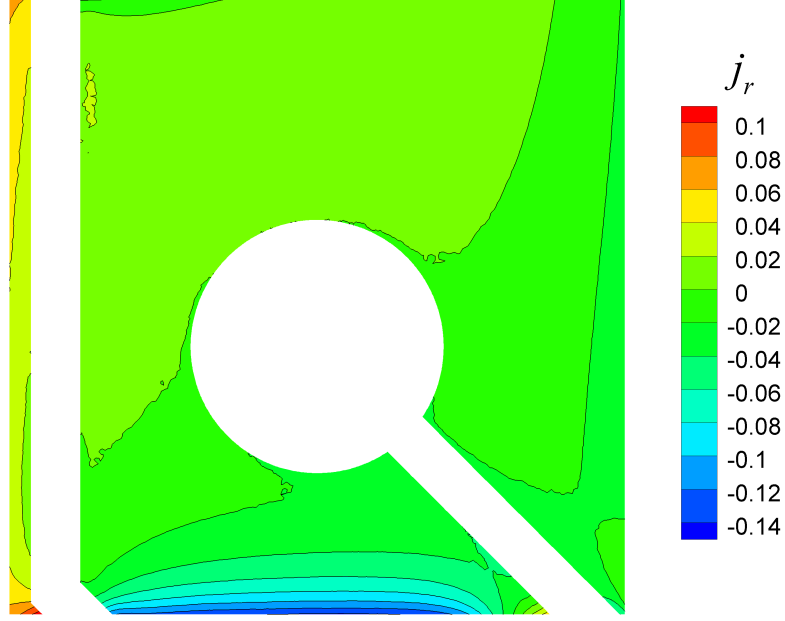


Figure 7.8:  $j_r$  distribution on raster element D9 without frame. Maximum 0.1072, minimum -0.1441.

6.1.2, the narrow strip of electrode surface receives less current density because of the additionally considered electrode area to the left of the raster element. This is reflected in the  $j_r$  distribution: The residuals are much smaller on that part of the raster element. Moreover, the lower border region receives much more current density with frame 1, which makes the absolute values of  $j_r$  smaller. This is because a part of the horizontal conducting line feature below the raster element (see Fig. 6.11) is taken into account. The central region of the raster element shows approximately the same absolute  $j_r$  without frame and with frame 1, which is around 0.01. This confirms that the distribution in the central region is almost unchanged by varying the frame size.

Fig. 7.10 shows the  $j_r$  distribution with frame 2. It has completely different characteristics: The contour lines are roughly vertical with the largest  $j_r$  at the left border and the smallest at the right border. This is because frame 2 considers conducting line feature 1 (see Fig. 6.11 for the naming of the conducting lines) which increases the current density on the left part of the raster element. The current density on the right part decreases accordingly, because the mean current density of the raster element is constant in all simulations.



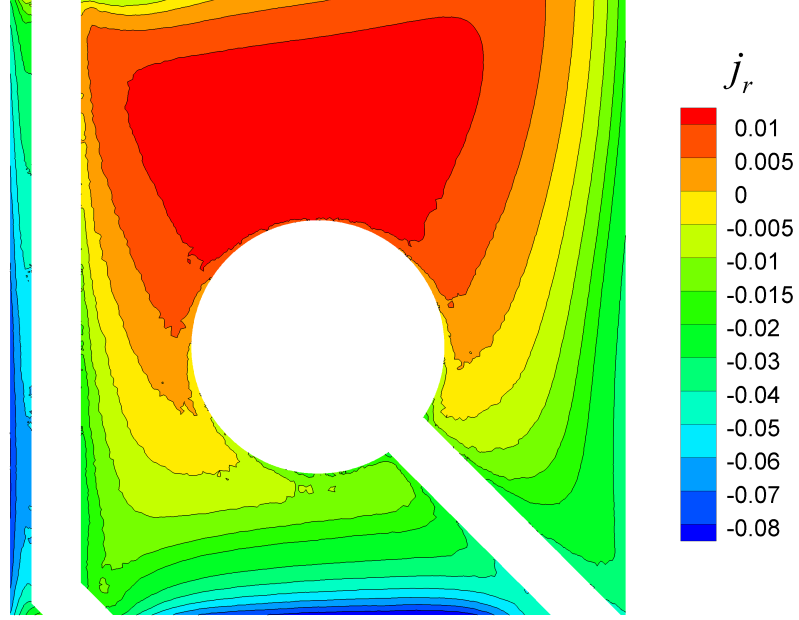


Figure 7.9:  $j_r$  distribution on raster element D9 with frame 1. Maximum 0.0146, minimum -0.0893.

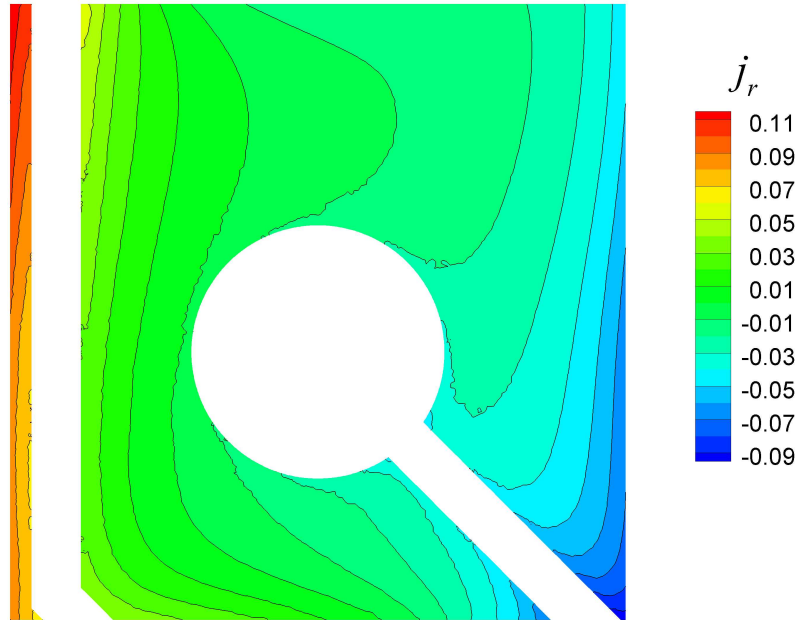


Figure 7.10:  $j_r$  distribution on raster element D9 with frame 2. Maximum 0.1206, minimum -0.0975.

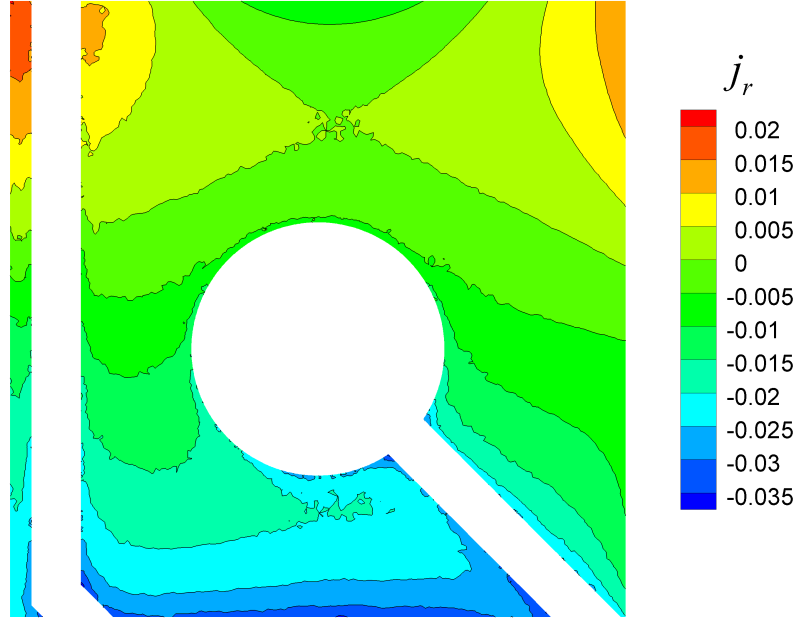


Figure 7.11:  $j_r$  distribution on raster element D9 with frame 3. Maximum 0.0203, minimum -0.0366.

The roughly vertical formation of the contour lines is not found in the residual distribution with the next largest frame, which is frame 3 (Fig. 7.11). This is due to taking into account conducting line feature 3, which is located to the right of the raster element. It levels the effect of conducting line feature 1, so that there is only small deviation on the horizontal axis. The main deviations are now found on the vertical axis.  $j_r$  is largest at the top and smallest at the bottom of the element.

This finding is even more pronounced in the distributions using frame 4 (Fig. 7.12) and frame 5 (Fig. 7.13). There is only negligible deviation on the horizontal axis, which means the contour lines are almost horizontal. Again, the residuals are largest at the top and smallest at the bottom. These deviations are obviously caused by an effect which cannot be taken into account by increasing the frame size.

The cause of this behavior can be understood by considering the position of the raster element on the workpiece (see Figs. 6.2 and 6.7). It is located in the horizontal middle of the workpiece. Because of the insulating surface enclosing the workpiece, the current density increases along the line running from the center of the workpiece to the middle of the (lower) edge. This line runs through raster element D9, so the

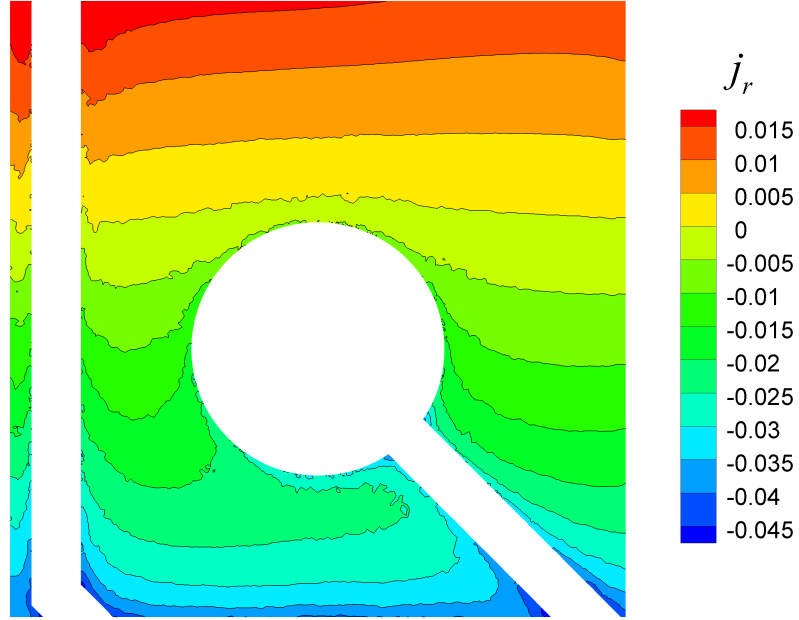


Figure 7.12:  $j_r$  distribution on raster element D9 with frame 4. Maximum 0.0208, minimum -0.0505.

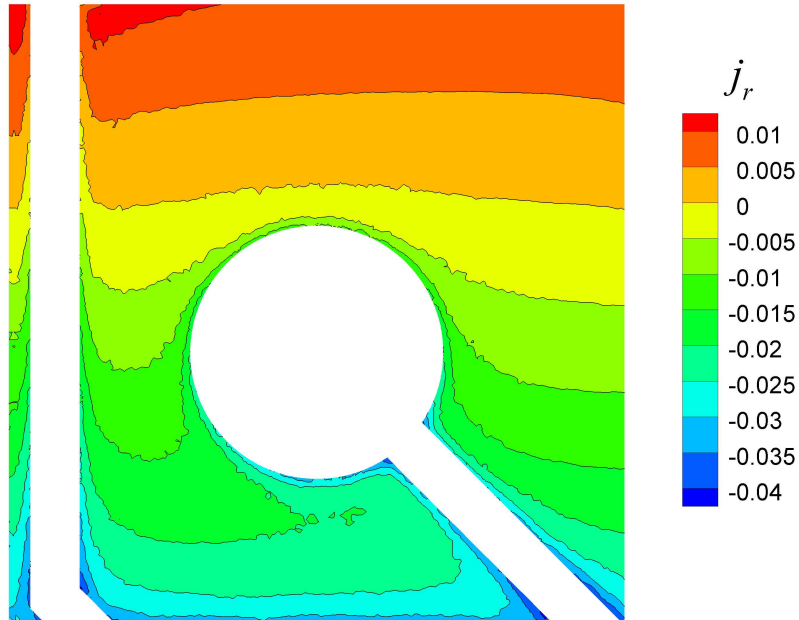


Figure 7.13:  $j_r$  distribution on raster element D9 with frame 5. Maximum 0.0133, minimum -0.0417.

current density also increases from the top to the bottom of the element. This *macroscopic* non-uniformity is not considered in the mesoscopic current density distribution, because the only macroscopic information entering the mesoscopic step is the mean current density of the respective raster element. It causes horizontal contour lines in the  $j_r$  plots for element D9. The deviations stemming from macroscopic non-uniformity are inherent in the modeling strategy. They are also contained in the distributions yielded without a frame and with the smaller frames but they are superposed there by mesoscopic non-uniformity. Macroscopic non-uniformity is only partly considered by the frames for raster elements located at the edge of the workpiece (see raster element A2).

The fact that only macroscopic non-uniformity remains as deviation from the direct simulation in Figs. 7.12 and 7.13 proves that the frame is a very effective tool in taking into account the influence of the mesoscopic surroundings. Mesoscopic non-uniformity can be considered as fully reflected in the modeling strategy.

The distributions of  $r$  show the same qualitative behavior as the distributions of  $j_r$ . Consequently, their interpretation leads to the same findings as discussed in the previous paragraphs. Figs. 7.14 and 7.15 picture the  $r$  distributions without frame and with frame 5. The only apparent difference to the  $j_r$  distributions is that the horizontal formation found with frame 5 is more pronounced in the  $r$  distribution. This is because the normalization to the mean current density in the computation of  $j_r$  causes the latter to be larger in regions with a large current density and smaller in regions with a small current density (if the relative error has the same order of magnitude). This slightly deforms the distributions of  $j_r$ .

A quantitative measure for the accuracy is the criterion  $\Sigma$ , which will now be discussed for the element D9. Fig. 7.16 plots  $\Sigma$  against the width of the frame normalized to the width of the raster element (a normalized frame width of 1 means no frame is used). It could be expected that  $\Sigma$  decreases monotonically with increasing frame size, but the run of the criterion is much more complicated.

The decrease in  $\Sigma$  from no frame to frame 1 is expected, but the accuracy gets worse when introducing frame 2.  $\Sigma$  is even larger than without a frame. This results from accounting for conducting line feature 1 and not accounting for conducting line feature 3. This effect is obviously

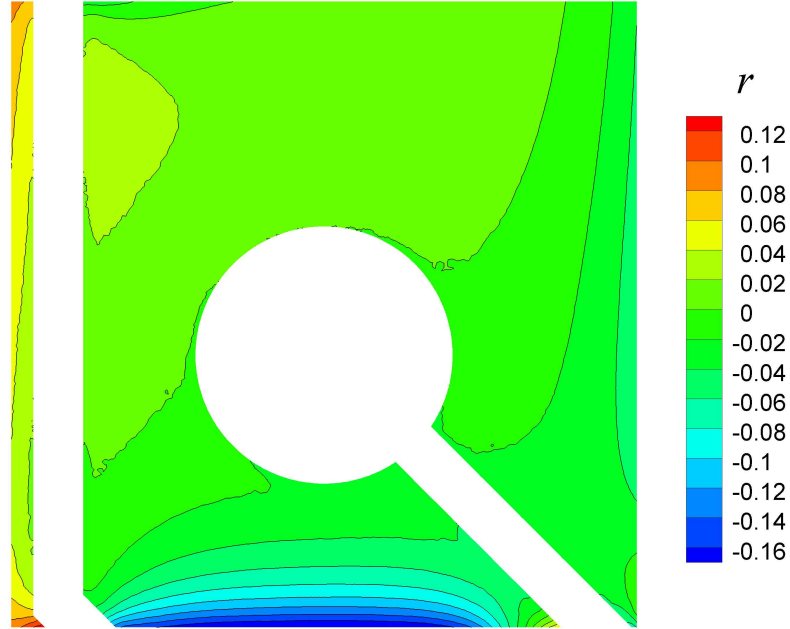


Figure 7.14:  $r$  distribution on raster element D9 without frame. Maximum 0.1278, minimum -0.1877.

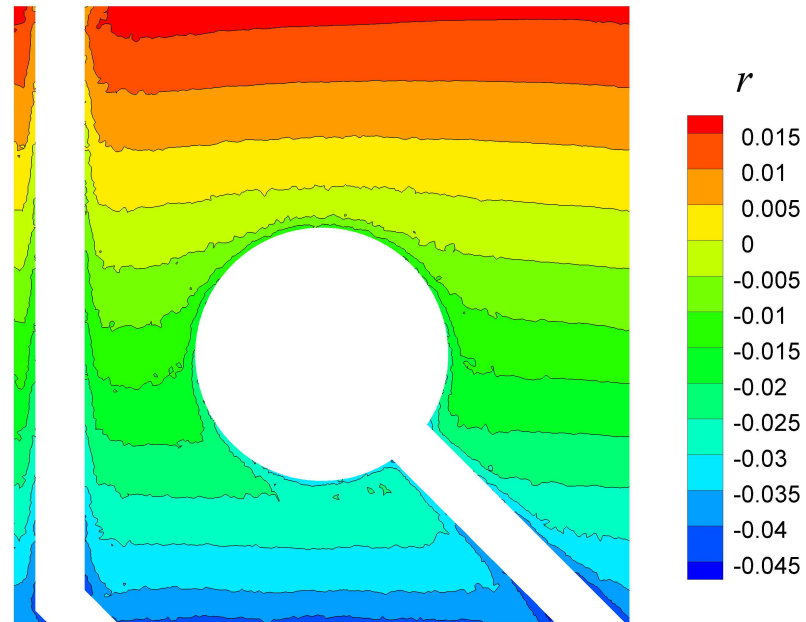


Figure 7.15:  $r$  distribution on raster element D9 with frame 5. Maximum 0.0177, minimum -0.0480.

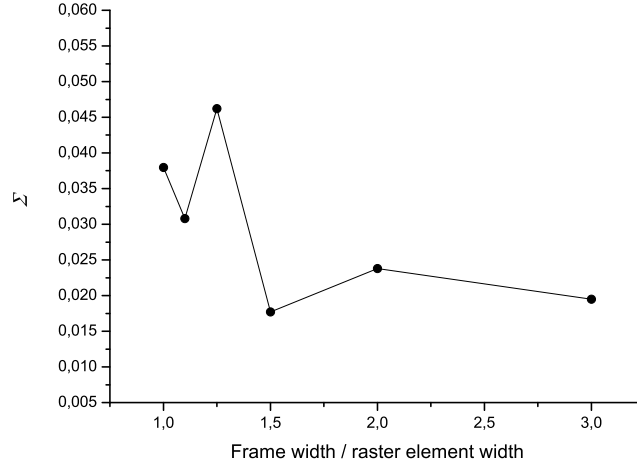


Figure 7.16:  $\Sigma$  versus width of the frame normalized to the width of the raster element for element D9.

pretty strong, which is also indicated by the  $j_r$  distribution with frame 2 (Fig. 7.10) having completely different characteristics than those with the other frames.

Using frame 3 yields the best accuracy of all frames, which is due to two reasons. Frame 3 takes into account both conducting line features 1 and 3, so there are no significant residuals on the horizontal axis. As was discussed before, macroscopic non-uniformity remains unconsidered for raster elements not located at the edges. Frame 3 accounts for the horizontal conducting line feature below the raster element. It increases the current density on the lower border region, thereby having the same effect as the macroscopic non-uniformity. Because the frame cuts off the electrode surface below this conducting line feature, its ohmic pathway is completely consumed by the current tubes above, which include the lower border region of the element. The resulting increase of the current density there counteracts coincidentally the deviation stemming from not considering macroscopic non-uniformity. Frame 2 also considers this conducting line feature, but the deviations on the horizontal axis surpass this effect.

Frame 4 and 5 achieve slightly worse accuracy than frame 3, because the coincidental counteraction of the macroscopic non-uniformity is weakened by taking into account electrode surfaces below the horizontal conducting line feature.

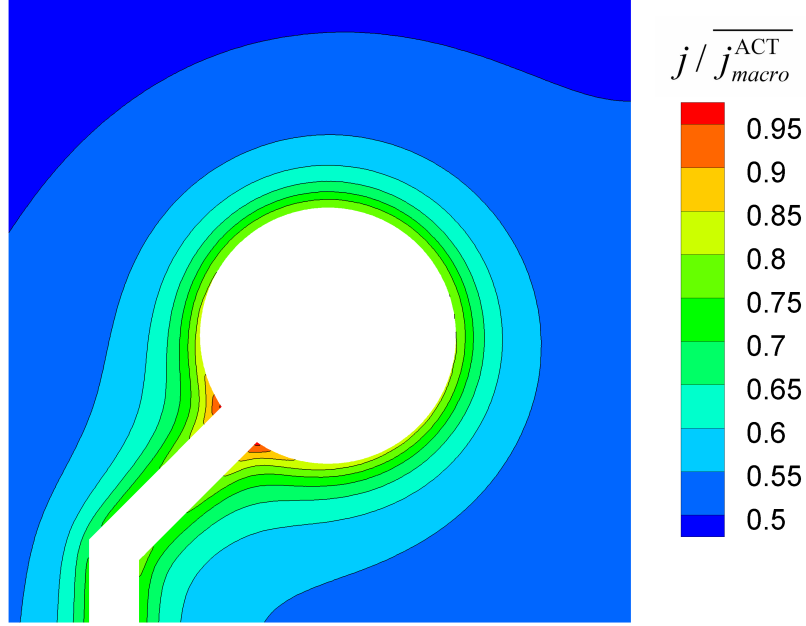


Figure 7.17: Mesoscopic current density distribution on raster element F10 from the direct simulation having a finer discretization there. The distribution is normalized to the mean current density. Maximum 0.960, minimum 0.485.

### Raster Element F10

The direct simulation with a finer discretization on raster element F10 used a mesh with 2,181,337 nodes and 11,922,106 elements. 20,205 nodes and 38,730 elements were used on the element F10, and the computing time was 936 s. The current density distribution on the element in question is depicted in Fig. 7.17. A cross-section of this distribution is shown in Fig. 6.15. There is no apparent deviation from the mesoscopic modeling strategy current density distribution with frame 5 (Fig. 6.17), and the deviation from the distribution without a frame (Fig. 6.16) is minor. The reasons why the introduction of a frame has only minor influence on the distribution have been discussed in Sec. 6.1.2.

Fig. 7.18 shows the distribution of  $j_r$  without using a frame. The largest residuals of about 3% are found in the lower left part. This is much less than the residuals found for raster element D9 without using a frame (Fig. 7.8). However, it is more than the residuals identified with macroscopic non-uniformity (Fig. 7.13) and is thus supposed to stem from mesoscopic effects. In fact, they can be attributed to not considering

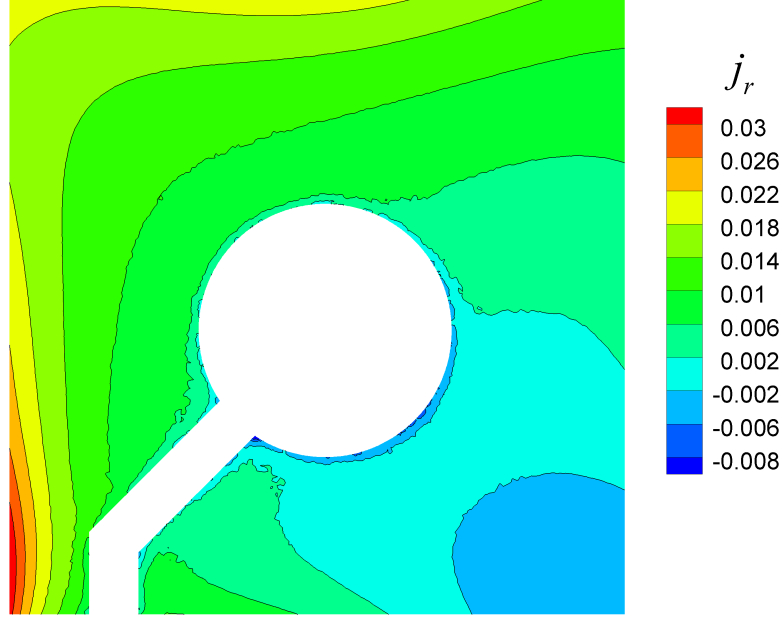


Figure 7.18:  $j_r$  distribution on raster element F10 without frame. Maximum 0.0336, minimum -0.0096.

the electrode surface to the left of the element. It consumes some of the ohmic pathway provided by the conducting line feature, which is received by the lower left part of the element if no frame is used. Thus, the current density is too large in the modeling strategy simulation. This effect is largest at the lower left border, because it is closest to the conducting line feature.

The  $j_r$  distribution with frame 3 (Fig. 7.19) does not show this effect any more. Considering the location of the raster element on the workpiece, the contour lines seem to have a too large slope to identify this distribution solely with macroscopic non-uniformity. They should only have a small positive slope.

Using frame 5 (Fig. 7.20) yields the behavior expected for macroscopic non-uniformity. This means the features outside of frame 3 still have some effect on the current density distribution, which revises the finding in Sec. 6.1.2 that they do not. The range of the remaining residuals is somewhat smaller than the one found for raster element D9. This was expected, because macroscopic non-uniformity will in general be more pronounced the closer the raster element is to the edge of the workpiece



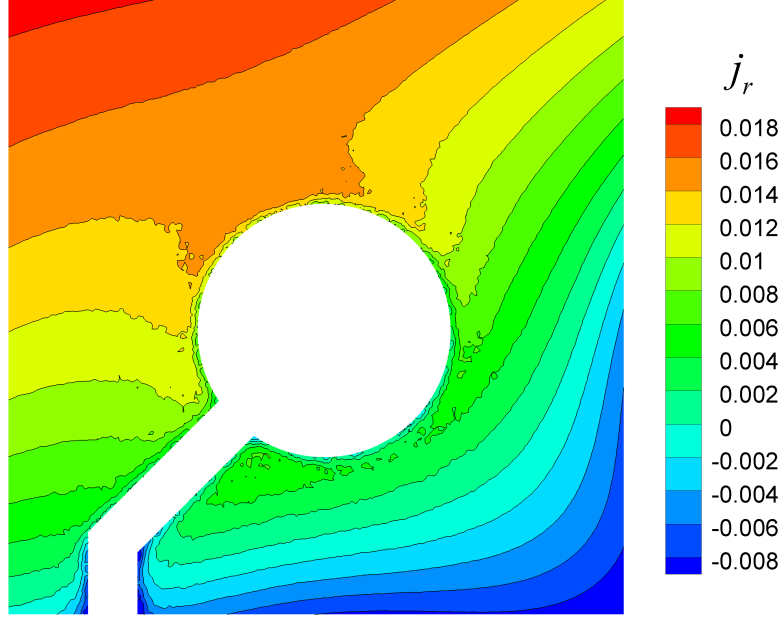


Figure 7.19:  $j_r$  distribution on raster element F10 with frame 3. Maximum 0.0187, minimum -0.0140.

(because maxima of current density occur in general at corners and edges, respectively). The improvement that could be achieved with introducing a frame is much smaller than for element D9, which was already discussed and reasoned in Sec. 6.1.2.

The criterion for the accuracy  $\Sigma$  is plotted against the frame width in Fig. 7.21. There is almost no change in  $\Sigma$  until frame 4 is applied. This is because the only surrounding features apart from the conducting line feature protruding from the element are located outside frame 3. In contrast to what was found from the cross-sections of the current density distributions in Sec. 6.1.2, plotting  $\Sigma$  shows that they do have an influence on the accuracy. For the smaller frames, the protruding conducting line feature causes residuals in the lower left corner. This is not reflected in Fig. 7.21 because these residuals are not widespread enough to have a significant effect on  $\Sigma$ . The improvement from frame 4 to frame 5 is minor.  $\Sigma$  starts at 1.98% without a frame and ends with 1.51% with frame 5, so the improvement in the criterion is only about 0.5%. For raster element D9, this improvement is about 1.9%. The value of  $\Sigma$  obtained with frame 5 is 1.51% for F10 and 1.95% for D9. This reflects that the macroscopic non-uniformity in element F10 is less pronounced than in D9.

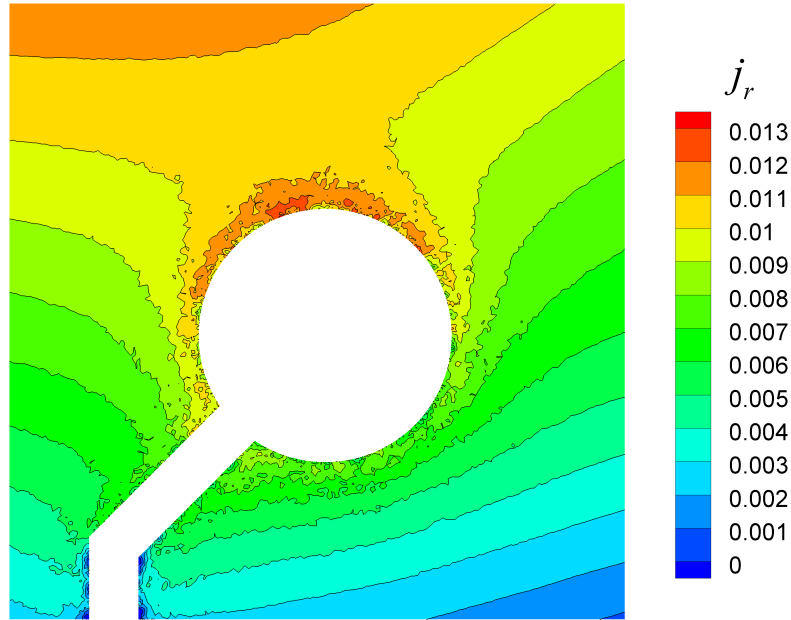


Figure 7.20:  $j_r$  distribution on raster element F10 with frame 5. Maximum 0.0142, minimum -0.0028.

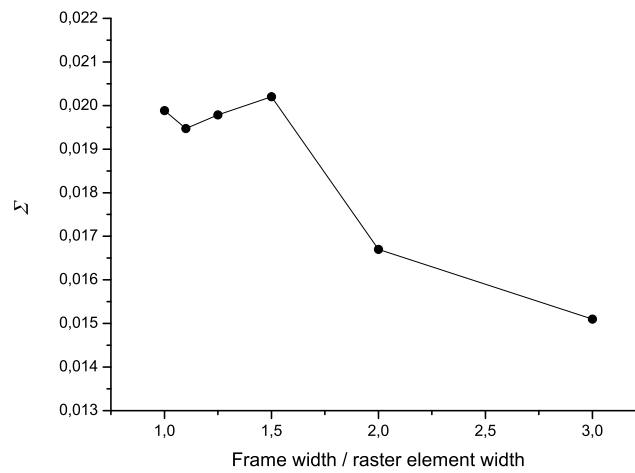


Figure 7.21:  $\Sigma$  versus width of the frame normalized to the width of the raster element for element F10.

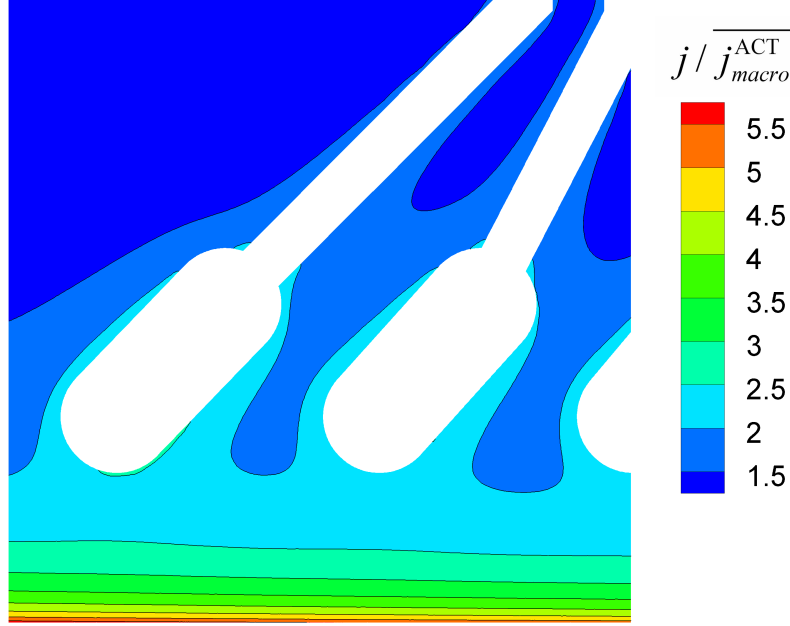


Figure 7.22: Mesoscopic current density distribution on raster element A2 from the direct simulation having a finer discretization there. The distribution is normalized to the mean current density. Maximum 5.911, minimum 1.090.

### Raster Element A2

The direct simulation with a finer discretization on raster element A2 used a mesh consisting of 2,082,064 nodes and 11,365,365 elements, of which 29,817 nodes and 56,082 elements were used for the element A2. The computing time was 537 s. The current density distribution on raster element A2 is pictured in Fig. 7.22, and a cross-section is depicted in Fig. 6.19. The distribution has the same characteristics as the modeling strategy distribution with frame 5 (Fig. 6.21), but the non-uniformity is somewhat more pronounced.

Raster element A2 is located at the edge of the workpiece. As was discussed qualitatively in Sec. 6.1.2, the insulating reactor wall enclosing the workpiece plays a dominant role and superposes the (mesoscopic) influence of the surrounding features. This reactor wall causes *macroscopic* non-uniformity, and it is partly taken into account by the frames. Thus, the introduction of the frames can partly reflect macroscopic non-uniformity here. This is in contrast to the elements D9 and F10, where it remained completely unconsidered. Macroscopic non-uniformity is ex-

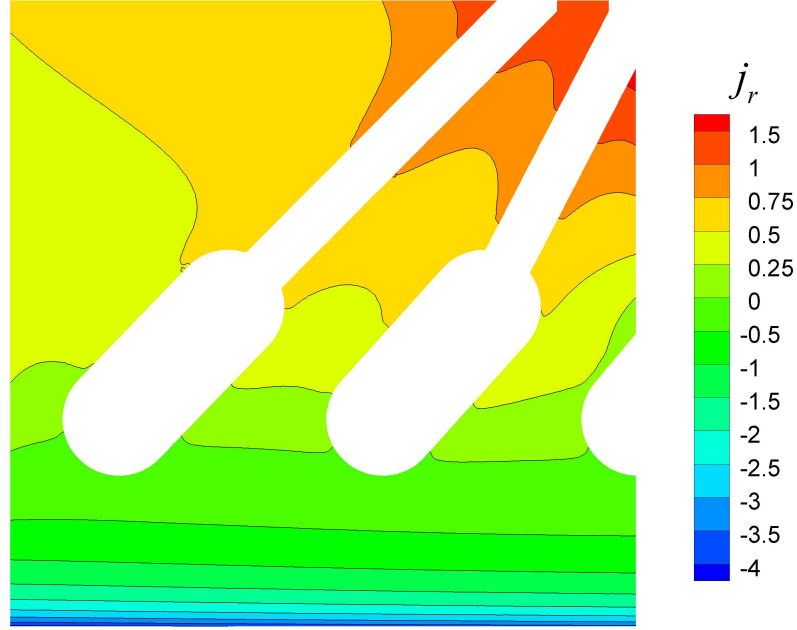


Figure 7.23:  $j_r$  distribution on raster element A2 without frame. Maximum 1.770, minimum -4.229.

pected to be much more pronounced for this element, because it is located at the edge.

The distribution of  $j_r$  without a frame, depicted in Fig. 7.23, shows nearly horizontal contour lines in the lower region. For element D9, horizontal contour lines were identified with macroscopic non-uniformity. This does not hold here, because the element A2 is not located in the middle of the horizontal axis. According to its location, the contour lines for this element are supposed to be sloped up to  $45^\circ$  and to have an increasing slope from the right to the left border. There is obviously a mesoscopic effect making the contour lines horizontal.

This horizontal behavior fades with increasing frame size. The  $j_r$  distribution with frame 2 (Fig. 7.24) shows sloped contour lines, and even more the distribution with frame 5 (Fig. 7.25). The  $j_r$  distributions with frame 1, 3 and 4 are intermediate steps between the three pictured distribution. The characteristics of the  $j_r$  distribution with frame 5 are identified with macroscopic non-uniformity. The quantitative error caused by the latter is expected to be smaller with increasing frame size, as indicated by the range of the residuals in Figs. 7.23, 7.24 and 7.25.

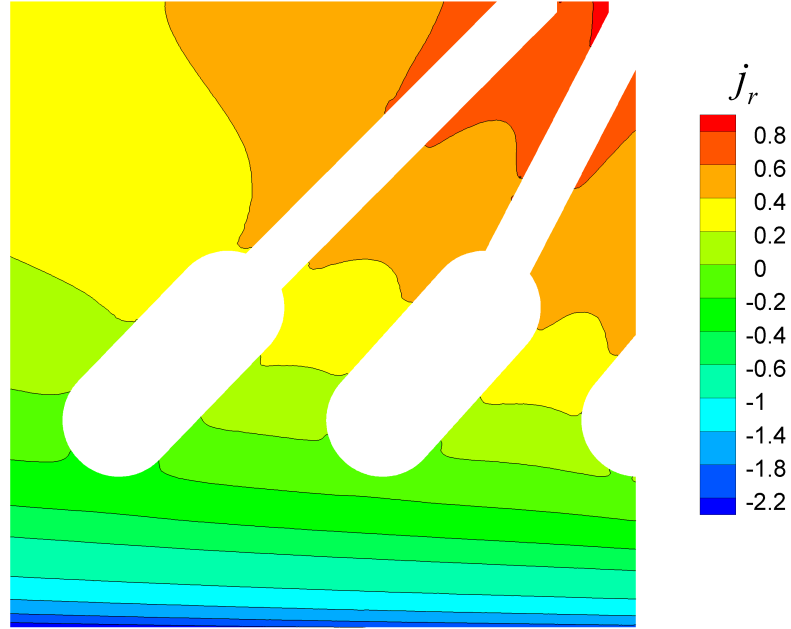


Figure 7.24:  $j_r$  distribution on raster element A2 with frame 2. Maximum 0.846, minimum -2.600.

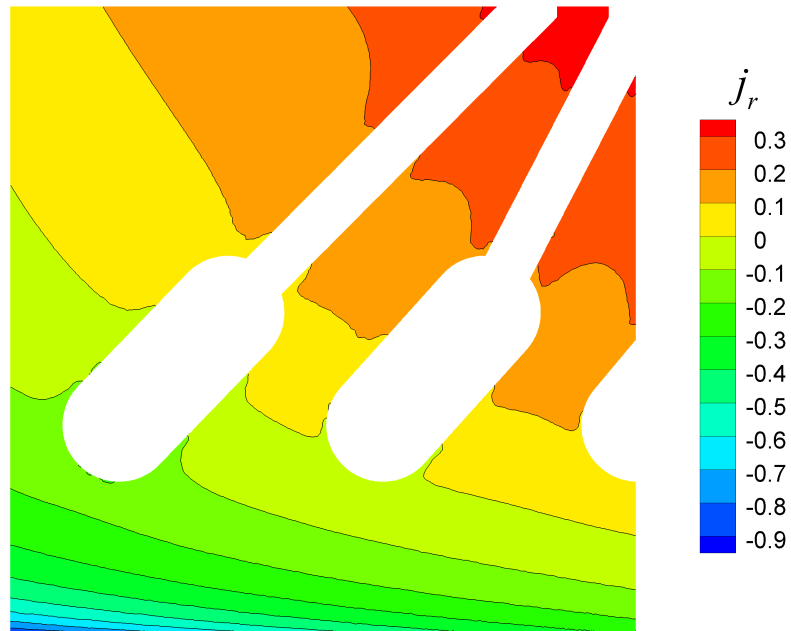


Figure 7.25:  $j_r$  distribution on raster element A2 with frame 5. Maximum 0.358, minimum -0.926.

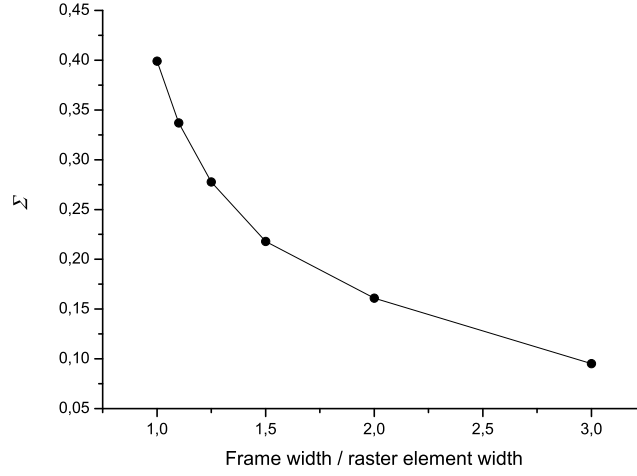


Figure 7.26:  $\Sigma$  versus width of the frame normalized to the width of the raster element for element A2.

The horizontal contour lines in the distribution without a frame are caused by not considering the electrode surface of raster element A1 (see Fig. 6.18). The consideration of the latter, which is done by increasing the frame size, decreases the current density in the left part of the element in question, which is reflected by the sloping of the contour lines. Obviously, not taking into account this electrode surface has coincidentally made the contour lines nearly horizontal in Fig. 7.23.

Fig. 7.26 plots  $\Sigma$  against the normalized width of the frame for raster element A2. The criterion is much larger than for the two raster elements discussed before; it ranges from 39.91% without a frame to 9.51% with frame 5. This is because the macroscopic non-uniformity is the more pronounced the closer a raster element is located to the edge and corner, respectively.  $\Sigma$  approaches a limiting value, which could only be reached if the frame accounts for the total reactor wall enclosing the workpiece. In that case, the modeling strategy simulation would as costly as the direct simulation. The improvement of  $\Sigma$  is much larger than for the elements D9 and F10. This is due to the partly consideration of macroscopic non-uniformity, which causes a much larger error than mesoscopic non-uniformity.

### 7.2.1 Choosing an Appropriate Frame Size

In Sec. 6.1.2, the question of which frame size is sufficient in the mesoscopic step of the modeling strategy has been discussed qualitatively on the basis of cross-sections of the current density distributions (Figs. 6.12, 6.15 and 6.19). In Sec. 7.2, this matter has been interpreted with quantitative parameters.  $j_r$  allows for a demonstrative interpretation of the mesoscopic and macroscopic non-uniformity and how they are reflected in the current density distributions.  $\Sigma$  represents the overall error of the distribution in one number, and is thus the appropriate quantity to conclude a recipe for choosing an appropriate frame size.

For raster elements not located at the edges, the frame accounts only for *mesoscopic* non-uniformity. In this case, it is difficult to predict which frame size will yield good accuracy. Depending on the design of the surrounding features, the error may even increase with increasing frame size. Frame 3, which has a width of 1.5 times the width of the raster element, has shown to yield satisfying accuracy for the investigated raster elements. It is suggested as a standard frame size for satisfying accuracy. If mesoscopic computations may be more costly than with frame 3, the use of frame 5 is suggested, because it shows somewhat better accuracy. It has a width of three times the raster element. It is emphasized that a very small frame or even no frame may yield satisfying accuracy. Consideration of the design of the surrounding features helps in pre-estimating the frame size. Fewer features in the surroundings and a larger distance of them from the raster element favor a smaller frame size. If conducting line features cross the raster element border perpendicularly, they do not cause any error. Conducting line features not crossing the border perpendicularly cause an error, as well as any other non-symmetric features which are partly cut off.

For raster elements which are located at the edges of the workpiece, introducing a frame reflects *mesoscopic* and *macroscopic* non-uniformity. The latter is much more pronounced at the edges and thus dominates the accuracy. The frame size should be as large as possible; frame 5 is given as a standard suggestion. The improvement of the accuracy while enlarging the frame to this size is large. The error decreases strictly monotonic, so a larger frame will always yield better accuracy than a smaller one.





# Chapter 8

## Future Work / Outlook

In the work presented here, only the shape evolution of trenches is investigated. This is dictated by the use of a two-dimensional moving-boundary software. Applying three-dimensional moving-boundary simulations would certainly improve the information value of the modeling strategy. The shape evolution of any desired feature or any desired combination of features could be investigated. Furthermore, the exact point in time when the electrical contact is lost could be determined. The shape of the machined metal layer at this point would be of great interest for the characterization of the machining process.

The overall performance of through-mask EMM processes may significantly be influenced by different sizes of the mask openings (e.g., different trench widths, pad opening or trench opening ...). The features of the PCB design discussed in this thesis all have the same characteristic dimensions. Furthermore, only the shape evolution of trenches was discussed. The difference between, e.g., the trench and the pad openings was not investigated. The investigation of equally wide trenches allows for a discussion of the non-uniformity of the shape evolution due to the electrochemical nature of the process. The influence of the location on the workpiece is clearly reflected. The effect of different mask opening sizes is at first best investigated on the microscopic scale, because it is then separated from the effect of the location. This has already been reported in literature [38, 40]. Investigating PCB designs with features having different characteristic dimensions would mix the effect of the location with the effect of different mask opening sizes. This might be an interesting

problem in future research on the through-mask EMM of PCBs.

The modeling strategy presented here does not consider concentration overpotential. It is based completely on the potential model, which accounts for migration but not for diffusion and convection. This does not allow for instance the discussion of surface films occurring at high current densities [13, 14, 15]. These films are known to have an essential influence on the machining process. Therefore, a consideration of concentration overpotential would strengthen the modeling strategy's importance a lot. The three-dimensional macroscopic modeling of PCBs on the basis of Eq. 3.3 is at the moment infeasible concerning both software and hardware. However, it is feasible on the microscopic scale. Mixing the potential model on the macroscopic scale with a model based on Eq. 3.3 on the microscopic scale could be a path towards the consideration of concentration overpotential in the modeling strategy. This is supposed to be a tenuous task, and justifications would have to be argued. A modification of the active area density approach including a simplified consideration of concentration overpotential has been published [30]. This could be a starting point for building the modeling strategy completely on tertiary current density distributions.

The strategy has been developed for through-mask electrochemical micromachining but it could also be applied to through-mask electrodeposition. If the same PCB design would be fabricated with through-mask electrodeposition, the photolithographic mask would – simply spoken – be the negative pattern of the photoresist in electrolytic etching. Concerning both the mathematical model and the strategy, the treatment of deposition would presumably be straightforward. The weak point in the application to through-mask electrodeposition on PCBs would be the occurrence of small active area densities. The PCB design dealt with in this thesis has an average active area density of 0.732 in etching, which corresponds to less than 0.268 in deposition. In general, the accuracy of the mean current densities determined from current density distributions is less sensitive to small active area densities than the distributions themselves. A quantification of how low the active area density may become while still yielding satisfying accuracy was not of interest in this thesis because the occurring active area densities were relatively large. It would surely be necessary in the application of the strategy to through-mask electrodeposition on PCBs.

# Chapter 9

## Conclusions

This thesis introduces a modeling strategy for the prediction of the shape evolution of complex photolithographically patterned electrodes, such as PCBs. The PCB used here has features with characteristic dimensions of tens of micrometers, whereas the dimension of the entire workpiece is about 8 mm. It thus spans spatial scales of two orders of magnitude. The sufficient discretization in a direct simulation is too costly in terms of allocated memory for a customary personal computer.

The strategy breaks the overall problem into three spatial scales, and involves accordingly three separate modeling steps. The macroscopic step uses the active area density approach to compute the current density distribution over the entire workpiece. From this distribution, the mean current densities of chosen mesoscopic regions are determined.

The latter are used as input for the total current in the simulations of the mesoscopic step. The mesoscopic reactor covers not only the mesoscopic region of interest, but also a specific surrounding region, which prevents a false behavior of the current density distribution at the border region and thus improves the accuracy of the simulations. The choice of an appropriate frame size is sophisticated. It has been shown by comparison with direct simulations that the frame size should be 1.5 times the width of the mesoscopic region of interest for satisfying accuracy, and 3 times for good accuracy.

The microscopic modeling step involves moving-boundary simulations. It was chosen to be two-dimensional and is thus restricted to the

investigation of trenches. The mean current density of the microscopic simulations is determined from the mesoscopic current density distribution. The microscopic reactor covers the trench in question and half of the photolithographic mask by which it is enclosed. This step yields the time-dependent etch profile of any chosen trench on the complex workpiece.

The potential of an auxiliary electrode in securing a uniform shape evolution of a PCB has been investigated. The shape evolution without auxiliary means was significantly non-uniform, reflected in a macroscopic Wagner's number of  $3.5 \cdot 10^{-3}$ . At a trench close to the corner the metal was completely etched off before the insulating support was exposed to the electrolyte at a trench located in the central region. According to these results, the process would surely suffer from loss of electrical contact. Applying an auxiliary electrode which was optimized in terms of its geometry and potential yielded an almost uniform shape evolution. Loss of electrical contact due to a non-uniform machining rate may thus be prevented by using a properly designed auxiliary electrode.

The optimization of the auxiliary electrode with respect to the uniformity of the workpiece's current density distribution is a sophisticated problem because of the complex patterning of the PCB. Besides the current density extrema caused by geometric factors, there are extrema caused by the pattern density. A complex interplay of different extrema was found to govern the criterion for uniformity. This interplay and the shapes and trends of the dependencies was cleared up by plotting the current density of the governing extrema against the parameters in question. Regimes where the criterion does not depend on the mean current density of the auxiliary electrode were found if the global extrema were too far away to be significantly influenced by the auxiliary electrode.

The accuracy of the first two steps of the modeling strategy has been evaluated by taking direct simulations as a benchmark. The agreement of the macroscopic modeling with the direct simulations was from 3.3% to 0.1% for 5  $\mu\text{m}$  photoresist thickness and from 4.3% to zero for 40  $\mu\text{m}$  photoresist thickness. The accuracy of the mesoscopic step has been evaluated with direct simulations having a finer discretization on the mesoscopic regions in question. It varied from 21.77% to 1.77% with the frame size suggested for satisfying accuracy, and from 9.51% to 1.51% with the frame size suggested for good accuracy. The agreement is in

general worse at the border regions of the workpiece.

The accuracy of the mesoscopic step is influenced by macroscopic and mesoscopic non-uniformity. Mesoscopic non-uniformity depends on the design of the surrounding features and equally concerns all raster elements. It affects the border region of raster elements but not the central region. It is accounted for with good accuracy by an appropriate frame. Macroscopic non-uniformity is only partly taken into account for raster elements at the border of the workpiece. It is thus an inherent error in the modeling strategy which remains as smallest possible error if the frame size is appropriate. Macroscopic non-uniformity affects the entire raster element and may cause much larger error than mesoscopic non-uniformity. It is the stronger the closer a raster element is located to the corners and edges, respectively.

The direct simulation of PCBs with moving boundaries is infeasible with the given software and hardware configuration. The direct simulation of the initial current density distribution may be feasible with constraints, as the ones performed in this thesis for the evaluation of the accuracy. Their computation was only feasible because the PCB is relatively small with a width of about 8 mm. However, the discretization was in principle insufficient and the results could only be considered reliable in the special purpose. PCBs in industrial applications may have a width of centimeters or even larger, which renders any direct simulation infeasible. Tab. 9.1 lists the nodes and elements of the meshes in some chosen simulations of this thesis. The direct simulations with meshes of about 12 million elements are replaced by two separate simulations with 3.8 and 1 million elements, respectively. Both of the latter have a sufficient discretization and are easily feasible on a 2.67 GHz dual-core, 2 GB RAM personal computer. It is emphasized that the comparison in Tab. 9.1 is in principle not justified. A direct simulation with sufficient discretization on the entire workpiece would need much more nodes and elements. The meshes of the direct simulations in Tab. 9.1 are only sufficient on the respective raster element although they are the finest possible with the given memory.

The simulations presented in this thesis are believed to be a valuable tool in the optimization of through-mask EMM processes. The modeling on the microscopic scale reported in literature has lead to a fundamental understanding of the process and given insight in proper ways of opti-

	Nodes	Elements
Modeling strategy		
Macroscopic step	706,032	3,834,734
Mesoscopic step D9	209,876	1,089,412
Mesoscopic step F8	219,449	1,151,324
Mesoscopic step A2	227,180	1,184,775
Direct Simulation D9	2,255,198	11,952,862
Direct Simulation F8	2,181,337	11,922,106
Direct Simulation A2	2,082,064	11,365,365

Table 9.1: Nodes and elements of the meshes in the modeling strategy and the direct simulations. The modeling strategy simulations with frame 5 are given here.

mization. However, the real complexity of a photolithographically patterned substrate could not be accounted for in these studies. The results presented here consider influences from three different spatial scales and thus reflect the complexity of such workpieces. The modeling strategy is a powerful tool for predicting and governing relevant process characteristics over complex structured electrodes. This study is believed to be of particular importance in research on highly complex workpieces which could be encountered in industrial applications.

# Appendix A

## Photoresist Thickness

This appendix deals with the influence of the photoresist thickness on current density distributions on different spatial scales. This subject is discussed for migrational transport, that is, for primary or secondary distributions. Convection and diffusion are not considered here.

On the microscopic scale, the effect of photoresist thickness has been discussed in literature in detail (e.g. [38, 52]). It is understood, that a large photoresist thickness makes the current density distribution uniform. If the mask would be as thick as to touch the counter electrode, the reactor would correspond to a cell with plain parallel electrodes filling completely the cross-section. Due to its geometry, such a cell always shows a uniform current density distribution (see [1, 2]). A thick photolithographic mask may be interpreted as an intermediate step towards such a reactor.

It has been reported that the microscopic current density distribution is uniform if the aspect ratio is 1 or larger. This subject is demonstrated by computing the current density distribution on a single trench with a width of 50  $\mu\text{m}$  and different aspect ratios. Fig. A.1 shows the reactor of the simulations. The electrochemical parameters are the same as in Chap. 6. The current density distributions are depicted in Fig. A.3. The distribution is already almost uniform for aspect ratio 0.5, and there is no significant non-uniformity for aspect ratio 1. The difference between the aspect ratios occurring in the two direct simulations, 0.12 and 1.01 (see Chap. 7), is surely of significance.

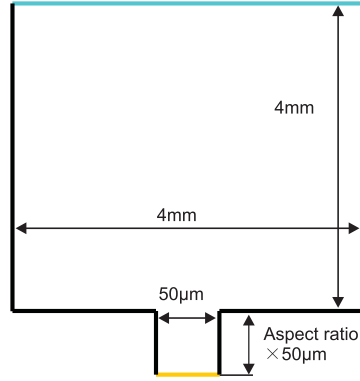


Figure A.1: Reactor containing a single trench with 50  $\mu\text{m}$  width. Not true to scale.

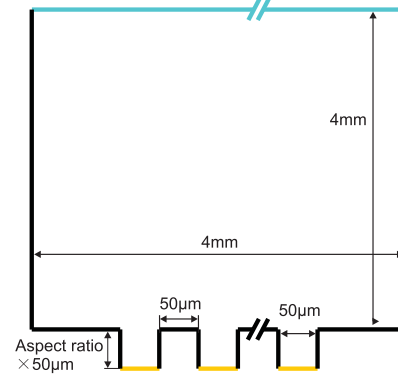


Figure A.2: Reactor containing 11 equidistant trenches with 50  $\mu\text{m}$  width; the trenches not shown in this figure have the same dimensions. Not true to scale.

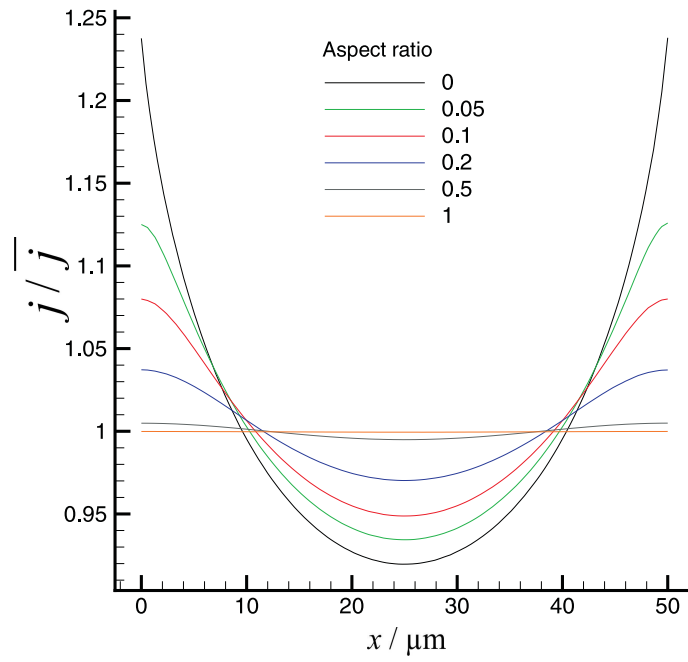


Figure A.3: Normalized current density distributions on a single trench with aspect ratios 0, 0.05, 0.1, 0.2, 0.5 and 1.



Aspect ratio	Trench No.					
	1	2	3	4	5	6
0	1.55	1.08	0.90	0.81	0.77	0.76
0.05	1.54	1.08	0.90	0.82	0.78	0.76
0.1	1.52	1.08	0.91	0.82	0.78	0.77
0.2	1.50	1.08	0.91	0.83	0.79	0.77
0.5	1.44	1.08	0.93	0.85	0.81	0.79
1	1.36	1.08	0.95	0.87	0.83	0.82

Table A.1: Normalized mean current densities of the trenches from Fig. A.4 for aspect ratios 0, 0.05, 0.1, 0.2, 0.5 and 1. Trench 1 is at the brink and trench 6 in the middle of the reactor.

In the following, the effect of photoresist thickness is discussed on the macroscopic scale. This subject has to our knowledge not been explicitly treated in literature. A demonstrative reactor containing 11 equidistant trenches (Fig. A.2) was chosen for this investigation. Evidently, the electrochemical parameters are equal to those used in Chap. 6.

Fig. A.4 shows the current density distribution on the trenches for different aspect ratios. Changing the aspect ratio significantly influences the distributions on the microscopic scale, whereas the mean current density of the trenches is barely influenced. This finding is quantified in Tab. A.1, which lists the normalized mean current densities of the trenches for the different aspect ratios. Because of the reactor's symmetry, only half of the trenches are listed. The changes in the mean current densities are minor compared to the changes in the microscopic current density distributions. The effect of photoresist thickness also makes macroscopic current density distributions more uniform, but this is much less pronounced than on the microscopic scale.

This finding is the reason for the good accuracy of the macroscopic step of the modeling strategy presented in Chap. 7.1. Such as the mean current densities of the trenches in Tab. A.1 do not change significantly with the photoresist thickness, the mean current densities of raster elements are barely influenced by this factor. The current density distributions on the raster elements are strongly influenced by the photoresist thickness.

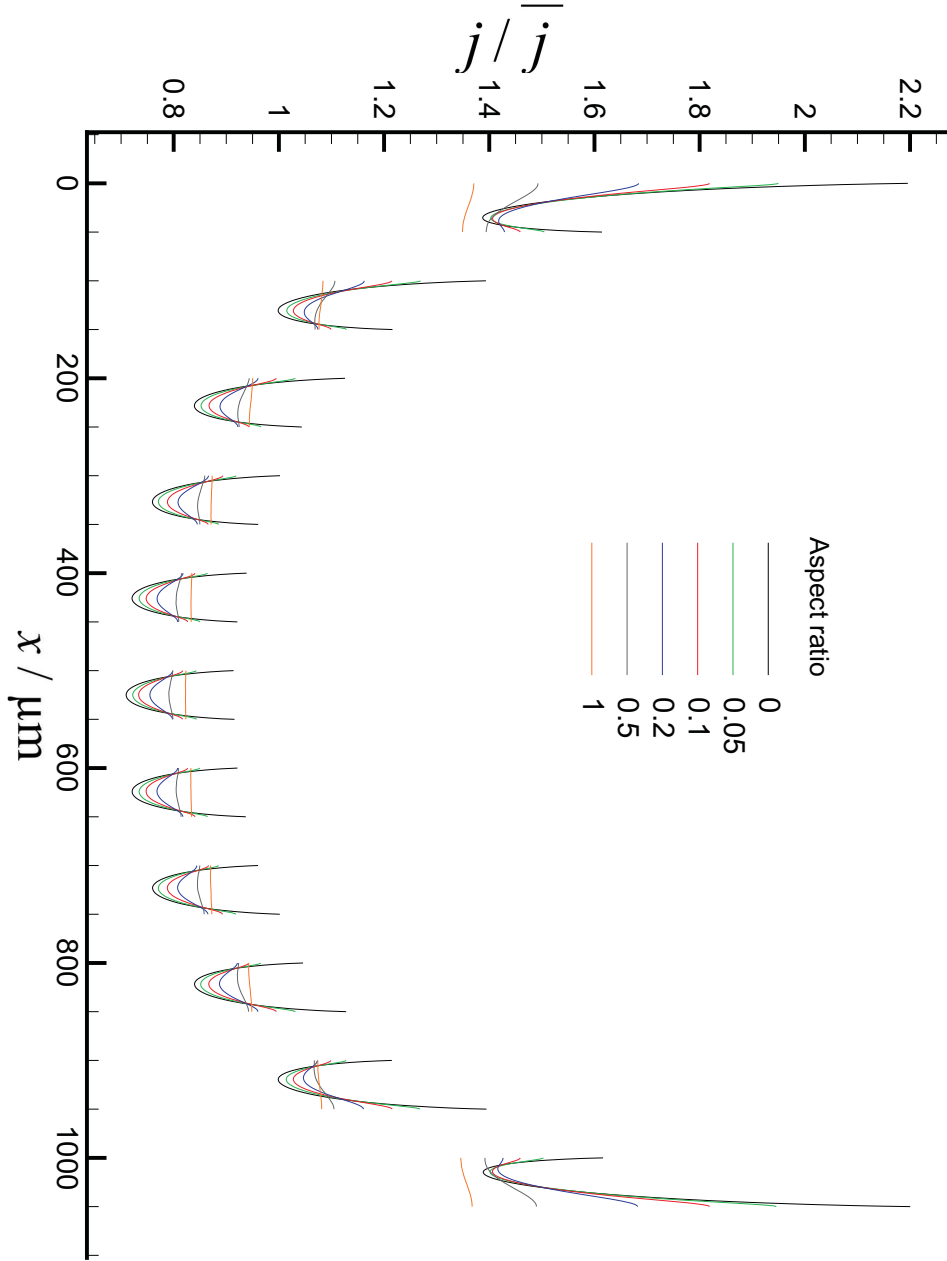


Figure A.4: Normalized current density distributions on 11 equidistant trenches with aspect ratios 0, 0.05, 0.1, 0.2, 0.5 and 1.

# Appendix B

## Numerical Issues

**Computation of  $j_r$**  The computation of the residual current density  $j_r$ , defined in Eq. 7.2, involves the subtraction of  $j_{\text{direct}}$  from  $j_{\text{strategy}}^{\text{meso}}$ . The values of these two quantities are supposed to be comparably large, because this means a good accuracy. It is shown in Chap. 7.2, that this difference may be in the range of a few percent. In the subtraction of two comparably large numbers, one always has to keep in mind that the error of the minuend and/or subtrahend may be dramatically amplified in the difference.

There is an error in  $j_{\text{strategy}}^{\text{meso}}$ , which has to be considered to avoid its amplification in  $r$ : The mean current density of the discussed mesoscopic current density distributions (e.g., Figs. 6.10 and 6.16), which is named the real mean current density, differs from the intended one, which was evaluated from the macroscopic current density distribution. This is because it is highly unpractical in the simulations using a frame to adjust the mean current density of the raster element very precisely. The difference may be around 1–2 ‰, which is well below the expected accuracy of the simulation and thus normally not of interest. If the difference between  $j_{\text{direct}}$  and  $j_{\text{strategy}}^{\text{meso}}$  is 1 ‰, this error may amplify to a relative error of  $j_r$  of 10–20 ‰, which is surely not satisfying.

To avoid this error, the mesoscopic current density distribution from the modeling strategy,  $j_{\text{strategy}}^{\text{meso}}$ , is multiplied by the fraction of the intended total current  $i_{\text{strategy}}^{\text{intended}}$  through the respective raster element and

the real total current  $i_{\text{strategy}}^{\text{real}}$  through the respective raster element:

$$j_r = \frac{j_{\text{strategy}}^{\text{meso}} \frac{i_{\text{strategy}}^{\text{intended}}}{i_{\text{strategy}}^{\text{real}}} - j_{\text{direct}}}{j_{\text{direct}}}. \quad (\text{B.1})$$

Eq. B.1 was used for the computation of  $j_r$  instead of Eq. 7.2.

The distributions of  $j_{\text{strategy}}^{\text{meso}}$  and  $j_{\text{direct}}$  are discretized with different meshes. The subtraction in Eq. B.1 evidently involves current densities at the same point, i.e., both distributions must be discretized with the same mesh to compute  $j_r$ . The finer discretized distribution, which is the one from the modeling strategy simulation, is interpolated at the coarser mesh, which is the one from the direct simulation. The interpolation was performed with the Kriging technique contained in Tecplot [53].

**Computation of  $r$**  Because the computation of  $r$  involves the same subtraction as the computation of  $j_r$ , the same problems concerning mean current densities and non-identical discretizations occur here. Eq. 7.3 is accordingly extended to

$$r = \frac{j_{\text{strategy}}^{\text{meso}} \frac{i_{\text{strategy}}^{\text{intended}}}{i_{\text{strategy}}^{\text{real}}} - j_{\text{direct}}}{j_{\text{direct}}}, \quad (\text{B.2})$$

and the latter is used in all computations of  $r$ . Interpolation of the distributions is performed as in the computation of  $j_r$ .

**Computation of  $\Sigma$**  The calculation of  $\Sigma$  involves a two-dimensional integral over the respective raster element, which has to be solved numerically. The integral is substituted for a sum over equidistant points. Evidently, the discretizations in all simulations do not consist of equidistant points; the meshes are always finer at corners and edges (where maxima of current density are expected). A mesh consisting of (approximately) equidistant nodes was created for every raster element, and both  $j_{\text{strategy}}^{\text{meso}}$  and  $j_{\text{direct}}$  were interpolated at this mesh. Fig. B.1 shows the mesh used for raster element D9; it consists of 7,904 nodes and 15,028 elements.

Replacing the integral in the computation of  $\Sigma$  by a sum transforms

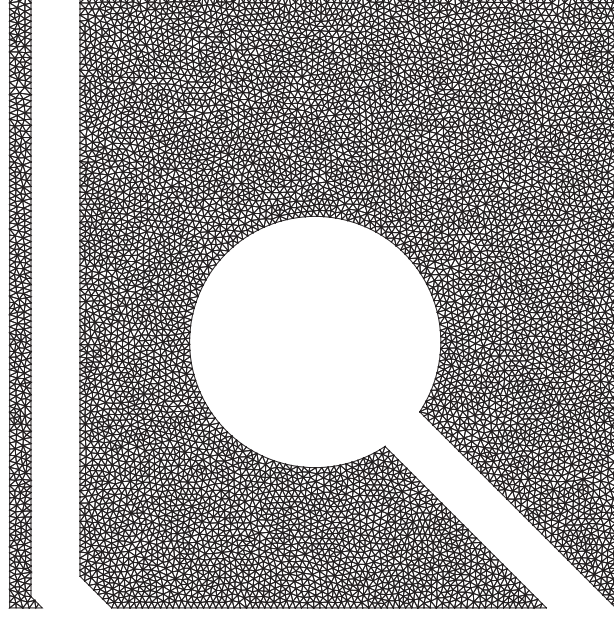


Figure B.1: Discretization for raster element D9 consisting of equidistant nodes.

Eq. 7.4 into

$$\Sigma = \sqrt{\frac{\sum_{i=1}^N r_i^2}{N}}, \quad (\text{B.3})$$

where  $r_i$  is  $r$  at a given point and  $N$  is the number of the nodes of the respective mesh.



# Bibliography

- [1] N. Ibl, in: *Comprehensive Treatise of Electrochemistry*, Vol. 6, E. Yeager, J. O. Bockris, B. E. Conway and S. Sarangapani, Editors, p. 239 (Plenum Press, New York, 1983).
- [2] J. Newman, *Electrochemical Systems* (Prentice-Hall, New York, 1991).
- [3] G. A. Prentice and C. W. Tobias, J. Electrochem. Soc. **129**, 72 (1982).
- [4] M. Datta, R. V. Shenoy, and L. T. Romankiw, J. Eng. Ind. **118**, 29 (1996).
- [5] M. Datta, IBM J. Res. Dev. **42**, 655 (1998).
- [6] M. Datta and D. Landolt, Electrochim. Acta **45**, 2535 (2000).
- [7] S. Krongelb, L. T. Romankiw, and J. A. Tornello, IBM J. Res. Dev. **42**, 575 (1998).
- [8] K. K. H. Wong, S. Kaja, and P. W. DeHaven, IBM J. Res. Dev. **42**, 587 (1998).
- [9] C. F. Coombs, *Printed Circuits Handbook* (McGraw-Hill, New York, 2001).
- [10] B. Bhattacharyya, J. Munda, and M. Malapati, Int. J. Mach. Tools Manufact. **44**, 1577 (2004).
- [11] J. L. Vossen and W. Kern, *Thin Film Processes* (Academic Press, New York, 1991).
- [12] M. Datta and L. T. Romankiw, J. Electrochem. Soc. **136**, 285C (1989).

- [13] M. Georgiadou and R. Alkire, *J. Electrochem. Soc.* **140**, 1340 (1993).
- [14] M. Georgiadou and R. Alkire, *J. Electrochem. Soc.* **140**, 1348 (1993).
- [15] M. Georgiadou and R. Alkire, *J. Electrochem. Soc.* **141**, 679 (1994).
- [16] C. Madore and D. Landolt, *J. Micromech. Microeng.* **7**, 270 (1997).
- [17] C. Madore, O. Piotrowski, and D. Landolt, *J. Electrochem. Soc.* **146**, 2526 (1999).
- [18] P. Kern, J. Veh, and J. Michler, *J. Micromech. Microeng.* **17**, 1168 (2007).
- [19] P.-F. Chauvy, P. Hoffmann, and D. Landolt, *Appl. Surf. Sci.* **208-209**, 165 (2003).
- [20] M. Datta, *J. Electrochem. Soc.* **142**, 3801 (1995).
- [21] M. Datta and L. T. Romankiw, U.S. Patent 5,284,554 (1994).
- [22] H. McCrabb, A. Lozano-Morales, S. Snyder, L. Gebhart, and E. J. Taylor, Meet. Abstr. – *Electrochem. Soc.* **901**, 1019 (2009).
- [23] G.-J. Kwon, H.-Y. Sun, and H.-J. Sohn, *J. Electrochem. Soc.* **142**, 3016 (1995).
- [24] M. Datta, *Interface (The Electrochemical Society)* **4**, 32 (1995).
- [25] M. Datta and D. L. King and A. D. Knight and C. J. Sambrucetti, U.S. Patent 5,105,537 (1992).
- [26] M. Datta and D. Harris, *Electrochim. Acta* **42**, 3007 (1997).
- [27] R. P. Frankenthal and H. D. Eaton, *J. Electrochem. Soc.* **123**, 703 (1976).
- [28] N. Ibl, IUPAC Information Bulletin, No. 59 (1977).
- [29] C. Wagner, *J. Electrochem. Soc.* **98**, 116 (1951).
- [30] S. Mehdizadeh, J. O. Dukovic, P. C. Andricacos, and L. T. Romankiw, *J. Electrochem. Soc.* **139**, 78 (1992).
- [31] T. Kessler and R. Alkire, *Plat. Surf. Finish.* **63**, 22 (1976).



- [32] J. O. Dukovic, IBM J. Res. Dev. **34**, 693 (1990).
- [33] J. O. Dukovic, in: *Advances in Electrochemical Science and Engineering*, Vol. 3, H. Gerischer and C. W. Tobias, Editors, p. 117 (VCH, Weinheim, 1994).
- [34] S. Mehdizadeh, J. Dukovic, P. C. Andricacos, and L. T. Romankiw, J. Electrochem. Soc. **140**, 3497 (1993).
- [35] K. Pantleon, B. Van den Bossche, M. Purcar, P. Bariani, and G. Floridor, J. Appl. Electrochem. **35**, 589 (2005).
- [36] A. C. West, M. Matlosz, and D. Landolt, J. Electrochem. Soc. **138**, 728 (1991).
- [37] B. DeBecker and A. C. West, J. Electrochem. Soc. **143**, 486 (1996).
- [38] A. C. West, C. Madore, M. Matlosz, and D. Landolt, J. Electrochem. Soc. **139**, 499 (1992).
- [39] R. V. Shenoy and M. Datta, J. Electrochem. Soc. **143**, 544 (1996).
- [40] R. V. Shenoy, M. Datta, and L. T. Romankiw, J. Electrochem. Soc. **143**, 2305 (1996).
- [41] B. Mollay *et al.*, in: *Microfabricated Systems and MEMS VII*, 2004-09, J. L. Davidson, P. J. Hesketh, D. Misra, and S. Shoji, Editors, p. 87 (The Electrochemical Society Softbound Proceedings, Pennington, NJ, 2004).
- [42] S. Dalby, J. Nickelsen, and L. Alting, Electroplat. Met. Finish. **28**, 18 (1975).
- [43] M. McCormick, D. Howe, and S. Y. Parn, Trans. Ins. Met. Finish. **62**, 129 (1985).
- [44] S. Mehdizadeh, J. Dukovic, P. C. Andricacos, and L. T. Romankiw, J. Electrochem. Soc. **137**, 110 (1990).
- [45] Y. Choi and T. Kang, J. Electrochem. Soc. **143**, 480 (1996).
- [46] Y. Oh, S. Chung, and M. Lee, Mater. Trans. **45**, 3005 (2004).
- [47] T. Okubo, T. Kodera, and K. Kondo, Chem. Eng. Comm. **193**, 1503 (2006).

- [48] PlatingMaster V 3.0 User Manual, [www.elsyca.com](http://www.elsyca.com).
- [49] ElSy V 6.1 User Manual, [www.elsyca.com](http://www.elsyca.com).
- [50] M. Purcar, B. V. den Bossche, L. Bortels, J. Deconinck, and G. Nelissen, *J. Electrochem. Soc.* **151**, D78 (2004).
- [51] G. Nelissen, A. V. Theemsche, S. Lecho, and J. Deconinck, *Galvanotech.* **91**, 970 (2000).
- [52] R. C. Alkire, H. Deligianni, and J.-B. Ju, *J. Electrochem. Soc.* **137**, 818 (1990).
- [53] Tecplot Focus 2009 User Manual, [www.tecplot.com](http://www.tecplot.com).

# Publications on this Thesis

## Publications in reviewed journals

P. Raffelstetter, B. Mollay, B. Van den Bossche, and G. E. Nauer,  
“Modeling Strategy for Predicting Current Density Distributions on PCBs  
and Other Complex Patterned Substrates”,  
J. Electrochem. Soc. **156**, D51 (2009)

P. Raffelstetter and B. Mollay,  
“On the Modeling of Shape Evolution in Through-Mask Electrochemical  
Micromachining of Complex Patterned Substrates”,  
Electrochim. Acta **55**, 2149 (2010)

## Conference proceedings

P. Raffelstetter and B. Mollay,  
“Electrochemical Micromachining of Complex Photolithographically Pat-  
terned Substrates: A Modeling Study on the Influence of the Design”,  
Proceedings on the 5<sup>th</sup> International Symposium on Electrochemical Mi-  
cromachining Technology (INSECT), Dresden, Germany, 2009

## Oral presentations at conferences

P. Raffelstetter, B. Mollay, B. Van den Bossche, M. Purcar, G. Nelissen,  
G. Fafilek, H. Kronberger, J. Deconinck, and G. E. Nauer,  
“Modelling of Electrochemical Pattern Etching Processes: Influence of  
the Design”,  
58<sup>th</sup> Annual Meeting of the International Society of Electrochemistry,  
Banff, Canada, 2007

P. Raffelstetter, B. Mollay, and G. E. Nauer,

“Modelling of Through-Mask Electrochemical Micromachining on Complex PCB Designs”,

214<sup>th</sup> Fall Meeting of the Electrochemical Society, Honolulu, USA, 2008

P. Raffelstetter and B. Mollay,

“Modeling of the Effect of an Auxiliary Electrode on Shape Evolution in Through-Mask Electrochemical Micromachining of a PCB Design”,

60<sup>th</sup> Annual Meeting of the International Society of Electrochemistry, Beijing, China, 2009

P. Raffelstetter and B. Mollay,

“Modeling Strategy for Predicting Current Density Distributions on PCBs and Other Complex Patterned Substrates”,

5<sup>th</sup> International Symposium on Electrochemical Micromachining Technology (INSECT), Dresden, Germany, 2009

# List of Symbols

$A$	Area ( $\text{m}^2$ )
$A^{\text{ACT}}$	Active area ( $\text{m}^2$ )
$A^{\text{SUP}}$	Superficial area ( $\text{m}^2$ )
$a$	Active area density
$c_k$	Concentration of species k ( $\text{mol m}^{-3}$ )
$D_k$	Diffusion coefficient of species k ( $\text{m}^2 \text{s}^{-1}$ )
$d$	Distance of the auxiliary electrode from the workpiece ( $\text{m}$ )
$\Delta$	Criterion for the accuracy of the macroscopic modeling step
$\delta$	Criterion for the uniformity of current density distributions
$F$	Faraday's constant ( $\text{C mol}^{-1}$ )
$f$	Factor by which $j(x, y, z)^{\text{AE}}$ is multiplied to yield $j(x, y, z)^{\text{AE}}$
$\eta$	Overpotential (V)
$I$	Mean current density of the auxiliary electrode (normalized to the mean current density of the workpiece)
$i$	Current of respective raster element (A)
$\mathbf{j}$	Current density ( $\text{A m}^{-2}$ )
$j$	Component of $\mathbf{j}$ at electrode surfaces perpendicular to the latter ( $\text{A m}^{-2}$ )
$j(x, y, z)$	Current density distribution ( $\text{A m}^{-2}$ )
$j(x, y, z)^{\text{AE}}$	Current density distribution considering an auxiliary electrode ( $\text{A m}^{-2}$ )
$j(x, y, z)^{\text{AE}}$	Current density distribution not considering an auxiliary electrode ( $\text{A m}^{-2}$ )

$j_r$	Residual current density
$\overline{j^{\text{ACT}}}$	Active current density ( $\text{A m}^{-2}$ )
$\overline{j^{\text{ACT}}}$	Mean active current density ( $\text{A m}^{-2}$ )
$j_{\max}^{\text{ACT}}$	Maximum active current density ( $\text{A m}^{-2}$ )
$j_{\min}^{\text{ACT}}$	Minimum active current density ( $\text{A m}^{-2}$ )
$\overline{j^{\text{SUP}}}$	Superficial current density ( $\text{A m}^{-2}$ )
$\overline{j^{\text{AE}}}$	Mean current density of $j(x, y, z)^{\text{AE}}$ ( $\text{A m}^{-2}$ )
$\overline{j^{\text{AE}}}$	Mean current density of $j(x, y, z)^{\text{AE}}$ ( $\text{A m}^{-2}$ )
$\kappa$	Conductivity of the electrolyte ( $\text{S m}^{-1}$ )
$l$	Characteristic length (m)
$\mathbf{N}_k$	Flux density of species k ( $\text{mol m}^{-2} \text{ s}^{-1}$ )
$n$	Spatial coordinate perpendicular to boundaries (m)
$R$	Gas constant ( $\text{J mol}^{-1} \text{ K}^{-1}$ )
$r$	Relative error of current density distributions
$\rho$	Resistivity of the electrolyte ( $\Omega \text{ m}$ )
$\Sigma$	Criterion for the accuracy of the mesoscopic modeling step
$\sigma^2$	Mean-root-square deviation of the current density from its average
$T$	Temperature (K)
$t$	Time (s)
$U$	Potential of the electrolyte (V)
$V$	Potential of an electrode (V)
$V_0$	Equilibrium potential of an electrode (V)
$\mathbf{v}$	Flow field; velocity of the electrolyte ( $\text{m s}^{-1}$ )
$W_a$	Wagner's number
$w$	Width of the auxiliary electrode (m)
$x, y, z$	Cartesian coordinates (m)
$v_k$	Rate of production of species k by chemical reactions ( $\text{mol m}^{-3} \text{ s}^{-1}$ )
$z_k$	Charge of species k

# List of Figures

1.1	Typical photolithographically structured substrate. . . .	2
3.1	Schematic illustration of the current lines in a parallel plate reactor. . . . .	16
5.1	Flowchart of the proposed modeling strategy. . . . .	32
6.1	PCB design. . . . .	34
6.2	PCB design and raster. . . . .	35
6.3	Active area density distribution of the PCB according to Fig. 6.2. . . . .	35
6.4	Macroscopic reactor. . . . .	35
6.5	A part of the surface mesh of the macroscopic reactor in Fig. 6.4. . . . .	35
6.6	Macroscopic current density distribution of $j^{\text{ACT}}$ . . . . .	36
6.7	Names of the raster elements on the PCB, according to the orientation of the workpiece in Figs. 6.2 and 6.3. . . .	37
6.8	Mesoscopic reactor for raster element D9. . . . .	38
6.9	A part of the surface mesh of the mesoscopic reactor in Fig. 6.8. . . . .	38
6.10	Mesoscopic current density distribution on raster element D9 obtained without a frame. . . . .	39
6.11	Mesoscopic regions considered in the simulation of raster element D9. . . . .	40
6.12	Cross-section of the current density distributions along the solid black line in Fig. 6.11. . . . .	41
6.13	Mesoscopic current density distribution on raster element D9 obtained with frame 5. . . . .	43

6.14	Mesososcopic regions considered in the simulation of raster element F10. . . . .	44
6.15	Cross-section of the current density distributions along the solid black line in Fig. 6.14. . . . .	45
6.16	Mesososcopic current density distribution on raster element F10 obtained without a frame. . . . .	46
6.17	Mesososcopic current density distribution on raster element F10 obtained with frame 5. . . . .	46
6.18	Mesososcopic regions considered in the simulation of raster element A2. . . . .	47
6.19	Cross-section of the current density distributions along the solid black line in Fig. 6.18. . . . .	48
6.20	Mesososcopic current density distribution on raster element A2 obtained without a frame. . . . .	50
6.21	Mesososcopic current density distribution on raster element A2 obtained with frame 5. . . . .	50
6.22	Mesososcopic current density distribution on raster element B2 obtained with frame 5. . . . .	51
6.23	Mesososcopic current density distribution on raster element B6 obtained with frame 5. . . . .	51
6.24	Trenches chosen for the microscopic simulations, named trench 1–3. . . . .	52
6.25	Microscopic reactor. . . . .	53
6.26	A part of the surface mesh of the microscopic reactor. . .	53
6.27	Initial current density distribution on trench 1. . . . .	54
6.28	Microscopic shape evolution of trenches 1–3 for different points in time. . . . .	55
6.29	Macroscopic reactor with base case auxiliary electrode. .	57
6.30	A part of the surface mesh of the reactor in Fig. 6.29. . .	57
6.31	Normalized macroscopic current density distribution of $j^{\text{ACT}}$ with the base case auxiliary electrode. . . . .	58
6.32	$\delta$ versus $I$ for $w = 1$ mm and different $d$ . . . . .	59
6.33	$\delta$ versus $I$ for $d = 0.15$ mm and different $w$ . . . . .	60
6.34	Normalized current density of the governing extrema versus $I$ for $w = 1$ mm and $d = 0.2$ mm. . . . .	61



6.35	Normalized current density of the governing extrema versus $I$ for $w = 1$ mm and $d = 0.15$ mm. . . . .	62
6.36	Normalized current density of the governing extrema versus $I$ for $w = 1$ mm and $d = 0.05$ mm. . . . .	63
6.37	$\delta$ versus $d$ for different $w$ and optimum $I$ . . . . .	64
6.38	Microscopic shape evolution of trenches 1–3 for different points in time with the base case auxiliary electrode. . .	66
7.1	Reactor of the direct simulation. . . . .	68
7.2	A part of the surface mesh of the reactor in Fig. 7.1. . .	68
7.3	The surface mesh of the reactor in Fig. 7.1 at the lower left corner of raster element D9. . . . .	69
7.4	Normalized current density distribution of the direct simulation. . . . .	70
7.5	Normalized current density distribution of the direct simulation with 40 $\mu\text{m}$ photoresist thickness. . . . .	70
7.6	The surface mesh at the lower left corner of raster element D9 for the direct simulation with a finer discretization on this element. . . . .	76
7.7	Mesosopic current density distribution on raster element D9 from the direct simulation. . . . .	77
7.8	$j_r$ distribution on raster element D9 without frame. . . .	78
7.9	$j_r$ distribution on raster element D9 with frame 1. . . . .	79
7.10	$j_r$ distribution on raster element D9 with frame 2. . . . .	79
7.11	$j_r$ distribution on raster element D9 with frame 3. . . . .	80
7.12	$j_r$ distribution on raster element D9 with frame 4. . . . .	81
7.13	$j_r$ distribution on raster element D9 with frame 5. . . . .	81
7.14	$r$ distribution on raster element D9 without frame. . . .	83
7.15	$r$ distribution on raster element D9 with frame 5. . . . .	83
7.16	$\Sigma$ versus width of the frame normalized to the width of the raster element for element D9. . . . .	84
7.17	Mesosopic current density distribution on raster element F10 from the direct simulation having a finer discretization there. . . . .	85
7.18	$j_r$ distribution on raster element F10 without frame. . . .	86
7.19	$j_r$ distribution on raster element F10 with frame 3. . . .	87

7.20	$j_r$ distribution on raster element F10 with frame 5. . . .	88
7.21	$\Sigma$ versus width of the frame normalized to the width of the raster element for element F10. . . . .	88
7.22	Mesosopic current density distribution on raster element A2 from the direct simulation having a finer discretization there. . . . .	89
7.23	$j_r$ distribution on raster element A2 without frame. . . .	90
7.24	$j_r$ distribution on raster element A2 with frame 2. . . . .	91
7.25	$j_r$ distribution on raster element A2 with frame 5. . . . .	91
7.26	$\Sigma$ versus width of the frame normalized to the width of the raster element for element A2. . . . .	92
A.1	Reactor containing a single trench with 50 $\mu\text{m}$ width. . .	102
A.2	Reactor containing 11 equidistant trenches with 50 $\mu\text{m}$ width. . . . .	102
A.3	Normalized current density distributions on a single trench.	102
A.4	Normalized current density distributions on 11 equidistant trenches. . . . .	104
B.1	Discretization for raster element D9 consisting of equidistant nodes. . . . .	107

# List of Tables

7.1	Currents through raster elements $i$ for the macroscopic modeling step and the direct simulations with 5 $\mu\text{m}$ and 40 $\mu\text{m}$ photoresist thickness. . . . .	74
9.1	Nodes and elements of the meshes in the modeling strategy and the direct simulations. . . . .	100
A.1	Normalized mean current densities of the trenches from Fig. A.4. . . . .	103



# Curriculum Vitae

## Personal Details

Name	Peter Raffelstetter
Address	Amalie-Seidel-Weg 3/3/2.05, 1120 Vienna, Austria
Citizenship	Austria
Place and date of birth	Vienna, 7.10.1982

## Education

1993-2001	Laaer Berg grammar school, 1100 Vienna
2001	A-levels
2001-2007	Diploma studies in chemistry at the University of Vienna
2005	Chinese language course 1A (phase 1 and 2) at the language center at the University of Vienna
2007	Diploma thesis "Phase diagram investigations and chemical vapor transport in the system Mo-Ta-As"
2007-2010	Doctoral studies in chemistry at the University of Vienna
2007-2008	Part-time bachelor studies in Chinese at the University of Vienna

## Internships

July-August 2003	Research internship at the mass spectrometry group of the Department of Analytical Chemistry, University of Vienna
June-July 2005	Research internship at the Institute of Traditional Chinese Medicine of the East China University of Science and Technology (Shanghai)

